PHASE CHANGE PHENOMENA ON WATER REPELLING AND BIPHILIC SURFACES

BY

SHREYAS ATMARAM CHAVAN

DISSERTATION

Submitted in partial fulfillment of the requirements
for the degree of Doctor of Philosophy in Mechanical Engineering
in the Graduate College of the
University of Illinois at Urbana-Champaign, 2019

Urbana, Illinois

Doctoral Committee:

      Assistant Professor Nenad Miljkovic, Chair and Director of Research
      Professor Anthony M. Jacobi
      Professor Predrag S. Hrnjak
      Associate Professor Randy H. Ewoldt
      Dr. Ryan Enright, Nokia Bell Labs Ireland

ABSTRACT

Water-repelling surfaces have been studied for many decades. Hydrophobic and superhydrophobic surfaces are beneficial in phase change heat transfer applications, specifically during condensation because of the enhanced heat transfer and during freezing because of the anti-freezing properties. The current study is focused on enhanced phase change phenomena on superhydrophobic and biphilic surfaces. Hydrophobic surfaces that enable dropwise condensation exhibit 5-10X higher heat transfer. Coalescence induced droplet jumping on superhydrophobic surfaces further increases the heat transfer by 30%. Here, biphilic surfaces consisting of hydrophilic spots on a superhydrophobic background are studied for enhanced condensation. Water droplets nucleating at the hydrophilic spots grow to sizes defined by the biphilic geometry, followed by coalescence and departure. A high fidelity model that captures departure dynamics during droplet jumping on biphilic surfaces and predict the overall condensation heat transfer has been developed. By controlling the spatial geometry and length scale of the hydrophilic spots, enhanced (10X) jumping-droplet condensation heat transfer is obtained.

In terms of freezing and frost formation, understanding the mechanisms of frost formation is essential to a variety of Heating, Ventilating, Air Conditioning and Refrigeration (HVAC&R) applications. When water vapor in the ambient condenses on a chilled substrate in the form of liquid water and then freezes, it is known as condensation frosting. The dominant mechanism governing the spread of condensation frosting is inter-droplet ice bridge frost wave propagation. When a subcooled condensate water droplet freezes on a hydrophobic or superhydrophobic surface, neighboring droplets still in the liquid phase begin to evaporate. The evaporated water molecules deposit on the frozen droplet and initiate the growth of ice bridges directed toward the

water droplets being depleted. Neighboring liquid droplets freeze as soon as the ice bridge connects. In this study, the significance of individual droplet freezing on frost wave propagation is studied. 10X slower frost wave propagation speeds on superhydrophobic surfaces are observed. Furthermore, at larger length scales, during bulk freezing of water, it has been shown that superhydrophobic surfaces offer no delay in freezing.

Although frosting delay has been shown with superhydrophobic surfaces, complete elimination of frosting has not been achieved. Given enough time, frosting will initiate and spread to cover the entire surface. In the HVAC&R sectors, the most common approach to remove frost from a surface (defrost) is to reverse the system cycle direction and heat the working fluid. However, water retention on the heat exchanger surface during defrosting decreases the long term heat transfer performance. In this study, the defrosting behavior of superhydrophobic and biphilic surfaces comprising of spatially distinct superhydrophobic and hydrophilic domains is used to accelerate defrosting. During defrosting, biphilic surfaces are shown to exhibit enhanced surface cleaning with no water retention. Furthermore, an ultra-efficient method to defrost a surface covered with ice/frost by focusing energy at the substrate-ice interface is studied. To remove ice/frost efficiently, only the interfacial layer adhering the ice/frost to the solid surface is melted by using a localized 'pulse' of heat, allowing gravity or gas shear in conjunction with the ultra-thin lubricating melt water layer to remove the ice/frost. A high fidelity numerical model is developed to simulate pulse defrosting. This work not only provides a fundamental understanding of phase change processes on superhydrophobic and biphilic surfaces, but also elucidates its applications for a plethora of energy industries.

To my parents,

Rasika and Atmaram Chavan

ACKNOWLEDGMENTS

I want to start with thanking my advisor, Prof. Nenad Miljkovic. Nenad, thank you so much for everything! I have learned so many valuable things from you, be it in research or life in general. You have taught me how to present my work in front of an audience, be it a presentation, an impromptu talk or a paper, and nail it like a boss. You inspired me by being a great example of someone with an innate passion for his work, which I have strived to emulate and will continue to do so in my life. You have always supported me whatever I did, and have guided me well throughout my Ph.D. You being an adviser, Ph.D. never seemed like an insane decision (given the prevalence of this idea in every grad student's life). I could not have asked for a better adviser!

Next, thank you to all my committee members. The summer spent with Dr. Ryan Enright at Nokia Bell Labs Ireland was one of the best summers of my life (although, apart from research, Irish countryside and lamb might have played a significant role!). Ryan is one of the most knowledgeable and smartest people I know, and working with him was a very humbling experience. Prof. Anthony Jacobi is one of the best teachers I have seen, and his course Multiphase Systems and Processes is one of my favorite courses at UIUC. Prof. Predrag Hrnjak helped me realize the nuances that may arise while scaling my research to industrial applications, and suggested ways to tackle them. Prof. Randy Ewoldt encouraged me approach certain aspects of my research from a new direction, which has helped me to dig deeper and explain my work in a better way. Apart from my committee, I would like to thank Kathryn Smith from MechSE department. I frankly don't know how the department or grad students will function without Kathy.

Now is the time to thank my family away from home. Let me start with my first roommates, Dhawal Desai, and Palash Badjatya. Dhawal, I have never come across anyone who has principles as ideal as you. Then I met Tooba Shoaib *aka* Batu, who fortunately (for her) went on to become my elder sister at Chambana. Batu, I will always be grateful to all the food you have fed to this beast, and all the relentless (and pointless) advice you have given me when I needed them the most. Then my other roommates, Vegnesh Jayaraman, and Anurag Bhattacharyya were people whose life fundaes were sorted. Vegnesh, you are the nicest person I know in my life. Manjunath CR and the adventurous (more than needed) trips with him shall always be cherished.

Even though I was thousands of miles away from home, I always felt at home because of Paul Stansberry and Becky Stansberry. You made me grow as a person, and I will never forget the Thanksgiving, Christmas, Dandiya, Diwali, and so many other things that we have done together. Those were the good times!

Finally, the most important people in my life…

I am eternally grateful to my parents, for their unconditional love, unwavering confidence, and constant motivation for me. They are the reason for what I am today. To my little sister, Shruti Chavan *aka* Rambo, lots of love and admiration. Rambo, with you, I have some of my happiest memories. Last but not least, Apurva, you have brought happiness in my life that I had never imagined. With you by the side, I am eager to see what the future holds.

Shreyas Chavan

Some parts of this thesis have been published in peer-reviewed journals. Chapter 2 is published in Applied Physics Letters (Chavan, S., J. Carpenter, M. Nallapaneni, J. Y. Chen, and N. Miljkovic. "Bulk water freezing dynamics on superhydrophobic surfaces." *Applied Physics Letters* 110, no. 4 (2017): 041604.) and Chapter 3 is published in Langmuir, reprinted with permission from (Chavan, Shreyas, Deokgeun Park, Nitish Singla, Peter Sokalski, Kalyan Boyina, and Nenad Miljkovic. "Effect of Latent Heat Released by Freezing Droplets during Frost Wave Propagation." *Langmuir* 34, no. 22 (2018): 6636-6644.). Copyright (2018) American Chemical Society.

कर्मण्येवाधिकारस्ते मा फलेषु कदाचन।

मा कर्मफलहेतुर्भूर्मा ते सङ्गोऽस्त्वकर्मणि॥

karmaṇy-evādhikāras te mā phaleṣhu kadāchana |

mā karma-phala-hetur bhūr mā te saṅgo 'stvakarmaṇi ||

"Do not let the fruit be the purpose of your actions, and therefore you won't be attached to not

doing your duty."

TABLE OF CONTENTS

LIST OF SYMBOLS

h_i	Heat transfer coefficient at liquid-vapor interface (W/m²K)
h_{fg}	latent heat of vaporization (J/kg)
$\hat{R}$	effective maximum droplet radius (m)
R_b	Droplet base radius (m)
R_e	droplet coalescence radius (m)
R_g	specific gas constant (J/mol K)
R_{min}	minimum droplet nucleation radius (m)
R_t	overall droplet thermal resistance (K/W)
T_i	Temperature at liquid-vapor interface (K)
T_s	substrate/wall temperature (K)
k_{HC}	hydrophobic promoter coating thermal conductivity (W/mK)
k_p	pillar/substrate thermal conductivity (W/m K)
k_w	water thermal conductivity (W/m K)
δ_{HC}	thickness of hydrophobic coating (m)
θ_a	advancing contact angle (deg)
v_g	water vapor specific volume (m³/kg)
ρ_w	water density (kg/m³)
$\Delta T = T_{sat} - T_s$	surface subcooling temperature (K)
h	pillar height (m)
q''	heat flux through the droplet (W/m²)
Bi	Biot Number
N	large droplet population density (m⁻³)
Nu	Nusselt number
R	Radius of the spherical droplet
n	small droplet population density (m⁻³)
α	condensation coefficient
θ	contact angle (deg)
τ	sweeping period (s)

ϕ	solid fraction
ρ	Density (kg/m^3)
T	Temperature (K)
T_s	Substrate Temperature (K)
T_{in}	Initial Temperature (K)
T_m	Melting Temperature (K)
T_{ml}	Temperature of the melt layer at $x = l_{w,c}$ (K)
T_{sol}	Solidus Temperature (K)
T_{liq}	Liquidus Temperature (K)
q''_{in}	Input heat flux by the heating element (W/m^2)
l_w	Length of the melt water layer (m)
l_i	Length of ice block attached on the substrate (m)
F_g	Gravitational force acting on the ice block (N)
F_{shear}	Shear force acting on the ice block (N)
$l_{w,c}$	Critical thickness of the melt water layer (m)
μ_w	Viscosity of water (Ns/m^2)
v	Velocity of the ice slab sliding from the substrate (m/s)
g	Gravity (m/s^2)
t_{pulse}	Duration of input heat pulse (s)
$C_{p,i}$	Specific heat of ice (J/kgK)
$C_{p,w}$	Specific heat of water (J/kgK)
L	Latent heat of fusion of water (J/kg)

CHAPTER 1: INTRODUCTION

Water-repelling surfaces have been studied for many decades [1,2]. Hydrophobic and superhydrophobic surfaces are beneficial in phase change heat transfer applications, specifically during condensation because of the enhanced heat transfer and during freezing because of the anti-freezing properties. Vapor condensation is a preferred mode of heat transfer in a wide range of applications such as thermoelectric power generation, thermal desalination, and thermal management. Water vapor condensing on high- or low-surface-energy surfaces forms a liquid film or distinct droplets, respectively. The latter, termed dropwise condensation, is desired due to its 5-10X higher heat transfer coefficient. To further enhance dropwise condensation, researchers have recently proposed the use of suitably designed superhydrophobic surfaces to enable coalescence-induced droplet jumping governed by inertial-capillary energy conversion [3,4]. By enabling droplet jumping, the average droplet size on the surface is reduced, decreasing the condensate thermal resistance and enhancing overall heat transfer by $\geq$ 30% when compared to dropwise condensation [5,6]. It has been recently shown that biphilic surfaces, consisting of hydrophilic spots on a superhydrophobic background, can significantly influence droplet size distributions and heat transfer behavior during jumping-droplet condensation [7,8]. Water droplets nucleating at the hydrophilic spots grow to sizes defined by the biphilic pattern geometry, followed by coalescence and departure. By controlling the spatial geometry and length scale of the hydrophilic spots, enhanced jumping-droplet condensation heat transfer can be obtained through the limit of droplet density. However, it remains unclear what the necessary surface energy requirements are to achieve this "patterned" mode of condensation. Moreover, accurate models that are capable of coupling both droplet-adhesion governed departure dynamics with individual transient droplet heat

1

transfer to predict the overall surface jumping-droplet condensation heat transfer on biphilic surfaces do not exist.

In terms of freezing and frost formation, understanding the mechanisms of frost formation is essential to a variety of industrial applications including refrigeration, [9,10] aviation, [11] wind energy, [12] and power transmission [13]. It has been observed that hydrophobic surfaces offer lower frost density and decreased frost growth rate as compared to hydrophilic surfaces [14]. To further delay frost formation, researchers have proposed the use of suitably designed superhydrophobic surfaces [15-17] to delay the heterogeneous nucleation of ice [18,19] as well as condensation frosting [20]. Although, at larger length scales, during bulk freezing, it has been shown that superhydrophobic surfaces offer no delay in freezing [21]. The length scales at which the droplet conduction resistance become more dominant than the interfacial air-gap resistance at solid-liquid interface is still unknown. The dominant mechanism of condensation frost formation on hydrophobic surfaces is inter-droplet frost wave propagation, [22,23] or ice bridging. When a subcooled condensate water droplet freezes on a hydrophobic or superhydrophobic surface, neighboring droplets still in the liquid phase immediately begin to evaporate [22,23]. The evaporated water molecules deposit on the frozen droplet and initiate the growth of ice bridges directed toward the water droplets that are being depleted. The significance of individual droplet freezing on frost wave propagation is still unknown.

Although frosting delay has been shown with superhydrophobic surfaces, complete elimination of frosting has not been achieved [24]. Given enough time, frosting will initiate and spread to cover the entire surface [23-25]. Due to the limitations in indefinitely preventing frost formation, industrial applications generally rely on active defrosting techniques. One active system

2

defrosting method utilizes reversal of the cycle direction to heat the working fluid and melt the frost [26,27]. However, (i) up to 27% of the total defrost heat input is used simply to heat up the evaporator [28], and (ii) up to 75% of the defrosting energy goes into heating the refrigeration system and not the ice [29]. Moreover, during frost, defrost, and refrost cycles, water retention is observed on the heat exchangers [30], which acts to decreases the overall heat transfer coefficient of a heat exchanger by 20% [10,31] and act as a seed layer for frost nucleation during the next frost cycle. Hence, there is a need of surfaces that enable no water retention upon defrosting.

In building energy applications, methods to remove frost from the surfaces of thermal components use electric heaters or hot-gas from the compressor to melt frost, which results in a further increase in energy consumption, and downtime. A need exists for defrosting approaches that are more energy efficient and quicker. Past studies have investigated electro-thermal Joule heating for de-icing applications [32-35], demonstrating a high energy requirement to achieve thermal de-icing. In order to mitigate high energy consumption, pulse electro-thermal defrosting has been proposed in the past [36,37], wherein melting of the interfacial layer adhering the ice to the solid surface allows gravity in conjunction with the ultra-thin lubricating meltwater layer to remove the ice/frost. However, accurate transient phase change heat transfer models of the pulse-defrosting process are currently not available. Furthermore, the coupling of transient lubricating film physics with the transient thermally driven phase change processes has not been explored.

1.1 Outline of the Thesis

The present research aims to understand and answer the questions outlined above. Chapter 2 presents condensation on biphilic surfaces. Enhancing the condensation heat transfer using biphilic surfaces is discussed. Chapter 3 presents bulk water freezing dynamics on

superhydrophobic surfaces and discusses avenues to delay bulk freezing. Chapter 4 presents the mechanism of frost wave propagation on hydrophobic and superhydrophobic surfaces during condensation frosting. The significance of individual droplet freezing on frost wave propagation is studied. Chapter 5 presents dynamic defrosting strategies on biphilic and superhydrophobic surfaces. The avenues to further decrease defrost time and provide design methodologies to create effective defrost-enhancing surfaces for industrial applications are explored. Chapter 6 presents a high fidelity model for interfacial pulse-defrosting applications, followed by experimental validation. A fundamental knowledge base for the design of efficient defrosting surfaces is discussed. Chapter 7 presents detailed conclusions from this study.

CHAPTER 2: CONDENSATION ON BIPHILIC SURFACES

2.1 Overview

Dropwise condensation that generally occurs on non-wetting surfaces exhibits 5-10X higher heat transfer coefficient than filmwise condensation. Furthermore, structured superhydrophobic surfaces that exhibit coalescence induced droplet jumping further enhances the condensation heat flux. However, higher supersaturation causes a superhydrophobic surface to flood, resulting in the failure of jumping droplet condensation and drastically decrease the heat transfer coefficient. Here we show, through detailed condensation heat transfer modeling coupled with numerical simulations of binary droplet coalescence, that biphilic surfaces with relatively high *apparent* surface energy spots on a superhydrophobic background surface exhibit 10X higher jumping droplet condensation heat transfer coefficient as compared to homogenous superhydrophobic surfaces. By promoting faster droplet growth rates on the spots, we control the droplet distribution density on the surface, thereby influencing the heat transfer and potentially delay flooding. These findings clarify the role of droplet jumping dynamics and distribution densities during condensation on biphilic surfaces and reveal the optimum design guidelines for biphilic surfaces with maximum condensation heat flux.

2.2 Introduction

Vapor condensation is a preferred mode of heat transfer in a wide range of applications such as building environmental control [38-40], power generation [41], and high-heat-flux thermal management [42]. Water vapor condensing on high- or low-surface-energy surfaces forms a liquid film or distinct droplets, respectively [1,2]. The latter, termed dropwise condensation, is desired

due to its 5-10X higher heat transfer coefficient [43-47]. To further enhance dropwise condensation, researchers have recently proposed the use of suitably designed superhydrophobic surfaces, wherein two or more droplets coalesce on an ultra-low adhesion nanostructured surfaces, the resulting droplet jumps away from the surface, termed as "coalescence induced droplet jumping" governed by inertial-capillary energy conversion [3,4,48-52]. By enabling droplet jumping, the average droplet size on the surface is reduced, decreasing the condensate thermal resistance and enhancing overall heat transfer by $\geq$ 30% when compared to dropwise condensation [5,6]. It has been recently shown that biphilic surfaces, consisting of smooth or rough hydrophilic spots on a superhydrophobic background, can significantly influence droplet size distributions and heat transfer behavior during jumping-droplet condensation [7,8,53,54]. Water droplets nucleating at the hydrophilic spots grow to sizes defined by the biphilic pattern geometry, followed by coalescence and departure. By controlling the spatial geometry and length scale of the hydrophilic spots, enhanced jumping-droplet condensation heat transfer can be obtained through the increase in droplet density. However, it remains unclear what the necessary surface energy requirements are to achieve this "patterned" mode of condensation. Moreover, accurate models that are capable of coupling both droplet-adhesion governed departure dynamics with individual transient droplet heat transfer to predict the overall surface jumping-droplet condensation heat transfer on this class of heterogeneous surfaces do not exist.

In this study, we numerically simulate the individual droplet transient condensation process on a jumping-droplet biphilic surface. The transient simulation captures the varying contact angle droplet growth dynamics on hydrophilic spots, along with the non-constant liquid-vapor interfacial temperature. We utilize our developed model to optimize the design of biphilic surfaces for maximum condensation heat transfer through the coupling of Ohnesorge number dependent

jumping dynamics and finite droplet adhesion on the droplet growth spots. In contrast to the previously used strategy of highly wetting droplet growth spots to achieve ordered droplet growth *via* spatial nucleation control, we explore an alternative strategy of promoting a large droplet growth rate contrast. By promoting significantly faster droplet growth rates on the defined growth spots, a locally hydrophobic (large receding angle) surface wetting state can be used. The result is to significantly reduce the droplet adhesion to extend the range of pattern geometries and droplet Oh where droplet jumping is possible. To validate the accuracy of the model, we performed condensation experiments to characterize individual droplet growth and departure dynamics on biphilic surfaces using optical microscopy. Using our model, we suggest avenues to maximize heat transfer on biphilic surfaces by identifying the critical bottlenecks such as optimization of droplet growth spot size and density-mediated adhesion, with individual droplet growth prior to departure. This work not only provides a more accurate framework for predicting the jumping-droplet condensation heat transfer on biphilic surfaces, but it also offers insights into new avenues for modeling evaporation and frosting phenomena on biphilic surfaces where analogous heat transfer and adhesion dynamics occur.

2.3 Methods

2.3.1 Heat Transfer Model

In this section, I develop a heat transfer model to calculate the condensation heat flux on a superhydrophobic and a biphilic surface building on my previous work [55]. To calculate the overall condensation heat transfer, we first calculate the heat transfer through a water droplet. Then, we multiply the individual droplet heat transfer with the droplet distribution density to get the overall condensation heat flux. To calculate the droplet heat transfer, we study the thermal resistance network. For a droplet residing on a surface, I start with the calculation of the interfacial

7

resistance at the liquid-vapor interface. I calculate the heat transfer coefficient at the liquid-vapor interface of a droplet during condensation.

Interfacial heat transfer coefficient. There have been many interfacial heat transfer coefficient formulae given in the literature, although a generic formula applicable for cases with high supersaturation or polyatomic molecules is lacking. One of the first derivations of the interfacial heat transfer coefficient was done by Schrage [56], where he derived an interfacial heat transfer coefficient associated with mass transfer across a liquid/vapor interface given by

$$h_i = \frac{2\alpha}{2-\alpha} \frac{1}{\sqrt{2\pi R_g T_{sat}}} \frac{h_{fg}^2}{v_g T_{sat}}, \tag{2.1}$$

where R_g is the specific gas constant and v_g is the water vapor specific volume, T_{sat} is the water vapor saturation temperature, and h_{fg} is the latent heat of phase change. During a net condensation process, the coefficient α represents the ratio of vapor molecules that will be captured by the liquid phase to the total number of vapor molecules reaching the liquid surface (ranging from 0 to 1).

The heat transfer coefficient given by Eq. (2.1) is widely used in the literature to model dropwise condensation [57-61]. Rose [62] has shown that the values of condensation coefficient α which can be accepted as most reliable are all close to unity. While in many studies have used Eq. (2.1) for polyatomic molecules , it has been shown that Eq. (2.1) is strictly applicable to monoatomic molecules [62,63]. Another discrepancy in Eq. (2.1) which has been noted in the literature [64-68] is the relation of heat transfer coefficient and the accommodation coefficient, α; the factor $\frac{2\alpha}{2-\alpha}$ is incorrect. Thus, an appropriate interfacial heat transfer coefficient associated with mass transfer across a liquid/vapor interface is desired. Rose [62] proposed a revised condensation heat transfer coefficient based on the theoretical result of Labuntsov & Kryukov [67]. Applying

the principles of the molecular-kinetic theory and solving the linearized Boltzmann equation, Labuntsov & Kryukov [67] calculated the pressure jump at the liquid-vapor interface for low as well as high interphase transfer rates. In the limit of low interphase mass transfer rates ($P_s \approx P_v$ and $T_s \approx T_v$), the pressure jump at the liquid-vapor interface is given by:

$$P_v - P_{sat}(T_S) = \frac{2 - 0.798\alpha}{2\alpha} m \sqrt{2\pi R_g T_{\text{sat}}} , \tag{2.2}$$

where m is the mass flux on the condensing surface. It should be noted that the pressure jump given by Eq. (2.2) has been reported in the literature, [66,69-72] which is obtained from the kinetic equations (Boltzmann equation, BGK model). Note, Eq. (2.2) is strictly applicable for a monotomic gas or hardsphere molecules [66,69-72].

For condensation of saturated vapor, and substituting $Q = mh_{fg}$, Eq. (2.2) can be rearranged to give

$$Q = \frac{2\alpha}{2 - 0.798\alpha} \frac{h_{\text{fg}}}{\sqrt{2\pi R_g T_{\text{sat}}}} (P_v - P_{sat}(T_S)). \tag{2.3}$$

When $(T_v - T_s)/T_s \ll 1$, the Clausius-Clapeyron equation, with linear approximation of the saturation curve, gives

$$\frac{P_{sat}(T_v) - P_{sat}(T_S)}{T_v - T_s} = \frac{h_{fg}}{T_s v_{fg}}. \tag{2.4}$$

Away from the critical point, $v_{fg} \approx v_g$, so Eqs. (2.2), (2.3) and (2.4) can be re-arranged to give

$$h_i = \frac{2\alpha}{2 - 0.798\alpha} \frac{1}{\sqrt{2\pi R_g T_{\text{sat}}}} \frac{h_{\text{fg}}^2}{v_g T_{\text{sat}}}. \tag{2.5}$$

Le Fevre (1964) suggested that for Eq. (2.2) to be valid for diatomic and polyatomic molecules, the pressure jump should by multiplied by $(\gamma + 1)/4(\gamma - 1)$. It should be noted that for

monoatomic molecules the ratio of specific heats, $\gamma = 5/3$, and the correction factor, $(\gamma + 1)/4(\gamma - 1) = 1$. Thus the interface heat transfer coefficient as suggested by Rose [62] becomes

$$h_i = \frac{8\alpha}{2 - 0.798\alpha} \frac{\gamma - 1}{\gamma + 1} \frac{1}{\sqrt{2\pi R_g T_{sat}}} \frac{h_{fg}^2}{v_g T_{sat}},$$

(2.6)

It should be noted that the heat transfer coefficient given by Eq. (2.6) is valid only for low mass flux on the condensing surface, in other words, $P_s \approx P_v$ and $T_s \approx T_v$. Thus, for any arbitrary mass flux, the interpolation expression of mass flux given by Labuntsov & Kryukov [67] using the description asymptotics in the low and high intensity regions should be used,

$$\dot{m}'' = 1.67 \frac{(P_v - P_{sat}(T_S))}{\sqrt{2\pi R_g T_v}} \times \left\{ 1 + 0.515\, ln\left[\frac{P_v}{P_s} \left(\frac{T_s}{T_v} \right)^{0.5} \right] \right\}$$

(2.7)

Thus by combining Eqs. (2), (4), and (7), the interface heat transfer coefficient along with the correction factor suggested by Le Fevre (1964) for non-monoatomic gases becomes

$$h_i = \frac{6.68}{\sqrt{2\pi R_g T_v}} \frac{\gamma - 1}{\gamma + 1} \frac{h_{fg}^2}{v_g T_s} \times \left\{ 1 + 0.515\, ln\left[\frac{P_v}{P_s} \left(\frac{T_s}{T_v} \right)^{0.5} \right] \right\}$$

(2.8)

Note, Eq. (2.8) is valid only for the accommodation coefficient, $\alpha = 1$. If the accommodation coefficient is smaller than unity, an implicit equation given in Labuntsov & Kryukov [67] should be solved to calculate the mass flux. When the interphase transfer rate is low-intensity ($P_s \approx P_v$ and $T_s \approx T_v$), Eq. (2.8) becomes equivalent to Eq. (2.6). When the interphase transfer rate is no longer low-intensity, Eq. (2.6) under predicts the interface heat transfer coefficient.

It should be noted that all the above analysis is done for a planar interface. At the liquid-vapor interface of small droplets, Eq. (2.8) over predicts the interface heat transfer coefficient. Umur and Griffith (1965)[73] used the Kelvin correction to solve for the heat transfer coefficient at the liquid-vapor interface for hemispherical droplets and reported the heat transfer coefficient to be equal to Eq. (1) multiplied by a factor $(1 - \frac{r^*}{r})$ where r^* is the critical radius. Thus, Eq. (2.8)

is updated accordingly for the Kelvin correction, the interface heat transfer coefficient after taking

into account the droplet curvature effects is

$$h_i = \frac{6.68}{\sqrt{2\pi R_g T_v}} \frac{\gamma - 1}{\gamma + 1} \frac{h_{fg}^2}{v_g T_s} \times \left\{ 1 + 0.515 \, ln \left[\frac{P_v}{P_s} \left(\frac{T_s}{T_v} \right)^{0.5} \right] \right\} \left(1 - \frac{r^*}{r} \right) \tag{2.9}$$

Droplet Growth Model. To calculate the theoretical droplet growth rate (dR/dt), the

individual droplet heat transfer $Q(R, \theta)$ is related to the droplet growth rate by the latent heat of

phase change [59]

$$Q(R, \theta) = \dot{m} h_{fg} = \rho_w h_{fg} \frac{dV}{dt} = \frac{\pi}{3} \rho_w h_{fg} \frac{d}{dt} [(1 - \cos\theta)^2 (2 + \cos\theta) R^3] \tag{2.10}$$

where ρ_w, θ, R and V is the density, contact angle, radius and volume of the water droplet

respectively. The heat transfer through an individual droplet, $Q(R, \theta)$ is obtained from a model

given in literature [55]. The convective interfacial heat transfer coefficient given by Eq. (2.9) is

combined with the conductive thermal resistance of the droplet to obtain $Q(R, \theta)$ [55]. There are

two modes of droplet growth – Constant Contact Angle (CCA) and Constant Contact Line (CCL).

In CCA mode, the droplet grows on a surface by maintaining a constant contact angle, with a

monotonous increase in the droplet base area. Whereas, in the CCL mode, the contact line of the

droplet, also known as the three-phase line is pinned to the surface during the droplet growth. In

CCL, the contact angle of the droplet increases monotonously whereas the droplet base area

remains constant. Accordingly, the droplet growth dynamics for CCA and CCL are different

[7,60].

To calculate the droplet growth rate for CCA mode, we differentiate Equation (2.10) with respect to R, we get an explicit term for dR/dt

$$Q(R,\theta) = \pi \rho_w h_{fg} R^2 \frac{dR}{dt} \left\{ (1 - \cos^2 \theta)^2 \sin \theta \frac{d\theta}{dR} R + (1 - \cos \theta)^2 (2 + \cos \theta) \right\}. \qquad (2.11)$$

For CCA, the contact angle with respect to R remains constant, $d\theta/dR = 0$. Rearranging Eq. (11), we get the theoretical droplet growth rate for CCA mode:

$$\frac{dR}{dt} = \frac{Q_{CCA}(R,\theta)}{\pi \rho_w h_{fg} R^2 \{ (1 - \cos \theta)^2 (2 + \cos \theta) \}}, \qquad (2.12)$$

where $Q_{CCA}(R,\theta)$ is individual droplet heat transfer across a droplet in CCA mode.

To calculate the droplet growth rate for CCL mode, the time derivative of droplet volume in Equation (2.10) can be represented as,

$$\frac{dV}{dt} = \frac{dV}{d\theta} \cdot \frac{d\theta}{dt} = \frac{\pi D_b^3}{32 \cos^4 \left(\frac{\theta}{2} \right)} \cdot \frac{d\theta}{dt}, \qquad (2.13)$$

where D_b is the droplet base diameter, $D_b = 2R \sin \theta$. Substituting Equation (2.13) in Equation (2.10), we get

$$\frac{d\theta}{dt} = \frac{32 \, Q_{CCL}(R,\theta)}{\pi \rho_w h_{fg} D_b^3} \cdot \cos^4 \left(\frac{\theta}{2} \right). \qquad (2.14)$$

where $Q_{CCL}(R,\theta)$ is the individual droplet heat transfer across a droplet in CCL mode. Since, the droplet base diameter is constant for CCL, $dD_b/dt = 0$. Differentiating the equation, $D_b = 2R \sin \theta$ with respect to time, and substituting it in Equation (14) we get:

$$\frac{dR}{dt} = -\frac{32 \cdot R \cdot Q_{\text{CCL}}(R,\theta)}{\pi \rho_{\text{w}} h_{\text{fg}} D_{\text{b}}^3} \cdot \frac{\cos\theta}{\sin\theta} \cdot \cos^4\left(\frac{\theta}{2}\right).$$

(2.15)

Equation (2.15) governs the theoretical droplet growth rate for the CCL mode.

To calculate the individual droplet heat transfer, we use the model developed by Chavan *et al.* [55] The individual droplet heat transfer, characterized by the droplet Nusselt number (Nu), is a function of the Biot number (Bi) and apparent advancing contact angle (θ_{a}), *i.e.* Nu = $f(\text{Bi}, \theta_{\text{a}})$. Here, the Nusselt and Biot numbers are defined in terms of the droplet base radius (R_{b}) as: [74]

$$\text{Bi} = \frac{h_{\text{i}} R_{\text{b}}}{k_{\text{w}}},$$

(2.16)

$$\text{Nu} = \frac{Q}{k_{\text{w}} R_{\text{b}}(T_{\text{sat}} - T_{\text{s}})},$$

(2.17)

where Q is the heat transfer through the droplet and k_{w} is the droplet thermal conductivity. The thermal resistance associated with the conduction through the droplet and condensation at the liquid vapor interface is calculated as:

$$\psi_{\text{c}} = \frac{1}{k_{\text{w}} R_{\text{b}} \text{Nu}}.$$

(2.17)

To calculate the overall individual droplet heat transfer, we calculate the overall thermal resistance for the CCA mode and the CCL mode. The CCA mode of droplet growth is observed on the nano-

structured SHP surfaces wherein, the droplet is present on the top of nanostructured pillars. The thermal resistance of air gap and nano pillars beneath the water droplet is given by:[59]

$$\psi_{\text{gap}} = \frac{1}{k_{\text{HC}}\pi R^2 \sin^2\theta} \left[\frac{k_{\text{P}}\phi}{\delta_{\text{HC}}k_{\text{P}} + hk_{\text{HC}}} + \frac{k_{\text{w}}(1-\phi)}{\delta_{\text{HC}}k_{\text{w}} + hk_{\text{HC}}} \right]^{-1}, \tag{2.18}$$

where k_{air} is the thermal conductivity of air, k_{P} is pillar thermal conductivity, h is the height of pillars, δ_{HC} is the coating thickness of the silane, ϕ is the structured surface solid fraction, k_{w} is thermal conductivity of water, and k_{HC} is the coating thermal conductivity. The total thermal resistance for a droplet growing in CCA mode is, $\psi_{\text{tot,CCA}} = \psi_{\text{c}} + \psi_{\text{gap}}$. The individual droplet heat transfer for CCA mode is:

$$Q_{\text{CCA}}(R,\theta) = \frac{\Delta T}{\frac{1}{k_{\text{HC}}\pi R^2 \sin^2\theta} \left[\frac{k_{\text{P}}\phi}{\delta_{\text{HC}}k_{\text{P}} + hk_{\text{HC}}} + \frac{k_{\text{w}}(1-\phi)}{\delta_{\text{HC}}k_{\text{w}} + hk_{\text{HC}}} \right]^{-1} + \frac{1}{k_{\text{w}}R_{\text{b}}\text{Nu}}}, \tag{2.19}$$

where $\Delta T = T_{\text{sat}} - T_{\text{s}}$ is the temperature difference between saturated vapor and substrate.

The CCL mode is observed on biphilic surfaces, wherein water nucleates on the flat growth sites of a biphilic surface with an SHP background. The water droplet is pinned at the edges of the spot. During the droplet growth during CCL mode, the total thermal resistance for the heat transfer is the addition of the droplet thermal resistance, ψ_{c} (Eq. (2.17)), and the thermal resistance of hydrophobic coating, ψ_{coat}. The thermal resistance of the hydrophobic coating is given by:

$$\psi_{\text{coat}} = \frac{\delta_{\text{HC}}}{k_{\text{HC}}\pi R^2 \sin^2\theta}, \tag{2.20}$$

The individual droplet heat transfer for CCL mode is:

$$Q_{CCL}(R, \theta) = \frac{\Delta T}{\dfrac{\delta_{HC}}{k_{HC}\pi R^2 \sin^2\theta} + \dfrac{1}{k_w R_b Nu}},$$

(2.21)

Substituting Eq. (2.19) in Eq. (2.12) and Eq. (2.21) in Eq. (2.15) gives the theoretical droplet growth rate for CCA and CCL modes respectively.

$$\left.\frac{dR}{dt}\right|_{CCA} = \frac{1}{\pi\rho_w h_{fg} R^2 \{(1 - \cos\theta)^2 (2 + \cos\theta)\}}$$

$$\cdot \frac{\Delta T}{\dfrac{1}{k_{HC}\pi R^2 \sin^2\theta}\left[\dfrac{k_P\phi}{\delta_{HC}k_P + hk_{HC}} + \dfrac{k_w(1 - \phi)}{\delta_{HC}k_w + hk_{HC}}\right]^{-1} + \dfrac{1}{k_w R_b Nu}},$$

(2.22)

$$\left.\frac{dR}{dt}\right|_{CCL} = -\frac{32 \cdot R}{\pi\rho_w h_{fg} D_b^3} \cdot \frac{\cos\theta}{\sin\theta} \cdot \cos^4\left(\frac{\theta}{2}\right) \cdot \frac{\Delta T}{\dfrac{\delta_{HC}}{k_{HC}\pi R^2 \sin^2\theta} + \dfrac{1}{k_w R_b Nu}}$$

(2.23)

Overall condensation heat transfer. To calculate the overall condensation heat flux we combined the individual droplet heat transfer with the total number of droplets on the condensing surface. For a superhydrophobic surface, a droplet distribution theory to account for the fraction of droplets on the surface of a given radius R for the surfaces undergoing shedding and jumping available in the literature is used. For small droplets ($R \leq R_e$), the size distribution $n(R)$ is determined by:[58]

$$n(R) = \frac{1}{3\pi R_e^3 \hat{R}} \left(\frac{R_e}{\hat{R}}\right)^{-\frac{2}{3}} \frac{R(R_e - R_{min})}{R - R_{min}} \frac{A_2 R + A_3}{A_2 R_e + A_3} \exp(B_1 + B_2), \tag{2.24}$$

where, where $\hat{R}$ is the average maximum droplet radius (departure radius), R_e is the radius when droplets growing by direct vapor addition begin to merge and grow by droplet coalescence, R_{min} is the critical nucleation radius for condensing droplets ($\approx$10 nm for water). For large droplets ($R \geq R_e$) growing due to coalescence, the droplet distribution $N(R)$ is determined from:[44]

$$N(R) = \frac{1}{3\pi R_e^2 \hat{R}} \left(\frac{R_e}{\hat{R}}\right)^{-\frac{2}{3}} \tag{2.25}$$

The variables A_1, A_2, A_3, B_1, B_2 are constants associated with droplet sweeping, defined as:[59]

$$A_1 = \frac{\Delta T}{h_{fg}\rho_w(1 - \cos\theta)^2(2 + \cos\theta)} \tag{2.26}$$

$$A_2 = \frac{\theta}{4k_w \sin\theta} \tag{2.27}$$

$$A_3 = \frac{1}{2h_i(1 - \cos\theta)} + \frac{1}{k_{HC}\sin^2\theta}\left[\frac{k_p\phi}{\delta_{HC}k_p + hk_{HC}} + \frac{k_p(1 - \phi)}{\delta_{HC}k_w + hk_{HC}}\right]^{-1} \tag{2.28}$$

$$B_1 = \frac{A_2}{\tau A_1}\left[\frac{R_e^2 - R^2}{2} + R_{min}(R_e - R) - R_{min}^2 \ln\left(\frac{R - R_{min}}{R_e - R_{min}}\right)\right] \tag{2.29}$$

$$B_2 = \frac{A_3}{\tau A_1}\left[R_e - R - R_{min}\ln\left(\frac{R - R_{min}}{R_e - R_{min}}\right)\right] \tag{2.30}$$

$$\tau = \frac{3R_e^2(A_2 R_e + A_3)^2}{A_1(11A_2 R_e^2 - 14R_e R_{min} + 8A_3 R_e - 11A_3 R_{min})} \tag{2.31}$$

For the case of smooth hydrophobic surfaces ($\phi = 1$, $h = 0$, $\delta_{HC} \approx 0$) or nanostructured superhydrophobic surfaces ($h \approx 0$, $\delta_{HC} \approx 0$), A_3 is defined as:

$$A_3 = \frac{1}{2h_i(1 - \cos\theta)} \tag{2.32}$$

The total surface steady state condensation heat flux (q_{tot}) for a superhydrophobic surface is obtained by incorporating the individual droplet heat transfer obtained from equations (2.19) or (2.21), with the droplet size distributions (Equation (2.16) and (2.17)):

$$q_{tot} = \int_{R_{min}}^{R_e} Q(R,\theta)n(R)dR + \int_{R_e}^{\hat{R}} Q(R,\theta)N(R)dR \qquad (2.33)$$

Now, to calculate the condensation heat transfer on a biphilic surface made up of droplet growth spots on a non-wetting background, we use the following assumption: (i) water nucleates preferentially at the spots, (ii) nucleation takes place at all spots, (iii) after nucleation, the droplet grows on the spot in CCL mode with a starting contact angle, θ_i, intrinsic to the surface chemistry (iv) the droplet grows until it coalesces with the neighboring droplet as shown in Fig. 2.1(a), and (v) the droplet jumps off and escapes the surface upon coalescence. The average heat transfer through an individual droplet growing on a biphilic surface is:

$$\bar{Q}(R,\theta) = \frac{\int_{\theta_i}^{\theta_a} Q(R,\theta)\, d\theta}{t_{growth}} \qquad (2.34)$$

where $Q(R,\theta)$ is the heat transfer through an individual droplet obtained from equations (2.19) or (2.21), θ_a is the contact angle of the droplet when it coalesces as shown in Fig. 2.1(a), and t_{growth} is the time taken by the droplet from nucleation to grow until it coalesces and jumps. The number of spots per unit area on a biphilic surface, $N_{biphilic}$ gives us the number of water droplets. The total condensation heat flux on a biphilic surface is calculated as:

$$q_{tot} = \bar{Q}(R,\theta) \cdot N_{biphilic} \qquad (2.35)$$

The overall condensation heat transfer coefficient is calculated by:

$$h_c = \frac{q_{\text{tot}}}{\Delta T} \tag{2.36}$$

where ΔT is the temperature difference between the ambient temperature, T_a and the condensing

surface, T_s ($\Delta T = T_a - T_s$).

2.3.2 VOF Droplet Jumping Model

Numerical Simulations. To study droplet coalescence and subsequent jumping on a

biphillic surface, we simulated the case of symmetric binary coalescence using the volume-of-fluid

(VOF) approach with custom automated mesh adaption to resolve the liquid/gas interface

implemented in a finite-volume solver (Fluent v17.0, Ansys Inc.).

We simulated the cases of symmetric binary coalescence ($N = 2$) using the volume-of-fluid

(VOF) method implemented in a finite-volume solver (Fluent v17.0, Ansys Inc.) with automated

mesh adaption implemented in a user defined function (UDF) to resolve the liquid/gas interface.

Three levels of adaption were allowed providing for a minimum cell volume (V_{min}) with

characteristic length ($V_{min}^{1/3}$) in the interface region of 1.9% the droplet radius. Due to symmetry

only one quarter of the domain was simulated with dimensions of $3R$x$3R$x$5R$, where R is the

simulated initial droplet radius. The simulation domain was bounded by two symmetry planes

where, by definition, the contact angle is single valued at $\pi/2$; two walls specified with a shear-

stress free condition; the droplet wetting wall specified as no-slip and a single valued contact angle

(contact angle hysteresis neglected); and an outlet vent, with backflow direction specified from

neighboring cell, opposite to the droplet wetting wall. To simulate the biphillic surfaces, the droplet

wetting wall was decomposed into two regions at the native mesh level. Distinct single valued

contact angles were specified for each region on the droplet wetting wall; $\theta = 180°$ for the

background surface and $\theta = \theta_r$ at the growth spot. The droplet volume was patched into the

simulation domain corresponding to the to the start of coalescence. The properties of the liquid droplet, the surrounding gas and the interface between them are nominally those of water and humid air at room temperature, which corresponds to a nominal viscosity and density ratio of μ_l/μ_g = 56 and ρ_l/ρ_g = 815, respectively.

The PISO algorithm was used for pressure-velocity coupling. Discretization for pressure, momentum and volume fraction was done with the PRESTO!, QUICK and Geo-Reconstruct algorithms, respectively. The continuum surface force (CSF) model was used to capture surface tension. The VOF implementation is intrinsically volume conserving [ref]. This was confirmed for all simulations by tracking the volume of the droplet phase during the simulations. Good results in reducing spurious velocities were obtained by using Fluent's native smoothing function. One fully-weighted cycle of smoothing at each iteration was found to be suitable for the simulations. Under-smoothing by reducing the weighting for a single smoothing cycle led to poor results. Over-smoothing should also be avoided as this unphysically reduces the local curvature of the bridging region leading to a reduction in the simulated jumping velocity.

Determination of jumping speed from simulations. Droplet jumping speeds were determined from simulations by calculating the mass averaged droplet velocity when the droplet lost contact with the surface. It should be noted that, during the coalescence process the droplet typically loses contact with the substrate twice. The first instance occurs during the initial bridge development where the entrainment liquid from the droplet bulk into the developing bridge region results in loss of contact with the substrate. As the liquid bridge expands, it eventually impacts the substrate leading to a substantial increase in the wetted area of liquid on the substrate. The point

19

of departure was found to correlate well with normal force on the wall reaching a minimum (negative).

2.4 Results and Discussions

Figure 2.1(a) represents the schematic of a biphilic surface. The maximum radius of the water droplet, $R_e = L/2$, where L is the pitch between the biphilic spots. The contact angle of the water droplet prior to coalescence is:

$$\theta_a = \sin^{-1}\left(\frac{D_b}{L}\right) \qquad (2.37)$$

where D_b is the diameter of the biphilic spot. Fig. 2.1(b) represents droplet radius observed from the top view, R_{top} as a function of time during droplet growth on a superhydrophobic and biphilic surface. The receding contact angle of water at the biphilic spot is, $\theta_r = 120°$. For a biphilic surface, we assume that water nucleates at the biphilic spot. Upon nucleation, the water droplet grows in a constant contact angle (CCA) mode, with an advancing contact angle, $\theta_a = 120°$. It grows in the CCA mode until the point the droplet is pinned at the edges of the biphilic spot. After that the droplet grows in a constant contact line (CCL) mode, wherein the droplet base area remains constant. It keeps on growing until it achieves the maximum droplet radius, R_e. Equations (2.22) and (2.23) are used accordingly to calculate the droplet growth rate on a biphilic spot. For a superhydrophobic surface, we assume that the droplet nucleates between the nanostructures and grows in a CCL mode until it is pinned in between two nanostructures as shown in the schematic of Fig. 2.1(b). Since the droplet grows in a CCL mode, with a constant droplet base area and a starting contact angle of 10°, the droplet radius observed from the top view remains constant. The droplet is assumed to start de-pinning when it has a contact angle of $\theta_{a,SHP} = 170°$. Once it starts

de-pinning, we assume that it goes into the Cassie-Baxter state and further grows in CCA mode. As observed in Fig. 2.1(b), the growth rate of a droplet on a biphilic surface is much faster than that of a SHP surface, and at a given instance of time, the size of a droplet on a biphilic surface is 10X than that of a droplet on a SHP surface. Moreover, with an increase in the height of the nanostructures on the SHP surface, we observe that the droplet growth rate on a SHP surface is further retarded.

Figure 2.2(a) represents total condensation heat flux, q_{tot} as a function of maximum droplet radius, R_e for a biphilic surface and a superhydrophobic surface for various advancing contact angle, θ_a. Note, it is assumed that droplet with radius, $R > R_e$ jump off and escape the surface, therefore jumping droplet condensation heat transfer is plotted here. Equations (2.33) and (2.34) are used to calculate the condensation heat flux for a superhydrophobic surface and biphilic surface respectively. For a biphilic surface, the maximum droplet radius on the surface is, $R_e = L/2$, where L is the pitch between the biphilic spots. It is observed that for a given advancing contact angle on a condensing surface, the condensation heat flux on a biphilic surface is 10X than that on a superhydrophobic surface. Furthermore, as θ_a decreases, the heat transfer area at the droplet base increases, decreasing the conduction thermal resistance of the droplet. Thus, with decreasing θ_a, q_{tot} increases. Additionally, it is observed that with decreasing the maximum droplet radius on the surface, q_{tot} increases. It is because with decreasing the maximum droplet size, the average size of the water droplet on the surface decreases, decreasing the thermal resistance. Thus, for enhanced heat transfer, a biphilic surface with lower contact angle and, accordingly, lower pitch between the biphilic spots is preferred.

To better understand the relation between the total condensation heat flux on a biphilic surface, droplet size and the contact angle of the droplet, we plot (Figure 2.3(b)) the condensation

heat transfer coefficient for a biphilic surface as a function of biphilic spot size, D_b and pitch ratio, L/D_b. The relation between the pitch ratio is given by Eq. (2.37). Eq. (2.36) is used to calculate the condensation heat transfer coefficient for a biphilic surface. We notice that for enhanced heat transfer, smaller biphilic spot sizes that result in smaller droplet sizes, and lower pitch ratios that result in lower contact angle are preferred. However, for small droplet sizes, the viscous dissipation increases upon coalescence. Moreover, with decreasing the contact angle, the adhesion of the water droplet to the biphilic spot increases. Increased viscous dissipation upon coalescence and enhanced surface adhesion could result in failure of droplet jumping upon coalescence. The relative significance of viscous forces as compared to inertial forces and surface tension can be determined by the Ohnesorge number:

$$Oh = \frac{\mu}{\sqrt{\rho \gamma R}} \tag{2.37}$$

where μ, γ, ρ, and R are the viscosity, surface tension, density and radius of the droplet. Physically Oh represents the ratio of two time scales, Rayleigh timescale for coalescence, $t_R \sim \sqrt{\rho R^3 / \gamma}$, and the viscocapillary time scale, $t_{visc} \sim \mu R / \gamma$ that characterizes the thinning dynamics of a viscously-dominated thread, $Oh = t_{visc}/t_R$ [75]. The non-dimensional velocity of the jumping droplet is given by:

$$v^* = v \sqrt{\frac{\rho R}{\gamma}} \tag{2.37}$$

where v is the maximum velocity of the jumping droplet. Figure 2.3(c) represents the characteristic velocity, v^* as a function of Oh for a smooth surface with no adhesion ($\theta_a = \theta_r \rightarrow 180°$). We expect the smooth approximation of the droplet jumping surface to be reasonable in comparison to

experiment provided that the surface structure length scale, l, is ~10X smaller than the droplet radius [76]. In this limiting case, we recover a jumping speed $v^* = 0.254$ at Oh = 0.01 (strong inertia) and a jumping cut-off of $Oh_c \approx 0.66$ broadly in-line with previous findings considering the viscosity/density ratio simulated here [48,77-80].

To determine the relation of Oh with the maximum droplet size and contact angle of water droplet during coalescence induced droplet jumping on a biphilic surface, we plot Oh as a function of biphilic spot size, D_b and pitch ratio, L/D_b in Figure 2.3(d). It is observed that Oh increases with decreasing the droplet size and droplet contact angle, whereas the condensation heat transfer coefficient increases as observed in Figure 2.3(b). Thus, there exists an optimum where we can achieve maximum jumping droplet condensation heat transfer on a biphilic surface. To identify the optimal design, we study the droplet jumping dynamics for a given biphilic surface design.

To explore droplet jumping dynamics on the biphilic surface, we implemented a VOF model as described in the methods section. Figures 3(a) and (b) show the time lapse images of the 3D VOF jumping droplet simulations on a biphilic surface, with a biphilic spot receding contact angle, $\theta_{r,spot} = 120°$ and $\theta_{r,spot} = 0°$, respectively for Oh = 0.1 and $L/D_b = 8.35$. It was observed that for a superhydrophlic spot, $\theta_{r,spot} = 0°$, satellite droplets are left behind at the biphilic spots during coalescence induced jumping (Figure 2.3(c)), whereas for a hydrophobic spot, $\theta_{r,spot} = 120°$, no such satellite droplets are formed.

Further simulations were conducted for $0.15 \geq Oh \geq 0.02$ (600 nm $< R_e <$ 30 μm), $3 < L/D_b < 8.4$, and $0 \leq \theta_{r,spot} \leq 120°$ to better understand the droplet jumping dynamics on a biphilic surface. Note, we restricted our simulations to Oh ≤ 0.15 considering a practical lower limit on structure length scale of ~10 nm[5,6] so that $R/l \gtrsim 10$ at the conditions studied here. In Figure 2.4,

we plot the characteristic velocity ratio, v^*/v_{na}^* which is the ratio of characteristic jumping velocity on a biphilic surface to that on a smooth, homogenous surface with no adhesion ($\theta_a = \theta_r \to 180°$) as a function of Oh with varying $\theta_{r,spot}$. Figure 2.4(a), (b) and (c) show the simulation results for a pitch ratio, $L/D_b = 3.16$, 4.18, and 8.35, respectively. In Figure 2.4(a), we observe that for a low pitch ratio ($L/D_b = 3.16$, $\theta_a = 161.5°$) no droplet jumping ($v^* = 0$) takes place for biphilic spots with a receding contact angle, $\theta_{r,spot} < 90°$. Moreover, for biphilic spots with a receding contact angle, $\theta_{r,spot} = 90°$, with increasing Oh, the viscous dissipation and surface adhesion start dominating, thereby resulting in the failure of droplet jumping. By increasing the pitch ratio ($L/D_b = 4.18$, $\theta_a = 166.2°$) as shown in Figure 2.4(b), the Oh at which droplets cease to jump upon coalescence can be pushed further. Additionally, biphilic spots with a receding contact angle, $\theta_{r,spot} = 60°$ exhibit coalescence induced droplet jumping for lower Oh cases. In order to achieve droplet jumping for biphilic surfaces with receding contact angle, $\theta_{r,spot} \to 0°$, the pitch ratio is further increased as shown in Figure 2.4(c) ($L/D_b = 8.35$, $\theta_a = 173.2°$). The pitch ratio, $L/D_b = 8.35$ exhibits coalescence induced droplet jumping for all the studied Oh and $\theta_{r,spot}$. However, note that as observed in Fig. 2.2(b), a high L/D_b leads to lower condensation heat transfer coefficient. To understand the dependence of the droplet jumping dynamics on the receding contact angle of the biphilic spot, we plot the characteristic velocity ratio, v^*/v_{na}^* as a function of $\theta_{r,spot}$ with varying Oh for $L/D_b = 8.35$ in Figure 2.4(d). We observe that for increasing $\theta_{r,spot}$, the droplet adhesion at the hydrophilic spot decreases resulting in an increase v^*/v_{na}^*. Interestingly, for hydrophobic spots with $\theta_{r,spot} = 120°$, the characteristic velocity of the jumping droplet on a biphilic surface is greater than that on a surface with no adhesion, $v_{biphilic}^* > v_{na}^*$, by as much as ~20%. Currently, we have no definite explanation for this observation, but it may be due to perturbations in the excess-surface energy-to-kinetic-energy transfer process during coalescence.

To optimize the biphilic surface design for maximum condensation heat transfer coefficient, we combine the results of VOF droplet jumping simulations with condensation heat transfer model. Figure 2.5 shows the condensation heat transfer coefficient as a function of Oh and pitch ratio, L/D_b. The results of the VOF jumping droplet model are superimposed on Figure 2.5. The area under the curve corresponding to a given $\theta_{r,spot}$ represents the regime where coalescence induced droplet jumping is observed. Above the curve droplets don't jump upon coalescence and remain on the surface. For example, a biphilic surface design with hydrophilic spots ($\theta_{r,spot} \leq 30°$ 60° (?)), a pitch ratio, $L/D_b = 8.35$ and Oh = 0.15 gives a model condensation heat transfer coefficient of $h_c \sim 5\text{x}10^4$ W/m²-K. With increasing $\theta_{r,spot}$, droplets at lower L/D_b and higher Oh are able to jump. For hydrophobic spots ($\theta_r = 120°$) with a low pitch ratio (~3) and Oh = 0.15, the accessible condensation heat transfer coefficient increases to $h_c \sim 2.6\text{x}10^5$ W/m²-K, a 5X increase in comparison to the hydrophilic spot limit.

By taking a strictly thermodynamic view, one expects that hydrophilic spots are necessary to promote the organized growth of condensed droplets on superhydrophobic background surface [refs, Hong Kong, McCarthy, others?]. However, we have shown that hydrophillic spots impose a significant penalty on droplet jumping and, as a result, condensation heat transfer coefficient due to increased adhesion. Moreover, one cannot expect that a practical surface can be realized whereby all nucleation sites down to ~10 nm size can be eliminated from the superhydrophobic background surface. If, instead, we consider the kinetics of the system (Figure 2.1(b)), we suggest that droplet growth rate contrast may achieve the same result on a "biphillic" surface that has the same wettability at the molecular level, but using smooth spots versus the rough background. Recognizing kinetic control as a strategy for ordered droplet condensation significantly expands

the allowable range of pattern geometries where droplet jumping can occur and, thus, the upper limit of the heat transfer coefficient.

Our work has been highly simplified to focus on the idealized situation of binary droplet growth and coalescence. Future work should investigate, in detail, the evolution of droplet size distribution on the surface due to the presence of droplet populations demonstrating distinctly different growth rates. Moreover, surface design strategies should be pursued that provide for large growth rate contrast between droplet growth spots and the superhydrophobic background surface.

2.5 Conclusions

In this study, we couple the individual droplet growth and condensation heat transfer with droplet jumping dynamics to optimize the design of a biphilic surface for maximum heat flux. We show that a biphilic surface has higher droplet growth rate during condensation than a superhydrophobic surface. In contrast to the previously used strategy of highly wetting droplet growth spots to achieve ordered droplet growth, we explored an alternative strategy of promoting a large droplet growth rate contrast. By promoting significantly faster droplet growth rates on the defined growth spots, a locally hydrophobic (large receding angle) surface wetting state can be used. This leads to a significant reduction in droplet adhesion to extend the range of pattern geometries and droplet Oh where droplet jumping is possible. Furthermore, the biphilic surface exhibits 10X higher heat transfer coefficient in comparison to a SHP surface. Biphilic surfaces with lower maximum droplet sizes (higher Oh) and lower contact angles during coalescence are preferred for higher heat flux. To determine the droplet jumping dynamics in this regime, we performed VOF numerical simulations of coalescence induced droplet jumping. The numerical simulations show that for hydrophilic spots, higher pitch ratios (high contact angle) and lower Oh are required to observe coalescence induced droplet jumping, whereas hydrophobic spots exhibit

26

jumping at higher Oh and lower contact angle, enhancing the heat flux. The characteristic velocity of jumping droplets on a biphilic surface with hydrophobic spots was higher than a surface with no adhesion. The results of the numerical model are superimposed on the condensation heat transfer model to optimize the design of a biphilic surface for maximum condensation heat flux. This study not only provides a more accurate framework for predicting the jumping-droplet condensation heat transfer on biphilic surfaces, it offers insights into biphilic surface design methodologies to achieve maximum condensation heat flux.
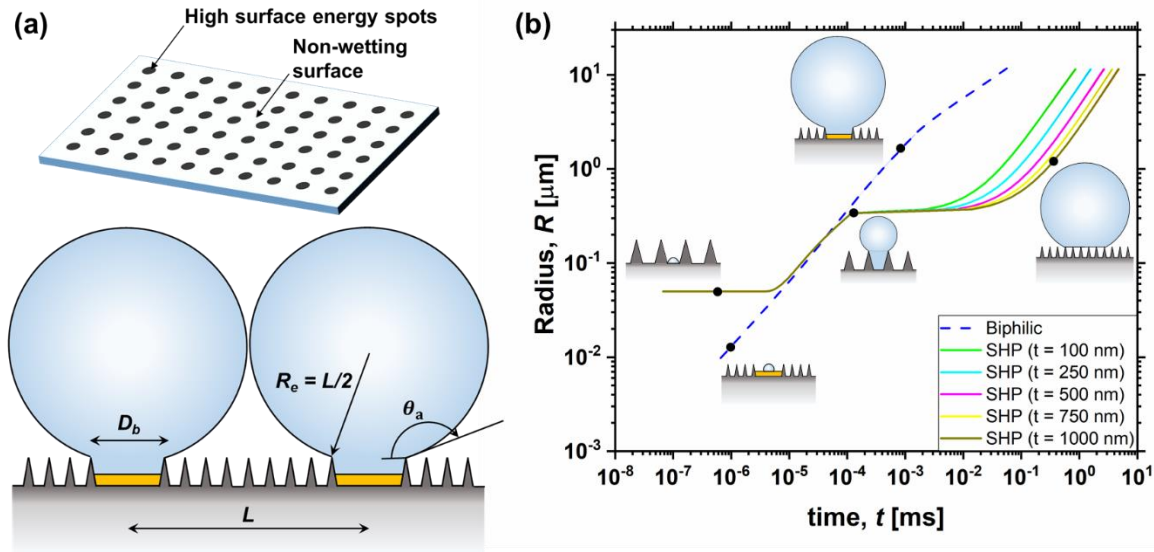
2.6 Figures

Figure 2.1. (a) Schematic of a biphilic surface from isometric view and side view. (b) Radius of the water droplet viewed from the top view direction as a function of time for a biphilic surface and superhydrophobic surfaces with varying pillar heights, t. The droplet radius is calculated theoretically from Eq. (2.22) and Eq. (2.23). For a biphilic surface, it is assumed that the water droplet nucleates at the biphilic spot (spot radius, $R_b = 2$ µm), which has a receding contact angle, $\theta_{r,spot} = 120°$. After nucleation, the droplet grows in a constant contact angle fashion until the edge of the droplet base matches the biphilic spot edge, after which the droplet grows in a constant contact line fashion. For a superhydrophobic surface, it is assumed that the droplet nucleates in the gap between the pillars with top view droplet radius, $R = 50$ nm. After nucleation, the droplet grows in a constant contact line fashion until the advancing contact angle of the water droplet reaches, $\theta_a = 170°$, after which the droplet grows in a constant contact angle fashion. With an increment in the pillar height on a superhydrophobic surface, the conduction resistance offered by the air gaps increases, delaying the droplet growth. Note, droplet growth rate for a biphilic surface is an order of magnitude higher than a superhydrophobic surface. The higher droplet growth rate on a biphilic surface leads to enhanced coalescence induced jumping droplet removal, leading to higher heat transfer.
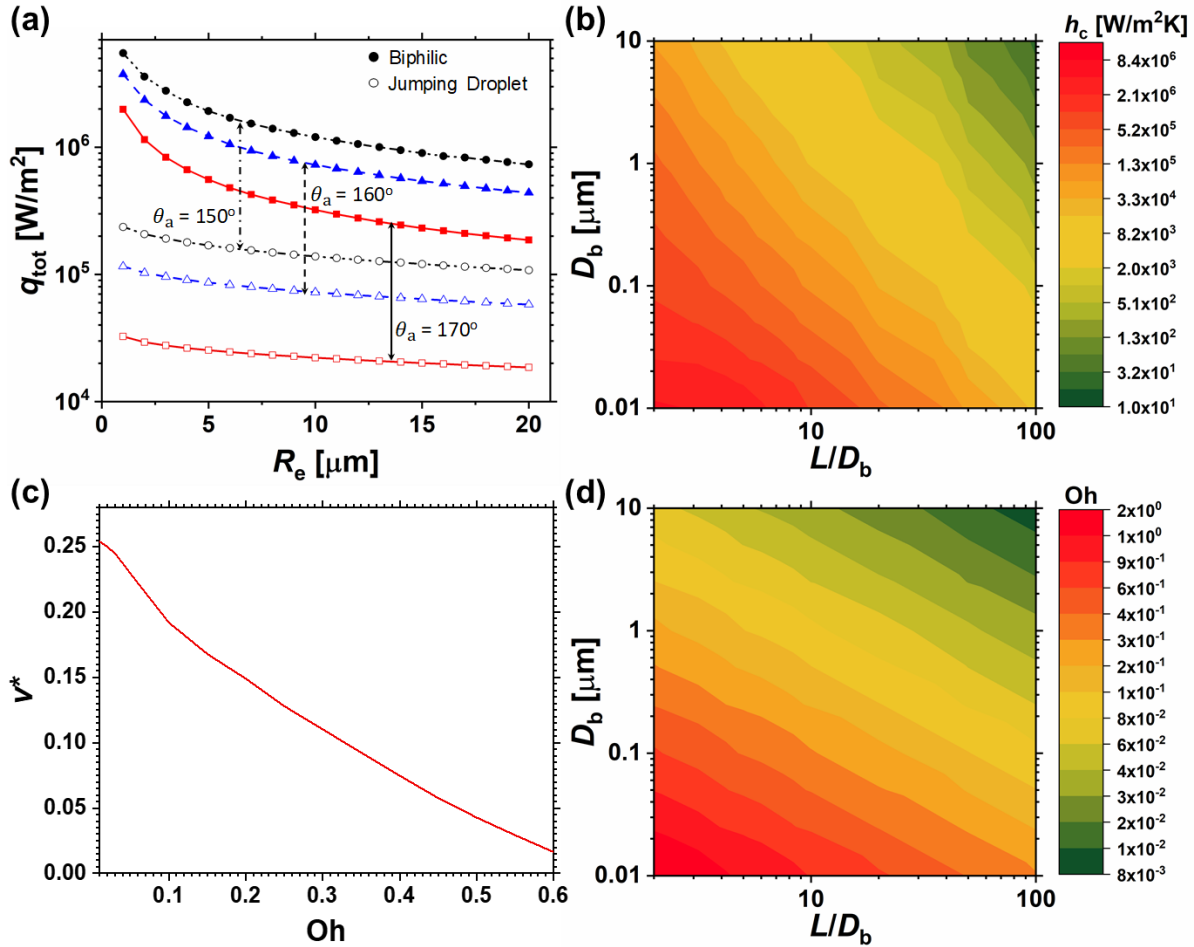
Figure 2.2. (a) Total condensation heat flux, q_{tot} as a function of maximum droplet radius, R_e for a biphilic surface and a superhydrophobic surface for various advancing contact angle, θ_a. (b) Total condensation heat transfer coefficient on a biphilic surface, h_c as a function of spot diameter on a biphilic surface, D_b and pitch ratio of the biphilic spots, L/D_b. Lower D_b and L/D_b is preferred for higher h_c. (c) Non-dimensional droplet jumping speed as a function of Ohnesorge number, Oh, on a smooth, homogenous surface with contact angle $\theta = 180°$. The properties of the liquid droplet, the surrounding gas and the interface between them are nominally those of water and air at 20 °C, which corresponds to a viscosity and density ratio of $\mu_l/\mu_g = 56$ and $\rho_l/\rho_g = 815$, respectively. (d) Ohnesorge number, Oh as a function of spot diameter on a biphilic surface, D_b and pitch ratio of the biphilic spots, L/D_b. For low D_b and L/D_b, h_c as well as Oh increases, indicating that coalescence induced droplet jumping may not be feasible in the regimes where h_c is maximum. Thus, an optimum exists corresponding to maximum condensation heat transfer possible on a biphilic surface.
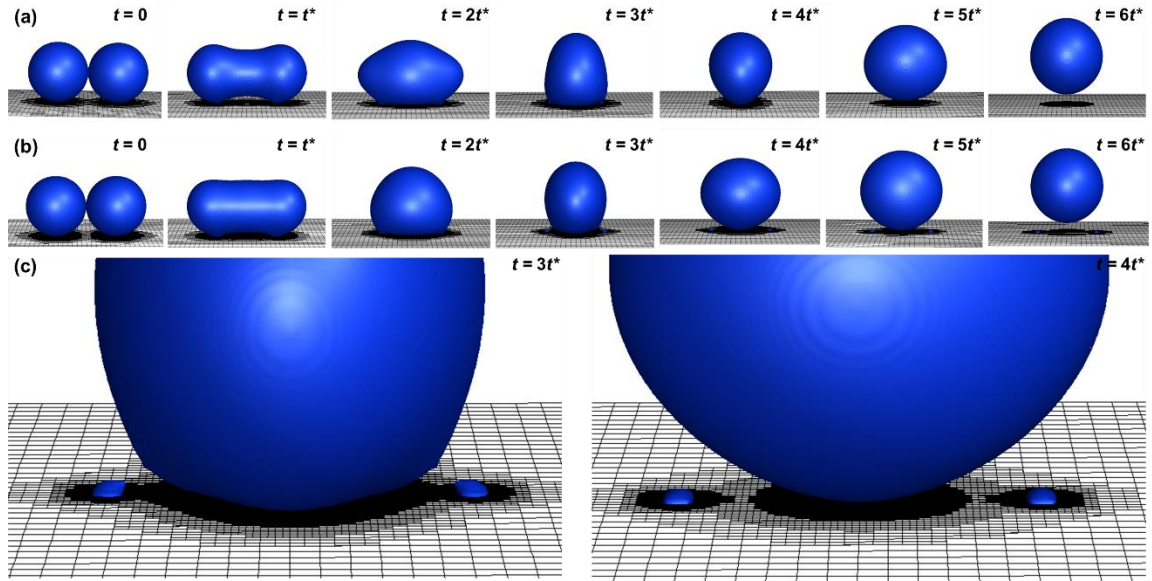
Figure 2.3. Time-lapse images of the 3D VOF droplet jumping simulations on a biphilic surface, with biphilic spot receding contact angle, (a) $\theta_{r,spot} = 120°$ and (b) $\theta_{r,spot} = 0°$. Oh $= 0.1$ and L/D_b $= 8.35$ for all the simulations. (c) Zoomed in images for $\theta_{r,spot} = 0°$. For a superhydrophlic spot, $\theta_{r,spot} = 0°$, satellite droplets are left behind at the biphilic spots during coalescence induced jumping whereas for hydrophobic spot, $\theta_{r,spot} = 120°$, no such satellite droplets are formed.
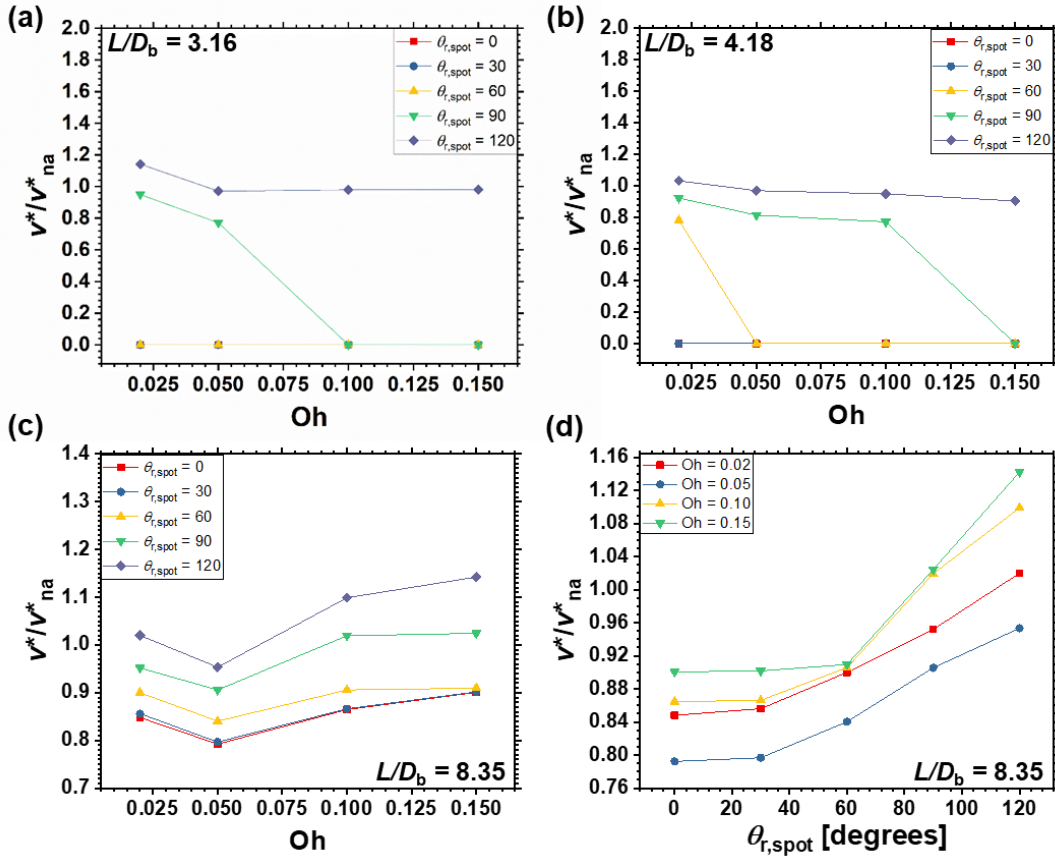
Figure 2.4. Characteristic velocity ratio, v^*/v_{na}^* as a function of Oh with varying $\theta_{r,spot}$ for pitch ratios, (a) $L/D_b = 3.16$, (b) $L/D_b = 4.18$, and (c) $L/D_b = 8.35$. With an increase in the pitch ratio, coalescence induced droplet jumping is observed even for hydrophilic spots. For $L/D_b = 8.35$, coalescence induced droplet jumping is observed even for superhydrophilic spots ($\theta_{r,spot} = 0$) for all the Oh explored. (d) Characteristic velocity ratio, v^*/v_{na}^* as a function of $\theta_{r,spot}$ with varying Oh for $L/D_b = 8.35$.
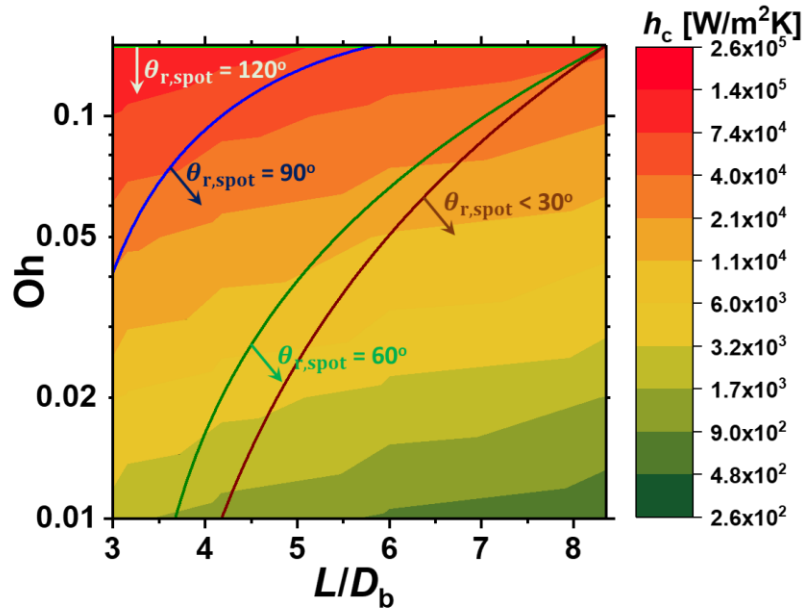
Figure 2.5. Overall Condensation heat transfer coefficient, h_c as a function of Oh and L/D_b with regime maps indicating the regime where coalescence induced droplet jumping is feasible for various $\theta_{r,spot}$. The area below the lines for various $\theta_{r,spot}$ marked by arrows represent the regime where, from simulation, coalescence induced droplet jumping is expected. Note, biphilic spots with $\theta_{r,spot} = 120°$ and a pitch ratio of $L/D_b \approx 3$ show maximum total condensation heat transfer coefficient.

CHAPTER 3: BULK WATER FREEZING DYNAMICS

3.1 Overview

In this chapter, we elucidate the mechanisms governing the heat-transfer mediated, non-thermodynamic, freezing delay on non-wetting surfaces for a variety of characteristic length scales, L_c (volume/surface area, 3 mm $< L_c <$ 6 mm) using carefully designed freezing experiments in a temperature-controlled, zero-humidity environment on thin water slabs. To probe the effect of surface wettability, we investigated the total time for room temperature water to freeze into ice on superhydrophilic ($\theta_a^{app} \to 0°$), hydrophilic ($0° < \theta_a < 90°$), hydrophobic ($90° < \theta_a < 125°$), and superhydrophobic ($\theta_a^{app} \to 180°$) surfaces. Our results show that at macroscopic length scales ($>$ 100 µm), heat conduction through the water-ice layer ($\sim k/L_c$) dominates the freezing process when compared to heat conduction through the functional coatings or nanoscale gaps ($\sim k_{air}/t$) at the superhydrophobic surface-water interface. In order to verify our findings, and to determine when the surface structure thermal resistance approaches that of the water/ice resistance, we fabricated and tested additional substrates coated with commercial superhydrophobic spray coatings, showing a monotonic increase in freezing time with coating thickness. The added thermal resistance of thicker coatings was much larger than that of nanoscale superhydrophobic features, which reduced the droplet heat transfer and increased the total freezing time. Transient finite element method heat transfer simulations of the water slab freezing process were performed to calculate the overall heat transfer coefficient at the substrate-liquid interface during freezing, and shown to be in the range of 1 to 2.5 kW/m²K. The results shown here suggest that in order to exploit heat transfer mediated freezing delay at larger length scales (~ 1mm), thicker

superhydrophobic coatings must be deposited on the surface, where the coating resistance is comparable to the droplet conduction resistance.

3.2 Introduction

Ice formation and accretion present serious economic and safety issues for many industrial applications such as aircraft, power lines, wind turbines, and HVAC&R equipment [10-12,31,81-84]. In order to delay ice nucleation via thermodynamic energy barriers, superhydrophobic surfaces have been the focus of study in recent decades [19,85-94]. Cooling of the superhydrophobic surfaces to subzero temperatures facilitates the formation of metastable supercooled spherical condensate that enables delayed frosting compared to traditional hydrophilic or hydrophobic surfaces [95-99]. Increased hydrophobicity, decreased solid-liquid contact area of the spherical condensate, and higher thermodynamic energy barriers for ice nucleation were responsible for the freezing delay [95,97,98].

Water droplets residing on suitably designed superhydrophobic surfaces exhibit the Cassie-Baxter wetting state, where droplets reside on the tops of the micro/nanostructured features [1,2]. Previous studies have shown that the presence of the air-gaps beneath small water droplets (droplet volume = 1.2 mL, characteristic length scale: 0.5 mm $< L_c <$ 2.5 mm) act as a thermal insulation blanket, and delay the time required to transiently cool the droplet to the melting point (0°C) when compared to hydrophobic surfaces having identical droplet shape and equivalent projected solid-liquid contact area [100,101]. Interestingly, a simplistic scaling-based comparison of the thermal resistances associated with conduction through the water droplet ($\sim L_c/k_{water}$) and conduction through the microscale air gaps (t/k_{air}) reveals that no such freezing delay should be observable for microscale, or macroscale water freezing ($L_c/k_{water} \gg t/k_{air}$), where k_{water} and k_{air} are the

thermal conductivities of water and air, respectively, and t is the thickness of nanoscale air gaps. The non-intuitive results beg the question: at what droplet length scales does the droplet conduction resistance become more dominant than the interfacial air-gap resistance? In an attempt to answer this important question, we performed careful freezing experiments in a temperature-controlled, zero-humidity, nitrogen environment on thin water columns having characteristic length scales L_c, (volume/surface area) greater than 2 mm, radii $R = 9.5, 12.8$ mm, and heights $L = 4, 6$ mm. Freezing time, t_f was characterized as the total time taken by the water column to freeze completely. Time zero was defined as the instant when the room temperature liquid water was deposited onto the chilled substrate. The end point of freezing time, t_f is defined when the whole water column is converted to solid ice. Thus the freezing time, t_f consists of the summation of the time taken by the water column to sensibly cool from room temperature to the melting temperature and the time taken by the ice wave front to completely propagate vertically through the water column after nucleating at the substrate-liquid interface. To probe the effect of surface wettability (air gaps), we fabricated aluminum and copper based superhydrophilic ($\theta_a^{app} \rightarrow 0°$), hydrophilic ($0° < \theta_a < 90°$), hydrophobic ($90° < \theta_a < 125°$), and zero-adhesion superhydrophobic ($\theta_a^{app} \rightarrow 180°$) nanostructured ($t < 1\,\mu m$) substrates. All of our experiments were initiated to freeze with an artificial nucleation site, eliminating the presence of metastable water supercooling and nucleation based freezing delay, and increasing substrate-to-substrate consistency. Our results showed that at millimetric length scales, heat conduction through the water-ice layer ($\sim k/L_c$) dominates the freezing process when compared to conduction through the nanoscale gaps ($\sim k_{air}/t$) at the superhydrophobic surface-water interface ($L_c/k \gg t/k_{air}$). The difference in the experimental freezing times between all tested (smooth or nanostructured) substrates was less than $\pm 10\%$ of the measured value, independent of the surface wettability. In order to verify our findings, and to

determine when the coating thermal resistance approaches the water/ice resistance, we fabricated and tested additional substrates coated with a commercial superhydrophobic spray coating (NeverWet). To control the thickness of the coatings, the number of spray-dry cycles (n) was controlled ($1 < n < 6$). The thicker commercial coatings ($t > 400 \, \mu m$ for $n = 5$) showed a monotonic increase in freezing time with n. The added thermal resistance of the thicker coatings was much larger than that of the nanoscale (~500 nm) superhydrophobic features, which reduced the droplet heat transfer and increased the total freezing time ($L_c/k_{water} \sim t/k_{coating}$). To gain an understanding of the critical length scales where the droplet conduction resistance approaches the nanoscale air-gap resistance, we performed transient finite element method (FEM) heat transfer simulations of the water slab freezing process to calculate the overall heat transfer coefficient at the substrate-liquid interface for a given experimental freezing time. The model results confirmed our scale dependent findings that for small overall heat transfer coefficient discrepancies between the hydrophobic and superhydrophobic surfaces, the difference in freezing time is highly droplet size dependent, being negligible for large droplets (~ 1mm), and appreciable for microscale droplets (~ 10µm). The results shown here suggest that in order to delay the freezing process inside the liquid at larger length scales, one must use thicker superhydrophobic coatings on the surface, where the coating resistance is comparable to the liquid/ice conduction resistance. The current study paints a picture of the heat transfer mediated water freezing process on superhydrophobic surfaces in complete compatibility with classical heat transfer analysis.

3.3 Substrate Fabrication

To create surfaces with a range of wettability and to vary the air-gap thickness, copper (with microstructured Ag coating) and nanostructured aluminum hydroxide (Al_2O_3) surfaces were fabricated. To fabricate nanostructured Al_2O_3 samples, commercially available Al 6061 tabs (25

mm x 25 mm x 0.8 mm, 99.90% purity) were first ultrasonically treated in acetone, followed by ethanol for 5 min each. After cleaning, the samples were dried in a clean N_2 stream. The specimens were then immersed into hot deionized water (90˚C) for one hour, followed by removal and rinsing with room temperature deionized water. This enabled boehmite ($Al_2O_3.xH_2O$) formation on the Al surface with sharp, knife-like structures having length scales approaching ≈300 nm. The nanostructured Al surfaces were used as superhydrophilic Al substrates. To functionalize the surface, Heptadecafluorodecyltrimethoxy-silane (HTMS) was deposited using vapor phase deposition.[102] Nanostructured Al substrates were placed in a container with a vial of 1 mL HTMS toluene solution (5% v/v). A lid was placed on top to seal the container, followed by heating in an atmospheric pressure oven at 80˚C for 3 hours. This process allows for the development of a highly conformal coating as the HTMS molecules evaporate from solution and re-deposit on the aluminum samples. Contact angle measurements (MCA-3, Kyowa Interface Science Ltd.) of ≈300 nL droplets on a HTMS coated nanostructured Al surface showed advancing/receding contact angles of $\theta_a{}^{app}/\theta_r{}^{app} \approx 170.4 \pm 1.4° / 165.4 \pm 4.1°$.

To fabricate the microstructured copper samples, commercially available polished multipurpose 110 Cu tabs (25 mm x 25 mm x 0.8 mm) were used (99.90% purity). Each Cu tab was ultrasonically treated in acetone, ethanol and then in isopropyl alcohol (IPA) for 5 min. An electroless galvanic deposition technique was used to coat textured layer of Ag on copper.[103] The cleaned copper tabs were immersed into an aqueous Silver Nitrate ($AgNO_3$, 0.010 mol/L) solution for 20 s, followed by rinsing with room temperature deionized water. The final surface consisted of sharp, knife-like structures having length scales approaching ≈1 µm. The structured Cu substrates with nano-structured Ag coating on it were used as superhydrophilic Cu substrates. To functionalize the surface, the textured Cu tabs were immersed in a solution of HDFT

(3,3,4,4,5,5,6,6,7,7,8,8,9,9,10,10,10-heptadecafluoro-1-decanethiol) and Dichloromethane (CH$_2$Cl$_2$) (1 mol/L) for 5 min, followed by washing with Dichloromethane and drying in a clean N$_2$ stream. Contact angle measurements of ≈300 nL droplets on Ag/HDFT coated Cu surfaces showed advancing and receding contact angles of $\theta_a{}^{app}/\theta_r{}^{app} \approx 173.4 \pm 1.3° / 164.4 \pm 4.7°$.

To fabricate the superhydrophobic spray coated samples, commercially available Cu tabs were spray coated with industrial superhydrophobic sprays (Rust-Oleum 287337 11 Oz. NeverWet Rain Repellent Spray). Contact angle measurements of ≈300 nL droplets on spray-coated Cu surfaces showed advancing and receding contact angles of $\theta_a{}^{app}/\theta_r{}^{app} \approx 164 \pm 4° / 159 \pm 3°$.

To fabricate the hydrophobic samples, commercially available Al (6061) and Cu (tool finished) tabs (25 mm x 25 mm x 0.8 mm, 99.90% purity) were first ultrasonically treated in acetone, followed by ethanol for 5 min each. After cleaning, the samples were dried in a clean N$_2$ stream. To functionalize the surface, Heptadecafluorodecyltrimethoxy-silane (HTMS) was deposited using vapor phase deposition.[102] Cleaned smooth Al and Cu substrates were placed in a container with a vial of 1 mL HTMS toluene solution (5% v/v). A lid was placed on top to seal the container, followed by heating in an atmospheric pressure oven at 80˚C for 3 hours. This process allows for the development of a highly conformal coating as the HTMS molecules evaporate from solution and re-deposit on the Al and Cu samples. Contact angle measurements (MCA-3, Kyowa Interface Science Ltd.) of ≈300 nL droplets on a HTMS coated smooth Al surface showed advancing/receding contact angles of $\theta_a{}^{app}/\theta_r{}^{app} \approx 126.7 \pm 5.5° / 108.6 \pm 3.6°$ and on a HTMS coated smooth Cu surface showed advancing/receding contact angles of $\theta_a{}^{app}/\theta_r{}^{app} \approx$ 146.0 ± 2.1° / 124.2 ± 3.2°. Note, the Cu tabs were tool finished, exhibiting ~ 50 um roughness. Table 3.1 show the wetting characteristics of the surfaces.

3.4 Experimental Methods

In order to study bulk freezing of water on structured superhydrophilic (SHPhil), structured superhydrophobic (SHP), and smooth hydrophilic and hydrophobic surfaces we conducted water freezing experiments by measuring the time taken by a room temperature water column of a certain height to completely freeze to solid ice. Circular water columns resting on the functional surfaces and surrounded by insulating PTFE rings were chosen as the ideal experimental freezing embodiment in order to ensure consistency from substrate to substrate, maximize the liquid-solid contact area, and reduce thermal parasitic losses in the radial direction. Due to geometric similarity, each water column was characterized by its characteristic length L_c, defined as the ratio of the water column volume to the heat transfer area at substrate-liquid interface [101]. In order to identify the effect of L_c, the freezing experiments were performed at a fixed L_c for all wetting and non-wetting substrates.

Figures 3.1a and b show the side view schematic and top view photograph of the experimental apparatus, respectively. Experiments were conducted for cold stage (surface) temperatures of $T_s = -10°C$, and $-20°C$. Hydrophilic (smooth Al and Cu tabs), hydrophobic (smooth Al and Cu tabs coated with HTMS), spray-coated superhydrophobic (Cu tabs coated with Rust-Oleum 287337 11 Oz. NeverWet Rain Repellent Spray), superhydrophilic (smooth Al and Cu tabs coated with Al_2O_3 and Ag nanostructures, respectively), and zero-adhesion superhydrophobic (smooth Al and Cu tabs coated with Al_2O_3/HTMS and Ag/HDFT nanostructures, respectively) substrates were first placed on the cold stage at a prescribed center position. To enhance thermal communication between the substrate and stage, 2mL of water were placed beneath each substrate to fill the microscale gaps. To ensure repeatability, water volumes of 1 mL and 3 mL were tried with negligible difference in freezing time. In addition, successive independent experimental runs

yielded consistent freezing times to within ±5% of the measured time. A hydrophobic ($\theta_a = 91 \pm 4.3°$) cylindrical insulating ring having an inner diameter equal to 25 ± 0.5 mm or 19 ± 0.5 mm was placed on the top of the 25mm x 25mm substrate to retain water from spreading onto the cold-plate surface. The insulating ring also ensured that consistent water column shapes could be obtained with flat menisci, irrespective of the surface wettability. A transparent polymer lid was used to cover the whole setup and to ensure a zero humidity environment by facilitating the supply of clean and dry N_2 in the enclosed space. The flow rate of the N_2 was reduced to an almost stagnant condition in order to avoid convective heat transfer effects. Room temperature ($23.5 \pm 0.5°C$) tap water was injected into the insulating ring from a syringe through a 1mm piercing made in the center of the polymer lid when the substrate temperature reached the desired cold stage temperature. Freezing time, t_f was characterized as the total time taken by the room temperature water column of characteristic length L_c, defined as the ratio of volume of water to the heat transfer area at the solid liquid interface (height of water column), to freeze completely. The end of the freezing process was characterized by manually vibrating the cold stage as a low frequency (≈30 Hz) and amplitude (≈ 1 mm) in order to observe the reflection of a hand held light emitting diode (LED) through the remaining liquid meniscus. Once the column froze completely, oscillation of LED was not observable, indicating complete freezing. Although the freezing observed here was a transient process, the substrate temperature quickly equilibrated to the desired cold stage temperature after injection of the room temperature tap water. It is important to note, nucleation on superhydrophobic substrates would occasionally not initiate due to the formation of a metastable state of supercooled water. To avoid this phenomenon, we used tap water in order to include impurities that can act as nucleation sites. Furthermore, by injecting the water with the syringe touching the surface at the center, we artificially initiated nucleation at the same location

for each substrate. Thus, delayed freezing due to the creation of thermodynamic energy barriers, which is highly dependent on substrate wettability, is not considered in this study.

3.5 Results and Discussion

Figure 3.2 shows the measured freezing time, t_f as a function of characteristic length, L_c (height of the water column) for T_s = -10°C. Interestingly, we did not see any dependence on surface wettability on the total freezing time. The difference in the freezing times, t_f between all samples was less than ± 10% of the measured value. For brevity and clarity, herein, we only focus on smooth hydrophilic (Smooth) and structured superhydrophobic (SHP) substrates to elucidate the effect of nanoscale air gaps on the freezing process. Analysis of the complete data set indicated a quadratic relationship between the freezing time and characteristic length. Assuming that the liquid phase is at the melting temperature of ice, and that the heat capacity of ice is negligible compared to the latent heat of solidification, an energy balance on the propagation of a planar ice-water front during freezing results in:[104,105]

$$v h_{fs} = \rho_{ice} k_{ice} \frac{\partial T}{\partial z},$$
(3.1)

where v is the ice front propagation speed, h_{fs} is the latent heat of fusion, k_{ice} and ρ_{ice} are the thermal conductivity and density of ice, and $\partial T / \partial z$ is the temperature gradient in the direction of ice propagation. Integrating Eq. (3.1) from ice nucleation to complete icing, we see that the total freezing time is proportional to the square of characteristic length is given by

$$t_f = \frac{h_{fs}L_c{}^2}{2k_{ice}\overline{\Delta T}},$$ (3.2)

where, $\overline{\Delta T}$ is the average temperature difference between the melting temperature (0ºC) and the temperature at the base of water column ($\overline{\Delta T} = T_{\text{melting}} - T_{\text{base}}$). Our experimental data agree well with the quadratic trend for $\overline{\Delta T}$ = 5.2ºC (Figure 3.2) . Although the base of the stage temperature was set to T_s = -10ºC, implying that $\overline{\Delta T}_{\text{exp}}$ = 10ºC, the frost propagation model does not account for i) sensible cooling of the liquid water or ice, ii) transient temperature response of the cold stage, or iii) the placement of the stage thermocouple within the stage and not on the sample, all of which would act to decrease the temperature difference $\overline{\Delta T}$, in agreement with our theoretical result [106]. The results indicate that for the length scales tested here, transient conduction through the water/ice column ($\sim k/L_c$) dominated the freezing process as compared to the conduction through the nanoscale gaps on superhydrophobic surface ($\sim k_{\text{air}}/t$). For larger characteristic length scales (L_c > 3 mm), the difference in the experimental freezing time for smooth and structured surfaces was less than ± 10%, indicating that the heat-transfer mediated freezing dynamics of water layers at the measured length scales do not depend on the surface wettability or micro/nanostructure, rather they depend on the characteristic length of the water column. Thus, at the length scales investigated (L_c > 2 mm), superhydrophobic surfaces do not provide any advantage of heat-transfer mediated delayed freezing of water over smooth hydrophilic or even superhydrophilic surfaces. It is important to reiterate, the results presented here do not contain thermodynamic delay in ice nucleation, which is dependent on surface wettability, and rather water begins to freeze as soon as it reaches the melting temperature.

One method to achieve delayed frost wave front propagation inside the liquid at larger length scales is to apply more thermally resistive superhydrophobic coatings such that the thermal resistance at the substrate-liquid interface (t/k_{air}) is of the same order of magnitude as that of the effective conduction thermal resistance inside the water/ice column (L_c/k). As expected, for the nanostructures examined insofar (~500 nm), the critical water column length scales needed to see appreciable heat-transfer mediated delay in freezing time can be estimated as $L_{c,crit} \sim kt/k_{air} \sim$ 25 µm. To validate our hypothesis and to quantify when the interfacial and ice/water conduction regimes intersect, we fabricated and tested additional smooth Cu substrates coated successively with a superhydrophobic spray solution (NeverWet) consisting of functionalized nanoparticle aggregates. To vary the thickness of the coatings, the number of spray-dry cycles (n) was controlled ($1 < n < 6$). Since the procedure used for coating the consecutive spray-dry cycles was kept consistent and done in a controlled fume hood environment, a non-linear, monotonic increase in the coating thickness was observed with increasing n.

Figure 3.3 shows the water column freezing time t_f as a function of number of successive superhydrophobic coating layers on the surface, n, at a surface temperature T_s = -10°C. As expected, the thicker commercial coatings ($t > 400$ µm for $n = 5$) showed a monotonic increase in freezing time as a function of n. The added thermal resistance of the thicker NeverWet coatings was much larger than that of the nanoscale (~500 nm) superhydrophobic features of the Ag and Al$_2$O$_3$ structures, which reduced the droplet heat transfer rate at the liquid-substrate interface and increased the total freezing time. For the NeverWet coatings, the critical water column length scale approached the experimentally tested water column length scale, $L_{c,crit} \sim kt/k_{coating} \sim 3.5$ mm (for $n = 5$, $k_{coating} \approx 0.1$ W/m·K).

To further elucidate the effect of nano- and microscale superhydrophobic surfaces on liquid-solid interfacial heat transfer during freezing, we calculated the overall heat transfer coefficient at the substrate-liquid interface (h) by performing transient FEM simulations of freezing using the materials, geometry, initial conditions, and experimentally measured freezing time as inputs. Prior to turning to FEM, we considered many different modeling approaches to elucidate the coupled stage-water-ice freezing physics. The frost wave propagation model (Eq. 3.1 and 3.2) [104], although appropriate for estimation, fails to take into account sensible cooling of the ice/water phase. Modeling of the freezing process analytically by considering the liquid and the substrate as semi-infinite bodies is also unphysical as it would pin the interfacial temperature to a constant value, until the thermal boundary layer reaches either the cold stage or top of the water surface. As evidenced by our experimental results, the interface temperature was not constant [106]. Modeling the water column as a semi-infinite body with a constant base temperature has been done before for impacting droplets on superhydrophobic surfaces having short contact times, [85] however cannot be applied here due to the inference of an infinite heat transfer coefficient at the bottom interface through the assumption of a constant base temperature. Assuming a constant base temperature boundary condition is unphysical as it leads to transient cooling and ice formation times on the order of milliseconds, something not observed in our results or the results of others [101]. To effectively model the problem, we apply an effective heat transfer coefficient, h, at the base between the constant temperature substrate and the water/ice residing on top of the structures. Note, the heat transfer coefficient approach is also an approximation, as the temperature of the substrate is not constant after water deposition. However, the developed approach is a happy medium between modeling of the entire cold plate assembly with time

resolved heat transfer rates (too cumbersome to obtain more generalized results), and simplistic models assuming constant base temperatures (too inaccurate when compared to real experiments).

To elucidate the effect of nano- and microscale superhydrophobic surfaces on liquid-solid interfacial heat transfer during freezing, we calculated the overall heat transfer coefficient at the substrate-liquid interface (h). A 2D axisymmetric numerical model based on finite element method was used to solve the transient phase change heat equation through water column. The ANSYS Transient Thermal Module was used to model the water column, with triangular meshing as shown in Figure 3.5 with 25,000 nodes. The maximum element size was kept constant for all the cases, element size = 0.125 mm. Mesh refinement was used at the liquid-vapor interface, liquid-side wall interface and solid-liquid interface (element size = 0.05 mm, Figure 3.5). Further reduction in mesh size resulted in < 1% change in the freezing time. Figure 3.4 shows the boundary conditions applied to the model during the simulations.

The input conditions:

- Geometry (size of the water column)
- Overall liquid-substrate interface heat transfer coefficient, h
- Natural convection boundary condition at the liquid-air interface, h_{nc} = 15.3 W/m^{2}K
- Over all heat transfer coefficient at the side wall, h_{sw} ~ 13 W/m^{2}K

h_{nc} and h_{sw} are analytically calculated for natural convection. Sensitivity analysis was done for h_{nc} and h_{sw}, and it was observed that a 10% change in h_{nc} and h_{sw} resulted in < 1% change in the freezing time. For the above input conditions, the total freezing time was calculated. Then, the value of overall liquid-substrate interface heat transfer coefficient, h was varied, such that the calculated freezing time matches the freezing time obtained from experiment for a given

geometry. The overall liquid-substrate interface heat transfer coefficient, h was calculated for all the experimental data points.

Figure 3.6(a) shows h as a function of L_c for the initially tested nanoscale coatings, indicating that for any given substrate wettability, h does not depend on the geometry of the water column. The overall heat transfer coefficient, h, is approximately equivalent for all surfaces for any given L_c due to the negligible thermal resistance of nano-scale gaps beneath the water column. At the length scales tested here, the freezing time is actually being constrained by the conduction of the latent heat through the water/ice column (L_c/k) and not through the interface itself (t/k_{air}), otherwise the calculated h should vary with substrate wettability. For a given L_c, the variation of h for different substrates arises mainly due to the sensitivity of freezing time to the applied h boundary condition in the transient FEM simulation. Although the freezing time was determined not to depend on wettability, the variability of experimentally determined the freezing times was not negligible from experimental run-to-run. The critical thickness of air gap needed to see appreciable delay in freezing time can be estimated as $t_{crit} \sim k_{air}L_c/k_w \sim 40$ µm. To investigate this further, transient FEM freezing simulations were done with an air gap of thickness $t = 1$ µm and 10 µm beneath the water column. As expected, with all other parameters kept constant, there was negligible difference in the total freezing times for flat surfaces and structured surfaces with an air gap of thickness $t = 1$ µm. The critical thickness of air gap needed to see appreciable delay in freezing time can be estimated as $t_{crit} \sim k_{air}L_c/k_w \sim 40$ µm. To investigate this scaling result, transient FEM simulations of freezing were done with an air gap of thickness, $t = 1$ µm and 10 µm beneath the water column. As expected (Figure 3.7), with all other parameters kept constant, there was no appreciable difference in the freezing times for a flat surface (with no air gap, $t = 0$) and a structured surface with air gap thickness of $t = 1$ µm. As the thickness of the air gap approached

$t \to t_{\mathrm{crit}}$, a notable difference in the freezing times for flat surfaces ($t = 0$) and structured surfaces ($t = 10\ \mu\mathrm{m}$) was observed for $1\ \mu\mathrm{m} < L_c < 5\ \mu\mathrm{m}$.

Figure 3.6(b) shows h as a function of the number of successive NeverWet superhydrophobic coatings on the surface (n). The added thermal resistance of the thicker coatings (~100 µm) was much larger than that of the nanoscale (~500 nm) superhydrophobic features, which reduced h and increased the total freezing time.

The present study offers a unique insight into the design of superhydrophobic coatings for anti-icing applications, particularly for heat transfer devices undergoing heat-transfer mediated (non thermodynamic limited) bulk water freezing. One may initially think that the added thermal resistance of thicker superhydrophobic coatings will penalize the heat exchanger performance when freezing is absent. However, the typical convective heat transfer resistance is much larger than the thermal resistance of any added functional coating ($1/h_{\mathrm{air}}A \gg t_{\mathrm{coating}}/k_{\mathrm{coating}}A$), indicating that coating may be worthwhile.

Furthermore, our study brings into question previous results which show that the presence of microscale (1 µm) air-gaps delay the time to transiently cool droplets to the melting point (0°C) [100,101]. Although our work defines the total freezing time as the time required to convert the entire water column from liquid to ice, the results of our FEM analysis reveal that even the initial water sensible cooling to the melting point is negligibly affected by air gaps $\approx 1\mu\mathrm{m}$, and only begins to change once air gap thicknesses approach 10 µm or greater. Interestingly, the insensitivity to short superhydrophobic structures on heat transfer during freezing is in agreement with condensation experiments and theory which stipulate that structure length scales be

minimized to avoid parasitic thermal resistance, and that structure length scales <1 µm have little effect on microscale droplet growth rates [107-112].

3.6 Conclusions

In summary, we have demonstrated that the use of nanoscale superhydrophobic surfaces does not result in the anomalous heat-transfer mediated delay of water freezing. Instead, classical heat transfer effects govern the freezing process irrespective of wettability, indicating that the required liquid length scales must approach the length scale of the coating in order to observe an appreciable effect. Transient freezing FEM simulations revealed that the overall heat transfer coefficient at the column base for freezing on nanoscale superhydrophobic surfaces approaches 2 kW/m^{2}K, irrespective of wettability or column length scale, and reduces monotonically with increased coating thickness. The overall heat transfer coefficient represents the bulk water freezing and coating thermal resistance. A reduction in overall heat transfer coefficient means that the coating resistance has increased (as the bulk water freezing resistance is maintained constant). The results shown here suggest that in order to delay the frost wave front propagation inside the liquid at larger length scales, one must use thicker superhydrophobic coatings on the surface, where the coating resistance is comparable to the liquid conduction resistance.

3.7 Table

Table 3.1. Surface Wetting Characteristics

| Surface ID	Substrate	Structures	Hydrophobic Coating	Advancing angle (degrees)	Receding angle (degrees)
Al – SHPhil	Al	$Al_2O_3.xH_2O$	none	≈20 ± 10°	0°
Cu – SHPhil	Cu	Ag	none	≈20 ± 10°	0°
Al – Smooth	Al	none	none	88.3 ± 4.2°	26.1 ± 2.7°
Cu – Smooth	Cu	none	none	82.6 ± 6.9°	16.5 ± 2.4°
Al – HP	Al	none	HTMS	126.7 ± 5.5°	108.6 ± 3.6°
Cu – HP	Cu	none	HTMS	146.0 ± 2.1°	124.2 ± 3.2°
Al_2O_3 – SHP	Al	$Al_2O_3.xH_2O$	HTMS	170.4 ± 1.4°	165.4 ± 4.1°
Cu – SHP	Cu	Ag	HDFT	173.4 ± 1.3°	164.6 ± 4.7°
Cu – NeverWet	Cu	NeverWet	NeverWet	164 ± 4°	159 ± 3°

3.8 Figures
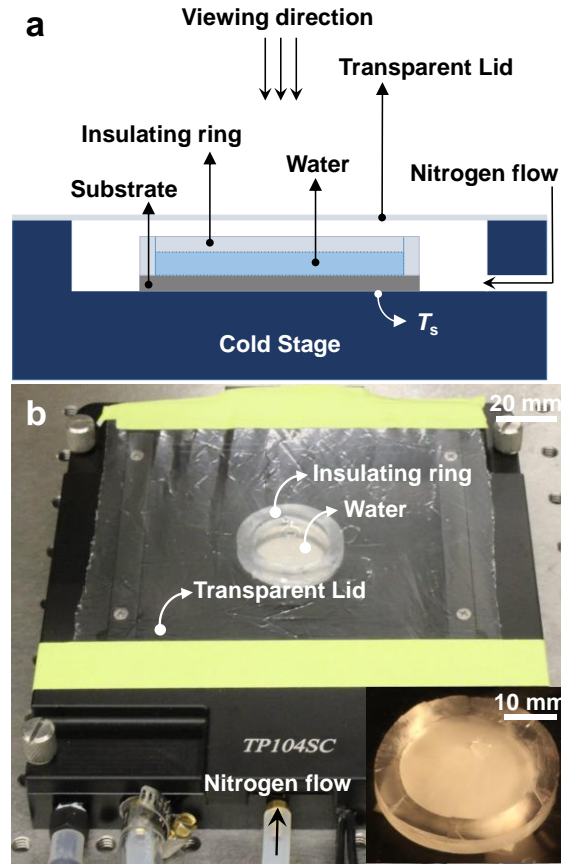
Figure 3.1. a) Side view schematic of the freezing experiment and b) picture of the actual setup. Inset: image of a frozen water column. The cold stage was kept at temperatures T_s = -10ºC, -20ºC. Samples were first placed on the cold stage at a prescribed center position. A hydrophobic cylindrical insulating ring (ID = 25 mm, 19 mm) was placed on the top of the substrate (25 mm x 25 mm) to retain water from spreading onto the cold-plate surface. Room temperature tap water was injected into the insulating ring when the substrate temperature reached the desired cold stage temperature. A transparent lid was used to cover the whole setup and to ensure a zero humidity environment by facilitating the supply of clean and dry N_2 in the enclosed space. Freezing time, t_f was characterized as the total time taken by the water column of height L_c to freeze completely.
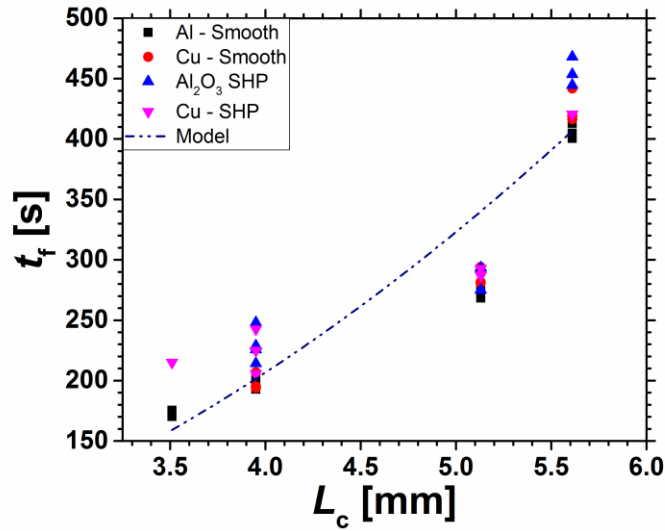
Figure 3.2. Freezing time, t_f as a function of characteristic length, L_c (height of the water column in this case) for surface temperature $T_s = $ -10ºC. The characteristic length and diameter of the water column ranged from 3.5 mm $< L_c <$ 5.6 mm and 19.1 mm $< D <$ 25.4 mm, respectively. The theoretical model reveals that $t_f \sim L_c^2$, [104,105] in excellent agreement well with the experimental data. The results indicate that for the length scales tested here, and in previous work, conduction through the ice/water column ($\sim k/L_c$) dominated the freezing process as compared to the conduction through the nanoscale gaps on superhydrophobic surface ($\sim k_{air}/t$). For larger characteristic length scales ($L_c >$ 3 mm), the difference in the experimental freezing time for smooth and superhydrophobic surfaces was less than $\pm10\%$, indicating that the freezing dynamics of water layers at the measured length scales do not depend on the surface wettability or micro/nanostructure, rather they depend on the characteristic length of the water column. For each substrate, three independent measurement were made and the final result was averaged. The removal of all humidity from the chamber, and consistent water column shape resulted in highly precise measurements ($<$ 5% difference from run to run). Error bars are not included in the graph for clarity (maximum error $\pm5\%$ of measurement).
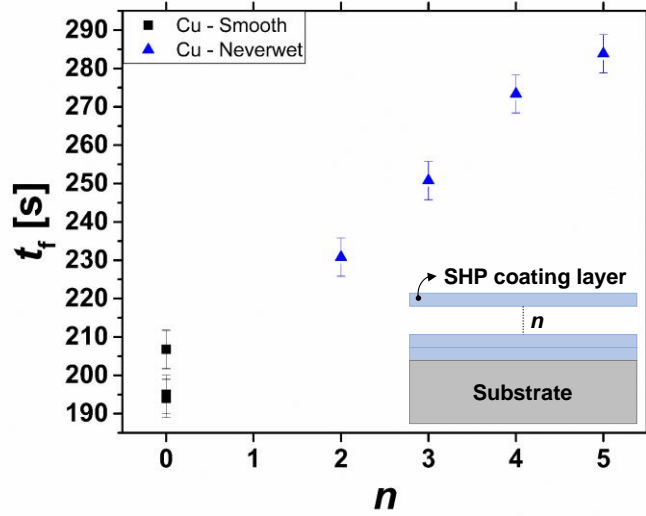
Figure 3.3. Freezing time t_f as a function of number of successive superhydrophobic coating layers (n) on the surface for surface temperature T_s = -10°C and L_c = 3.95 mm. The results show that for single coatings, conduction through the water column ($\sim k_{water}/L_c$) is the freeze limiting step when compared to conduction through the nanoscale gaps on superhydrophobic coatings ($\sim k_{air}/t$). The thicker commercial coatings ($t_{coating}$ > 400 µm for n = 5) showed a monotonic increase in freezing time as a function of n. The added thermal resistance of the thicker coatings was much larger than that of the nanoscale ($\sim$500 nm) superhydrophobic features, which reduced the droplet heat transfer rate at the liquid-substrate and increased the total freezing time ($t_{coating}/k_{coating} \sim L_c/k$). Coating thickness was measured with cross sectioning and optical microscopy.
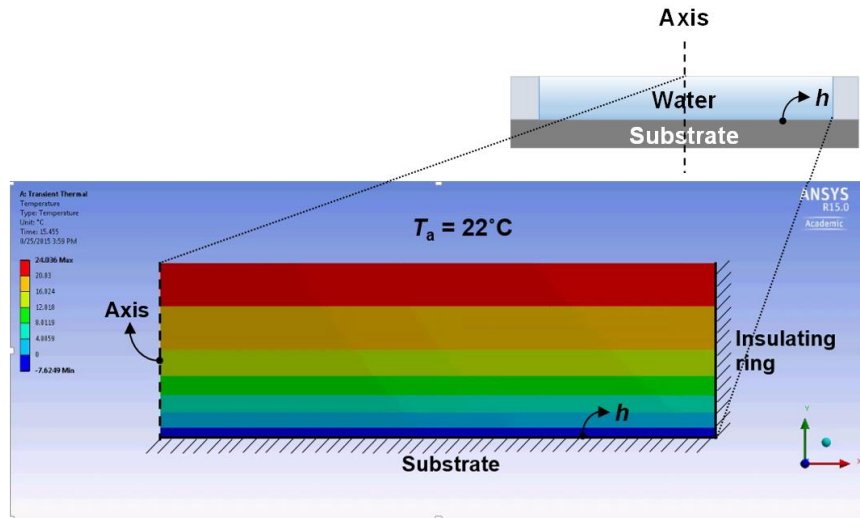
Figure 3.4. The boundary conditions applied to the 2D axisymmetric numerical model.
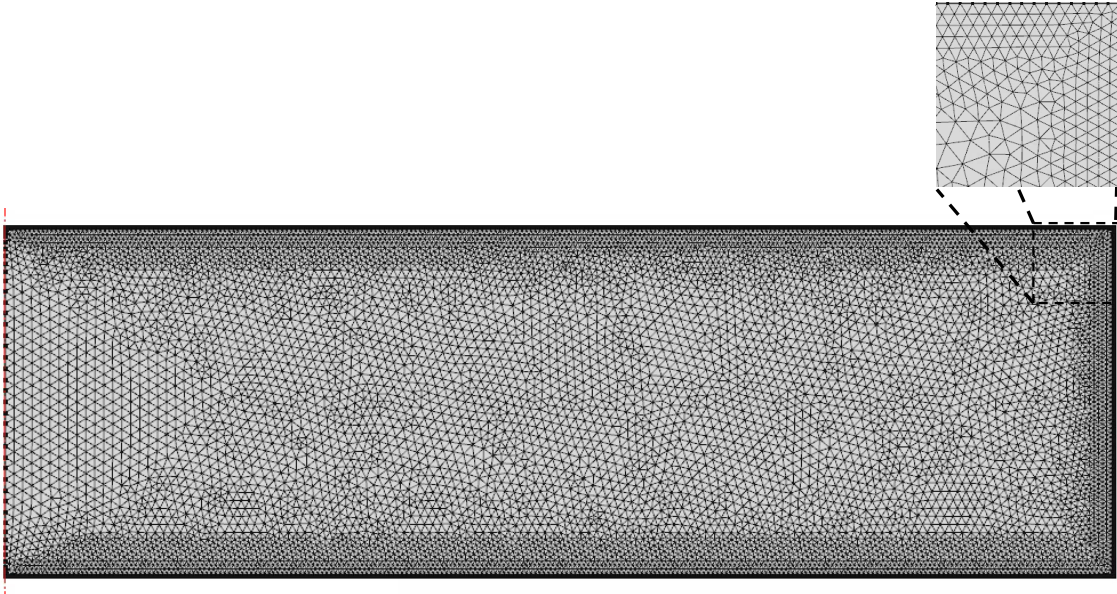
Figure 3.5. Triangular meshing of the water column. Maximum mesh size = 0.125 mm and n, Number of nodes = 25,000.
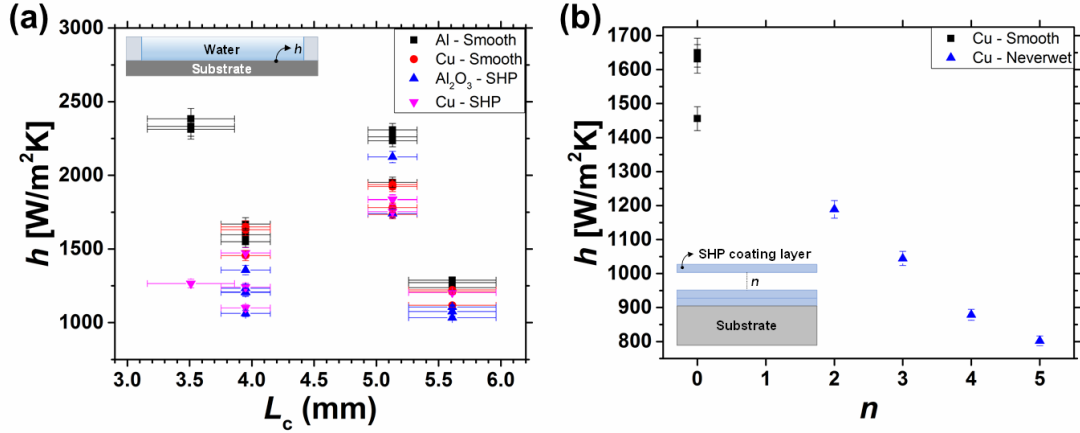
Figure 3.6. a) Surface-liquid interface overall heat transfer coefficient (h) as a function of characteristic length, L_c for surface temperature $T_s = -10°C$. To determine the overall heat transfer coefficient, we performed transient finite element method heat transfer simulations of the water column freezing process using the geometry, initial conditions, and experimental freezing time as input. The results show that for any given substrate type, h does not depend on the geometry of the water column, *i.e.*, its height (characteristic length, L_c) and radius (R). b) Surface-liquid interface overall heat transfer coefficient (h) as a function of the number of successive superhydrophobic coatings on the surface (n) for surface temperature $T_s = -10°C$ and $L_c = 3.95$ mm. The added thermal resistance of the thicker coatings was much larger than that of the nanoscale (~500 nm) superhydrophobic features, which reduced the droplet heat transfer and increased the total freezing time ($t_{coating}/k_{coating} \sim L_c/k$). This resulted in a monotonic decrease in the overall heat transfer coefficient with increasing n.

Figure 3.7. Total freezing time (t_f) as a function of characteristic length scale (L_c) for varying air gap height (t). The diameter of the water column is, $D = 25.4$ mm and characteristic length scales 1 mm $< L_c <$ 5 mm. The overall heat transfer coefficient at the substrate-liquid interface is $h = 3000$ W/m^{2}K.
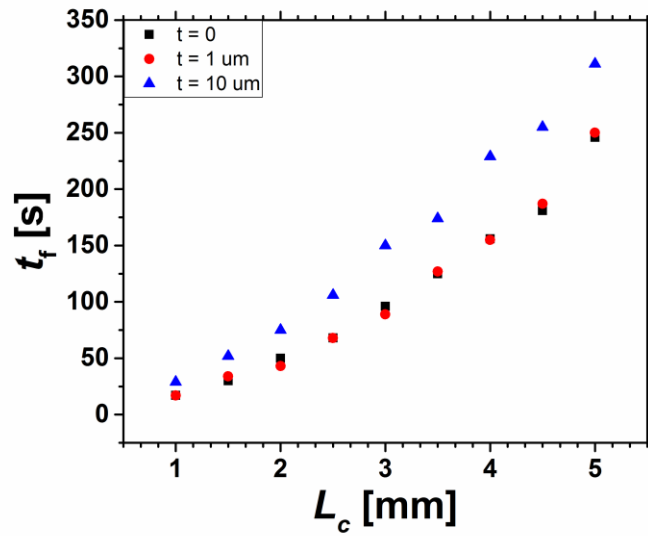
CHAPTER 4: INDIVIDUAL DROPLET FREEZING AND FROST WAVE PROPAGATION

4.1 Overview

Frost spreads on non-wetting surfaces during condensation frosting via an inter-droplet frost wave. When a subcooled condensate water droplet freezes on a hydrophobic or superhydrophobic surface, neighboring droplets still in the liquid phase begin to evaporate. The evaporated water molecules deposit on the frozen droplet and initiate the growth of ice bridges directed toward the water droplets being depleted. Neighboring liquid droplets freeze as soon as the ice bridge connects. Two possible mechanisms govern the evaporation of neighboring water droplets: (1) the difference in saturation pressure of the water vapor surrounding the liquid and frozen droplets induces a vapor pressure gradient, and (2) the latent heat released by freezing droplets locally heats the substrate, evaporating nearby droplets. The relative significance of these two mechanisms is still not understood. In this chapter, we study the significance of the latent heat released into the substrate by freezing droplets, and its effect on adjacent droplet evaporation, by studying the dynamics of individual water droplet freezing for varying droplet radii (10 µm $< R < 100$ µm) on aluminum, copper, and glass-based hydrophilic ($\theta_a < 90°$), hydrophobic ($110°$ $< \theta_a^{app} < 140°$), and superhydrophobic ($\theta_a^{app} > 160°$) surfaces. The latent heat flux released into the substrate was calculated from the measured droplet sizes and the respective freezing times (t_f), defined as the time from initial ice nucleation within the droplet to complete droplet freezing. To probe the effect of latent heat release, we performed 3D transient finite element simulations showing that the transfer of latent heat to neighboring droplets is insignificant, and accounts for a negligible fraction of evaporation during microscale frost wave propagation. Furthermore, we

studied the effect of substrate thermal conductivity on the transfer of latent heat transfer to neighboring droplets by investigating the velocity of ice bridge formation. The velocity of the ice bridge was independent of the substrate thermal conductivity, indicating that adjacent droplet evaporation during condensation frosting is governed solely by vapor pressure gradients. For the length scales tested here ($R > 10$ um), surface wettability had the largest effect on t_f as it governs the droplet conduction thermal resistance, increasing with higher intrinsic and apparent advancing contact angles. This study not only provides key insights into the individual droplet freezing process but also elucidates the negligible role of latent heat released into the substrate during frost wave propagation.

4.2 Introduction

Understanding the mechanisms of frost formation is essential to a variety of industrial applications including refrigeration, [9,10,82] aviation, [11] wind energy, [12] and power transmission [13]. Ice accretion and frost formation is a multi-billion dollar problem in the United States alone [113]. It has been observed that hydrophobic surfaces offer lower frost density and decreased condensation frost growth rate as compared to hydrophilic surfaces [14]. To further delay frost formation, researchers have proposed the use of suitably designed superhydrophobic surfaces [15-17,81] to delay the heterogeneous nucleation of ice [18,19,90,114], and thus condensation frosting [20]. By exploiting the ultra-low adhesion offered by superhydrophobicity, [115] droplets forming during condensation frosting can undergo spontaneous coalescence induced droplet jumping at micrometric length scales (~1 µm) prior to supercooling and freezing on the surface [23,99]. In addition to condensate removal prior to freezing, previous researchers have shown superhydrophobic surfaces to facilitate delayed freezing of individual droplets,

58

[116,117] as well as bulk water layers due to the delay in ice nucleation and higher thermal resistance at the liquid-solid interface [21,118].

The dominant mechanism of condensation frost formation on hydrophobic surfaces is inter-droplet frost wave propagation, [22,23,119-122] or ice bridging. When a subcooled condensate water droplet freezes on a hydrophobic or superhydrophobic surface, neighboring droplets still in the liquid phase immediately begin to evaporate [22,23]. The evaporated water molecules deposit on the frozen droplet and initiate the growth of ice bridges directed toward the droplets being depleted. The neighboring liquid droplets freeze as soon as the ice bridge connects and provides a heterogeneous nucleation site. Coalescence induced droplet jumping on superhydrophobic surfaces decreases the droplet distribution density, [5,55,123,124] thereby decreasing the frost wave propagation speeds, delaying frosting [23]. However, given enough time, frost formation still takes place due to the propagation of an inter-droplet frost wave from neighboring edge defects [23,125].

During inter-droplet ice bridging, two mechanisms govern the evaporation of neighboring water droplets: (1) the difference in saturation pressure of the water vapor surrounding the liquid droplet and the frozen droplet induces a vapor pressure gradient, [14,22,126] and (2) the latent heat released by freezing droplets locally heats the substrate, evaporating nearby droplets [23]. The relative significance of these two mechanisms is currently not well understood. A simple scaling analysis sheds some light on the mechanism. The latent heat of fusion of water at 0°C ($h_{sf} \approx 334$ kJ/kg) is approximately an order of magnitude smaller than the latent heat of vaporization at 0°C ($h_{fg} \approx 2500$ kJ/kg). Upon freezing, a microscale liquid water droplet releases the majority of its latent heat into the substrate, [127] which will hemispherically diffuse. Thus, we can estimate that

similarly sized neighboring water droplets will receive much less thermal energy than what is required for complete evaporation ($h_{sf} \ll h_{fg}$). However, if freezing water droplets have larger length scales ($R \sim$ mm), the latent heat of freezing might be significant enough to cause evaporation of smaller ($R \sim \mu$m) neighboring droplets. Thus, depending on the substrate thermal conductivity, the evaporation rate of neighboring water droplets due to conduction of latent heat into the substrate may be significant. Indeed, the substrate thermal conductivity dependent droplet evaporation phenomenon has been observed during the formation of frost halos, [128] indicating that the latent heat released may play an important role at a particular, and currently ill-defined, length scale.

In this chapter, we establish the length scale at which the latent heat released into the substrate is important via the study of individual water droplet freezing and bridge growth dynamics for varying droplet sizes ($10 < R < 100\ \mu$m), on aluminum and copper based hydrophilic ($\theta_a < 90°$), hydrophobic ($110° < \theta_a^{app} < 140°$), and superhydrophobic ($\theta_a^{app} > 160°$) surfaces. Using optical microscopy, we characterized the latent heat flux released into the substrate by measuring the freezing droplet radius and the respective droplet freezing time (t_f), defined as the time from initial ice nucleation within the droplet to complete droplet freezing. To calculate the latent heat flux transferred from the freezing droplet to neighboring droplets, we combined the experimentally characterized heat fluxes with 3D transient finite element method heat transfer simulations. The simulation results showed that the transfer of latent heat to neighboring droplets is indeed insignificant, and accounts for a negligible fraction of evaporation during microscale frost wave propagation. In order to further validate our simulations, we conducted additional experiments and simulations on substrates having varying thermal conductivity (1 to 400 W/m·K) to show that both individual droplet freezing times and adjacent droplet evaporation dynamics

remain invariant. Furthermore, we measured a negligible difference between inter-droplet bridging velocities for similar droplet arrangements on varying thermal conductivity substrates having identical wettability, pointing to vapor diffusion dynamics as the governing driving force for bridging. The experiments show that the wettability of the substrate has the largest effect on individual droplet freezing time, as the interfacial contact area between the droplet and the surface is inversely proportional to the advancing contact angle of the droplet, governing conduction heat transfer through the bulk of the droplet. Indeed, the disparity between measured individual droplet freezing time scales (~1 ms) to frost wave propagation time scales (~1 s) indicates that the observed bridging phenomena is not affected by individual droplet freezing. This study not only provides vital information on the role of latent heat released into the substrate during frost wave propagation but also explains the effect of substrate thermal conductivity and wettability during ice bridge formation.

4.3 Substrate Fabrication and Characterization

Six different types of superhydrophobic surfaces ($\theta_a > 150°$) and four hydrophobic surfaces ($110° < \theta_a^{app} < 140°$) were fabricated in order to study the effect of substrate thermal conductivity (k_s), structure length scale (l), and wettability on the latent heat released by individual droplets into the substrate. Table 1 shows a summary of the different substrate characteristics. Superhydrophobic copper (Cu – SHP) and superhydrophobic copper oxide (CuO – SHP) represent substrates with differing l and identical k_s. Superhydrophobic bronze (Bronze – SHP) and CuO-SHP represent substrates with differing k_s and similar l (Figure 4.1a and 4.1b). Superhydrophobic boehmite (AlO(OH) – SHP) and CuO – SHP represent substrates with both differing k_s and l. The wettability of the substrates was varied by using either micro/nanostructured (SHP), tool finished

(Cu – HP(I)) and polished (Cu – HP(II) and Si – HP) substrates functionalized with hydrophobic coatings.

To fabricate nanostructured superhydrophobic (SHP) AlO(OH) samples, commercially available Al 6061 tabs (25 mm x 25 mm x 0.8 mm, 99.90% purity) were first ultrasonically treated in acetone, followed by ethanol for 5 min each. After cleaning, the samples were dried in a clean N_2 stream. The samples were then immersed in hot deionized water (90˚C) for one hour, followed by removal and rinsing with room temperature deionized water. This enabled boehmite ($Al_2O_3.xH_2O$) formation on the Al surface with sharp, knife-like structures having length scales approaching ≈300 nm. To functionalize the surface, Heptadecafluorodecyltrimethoxy-silane (HTMS) was deposited using vapor phase deposition [102]. Nanostructured Al substrates were placed in a container with a vial of 1 mL HTMS toluene solution (5% v/v). A lid was placed on top to seal the container, followed by heating in an atmospheric pressure oven at 80˚C for 3 hours. This process allows for the development of a highly conformal coating as the HTMS molecules evaporate from solution and re-deposit on the aluminum samples. Contact angle measurements (MCA-3, Kyowa Interface Science Ltd.) of ≈300 nL droplets on an HTMS coated nanostructured Al surface showed advancing/receding contact angles of $\theta_a^{app}/\theta_r^{app} \approx 170.4 \pm 1.4° / 165.4 \pm 4.1°$.

To fabricate the nanostructured SHP Cu samples, commercially available polished multipurpose 110 Cu tabs (25 mm x 25 mm x 0.8 mm) were used (99.90% purity). Each Cu tab was ultrasonically treated in acetone, ethanol and then in isopropyl alcohol (IPA) for 5 min. An electroless galvanic deposition technique was used to coat textured layer of Ag on copper [103]. The cleaned copper tabs were immersed into an aqueous Silver Nitrate ($AgNO_3$, 0.010 mol/L) solution for 20 s, followed by rinsing with room temperature deionized water. The final surface

consisted of sharp, knife-like structures having length scales approaching ≈60 to 200 nm. To functionalize the surface, the textured Cu tabs were immersed in a solution of HDFT (3,3,4,4,5,5,6,6,7,7,8,8,9,9,10,10,10-heptadecafluoro-1-decanethiol) and Dichloromethane (CH_2Cl_2) (1 mol/L) for 5 min, followed by washing with Dichloromethane and drying in a clean N_2 stream. Contact angle measurements of ≈300 nL droplets on Ag/HDFT coated Cu surfaces showed advancing and receding contact angles of $\theta_a{}^{app}/\theta_r{}^{app} \approx 173.4 \pm 1.3° / 164.4 \pm 4.7°$.

To fabricate the structured SHP CuO and Bronze substrates, commercially available polished multipurpose Cu and Bronze tabs (25 mm x 2 25 mm x 0.8 mm) were used (99.90% purity). Each Cu and Bronze tab was thoroughly rinsed with acetone, ethanol, isopropyl alcohol (IPA) and deionized (DI) water. The tabs were then dipped into a 5.0 M hydrochloric acid solution for 2 min to remove the native oxide film on the surface, then rinsed with DI water and dried with clean N_2 gas. Nanostructured CuO films were formed by immersing the cleaned tabs into a hot (96 ± 3°C) alkaline solution composed of $NaClO_2$, $NaOH$, $Na_3PO_4 \cdot 12H_2O$, and DI water (3.75:5:10:100 wt. %).[129] During the oxidation process, a thin (≈300 nm) Cu_2O layer was formed on the dipped side that then re-oxidized to form sharp, knife-like CuO oxide structures with heights of $h \approx 1$ μm. To functionalize the surface, HTMS was deposited using chemical vapor deposition as explained in the fabrication procedure for AlO(OH) – SHP. Contact angle measurements of ≈300 nL droplets on an HTMS coated CuO surface showed advancing/receding contact angles of $\theta_a{}^{app}/\theta_r{}^{app} \approx 170.5 \pm 7.2° / 162.7 \pm 3.4°$. Contact angle measurements on an HTMS coated nanostructured Bronze surface showed advancing/receding contact angles of $\theta_a{}^{app}/\theta_r{}^{app} \approx 165.2 \pm 4.3° / 160.8 \pm 3.9°$.

To fabricate the HP Cu (I) and HP Cu (II) samples, commercially available tool finished (for Cu – HP (I)) and polished (for Cu – HP (II)) multipurpose 110 Cu tabs (25 mm x 25 mm x 0.8 mm) were used (99.90% purity). Then, it was thoroughly rinsed with acetone, ethanol, isopropyl alcohol (IPA) and deionized (DI) water. The tabs were then dipped into a 5.0 M hydrochloric acid solution for 2 min to remove the native oxide film on the surface, then rinsed with DI water and dried with clean N_2 gas. To functionalize the surface, HTMS was deposited using chemical vapor deposition as explained in the fabrication procedure for AlO(OH) – SHP. Contact angle measurements of ≈300 nL droplets on Cu – HP (I) surfaces showed advancing and receding contact angles of $\theta_a{}^{app}/\theta_r{}^{app} \approx 146.0 \pm 2.1°$ / $124.2 \pm 3.2°$ and on Cu – HP (II), $\theta_a{}^{app}/\theta_r{}^{app} \approx 118.9 \pm 1.7°$ / $74.2 \pm 0.9°$. The Cu – HP (I) samples are rough, and the water droplets residing on these samples are in Wenzel state.[1]

To fabricate the HP Si sample, commercially available Si wafers were used. The Si wafer was first thoroughly rinsed with acetone, ethanol, isopropyl alcohol (IPA) and deionized (DI) water and dried with clean N_2 gas. To functionalize the surface, HTMS was deposited using chemical vapor deposition as explained in the fabrication procedure for AlO(OH) – SHP. Contact angle measurements of ≈300 nL droplets on Si – HP surfaces showed advancing and receding contact angles of $\theta_a{}^{app}/\theta_r{}^{app} \approx 110.4 \pm 0.3°$ / $69.7 \pm 1.1°$.

To fabricate the SHP Cu-Glaco and Glass-Glaco samples, commercially available polished Cu tabs and Glass tabs (25 mm x 25 mm x 0.8 mm) were used. Then, they were thoroughly rinsed with acetone, ethanol, isopropyl alcohol (IPA), deionized (DI) water and dried with N_2 gas. The samples were then spray coated using the commercially available superhydrophobic coating, Glaco (Soft 99 Glaco Side Mirror Zero Coat - 40ml). The samples were then left to dry at room

temperature for 30 mins. Contact angle measurements of ≈300 nL droplets on Cu-Glaco – SHP surfaces showed advancing and receding contact angles of $\theta_a{}^{app}/\theta_r{}^{app} \approx 165.7 \pm 0.7°$ / $164.3 \pm 0.6°$ and on Glass_Glaco – SHP, $\theta_a{}^{app}/\theta_r{}^{app} \approx 163.5 \pm 1.9°$ / $161.3 \pm 0.9°$.

4.4 Experimental Methods

Individual droplet freezing was studied using a custom built top-view optical light microscopy set-up shown diagrammatically in a side view schematic in Figure 4.1(a). Briefly, samples were placed horizontally on the cold stage (Instec, TP104SC-mK2000A) with a thin film of water underneath in order to provide good thermal communication between the sample and stage. The cold stage was cooled to the test temperature of T_s = -20 ± 0.5°C in a laboratory environment having air temperature, T_{air} = 22 ± 0.5°C, and relative humidity (RH), Φ = 50 ± 1% (Roscid Technologies, RO120). Individual droplet freezing movies were recorded from the top view at 7,000 to 23,000 frames per second with a high speed camera (Phantom, V711, Vision Research) attached to an upright microscope (Eclipse LV100, Nikon). For a droplet of diameter D, the freezing time, t_f, was characterized as the time from initial ice nucleation within the droplet to complete droplet freezing. Top view imaging was performed with a 20X and 50X (TU Plan Fluor EPI, Nikon) objective. For the 20X, lens, the working distance was measured to be 5.8 ± 0.5 mm, and for 50X, 11.8 ± 0.5 mm. Illumination was supplied by an LED light source (SOLA SM II Light Engine, Lumencor). The LED light source was specifically chosen for its high-intensity and low power consumption (3.5 W) in order to minimize heat generation at the surface due to light absorption and minimize its influence on the droplet evaporation rates during condensation frosting. Furthermore, by manually reducing the condenser aperture diaphragm opening size and increasing the camera exposure time, we were able to minimize the amount of light energy needed for illumination and hence minimize local heating effects during freezing experiments [130].

Figure 4.2(a) shows the top view time-lapse optical microscopy images of individual droplet freezing on the nanostructured CuO surface (CuO – SHP). Visual inspection of the high-speed videos showing the freezing process clearly delineate the differing stages of freezing due to pixel intensity changes. For all the droplet freezing videos taken in this study, it was observed that the image intensity of ice was higher than that of water. In order to mimic the human eye and quantify when the freezing starts and stops, the intensity (average RGB value) of every frame in the droplet freezing video was plotted. Figure 4.2(b) shows the intensity of the optical microscopy images as a function of time as the water droplet transitions from liquid to solid. While calculating the intensity, a moving average was taken of five neighboring data points to minimize noise. Initially, when the droplet was in liquid phase, the intensity was constant. When an ice bridge approaches the liquid droplet and appears in the field of view (at $t = 1.8$ ms), the intensity of the image increases slightly, as observed at the local maxima near $t = 2.0$ ms. As soon as the ice bridge touches the liquid droplet, freezing initiates ($t = 2.0$ to 4.0 ms). The image intensity oscillates, and then becomes stable at a higher intensity. The oscillation represents the different stages of freezing: i) recalescence, defined as the formation of a porous ice scaffold inside the supercooled liquid droplet [116,131,132] (which starts at the onset of freezing, $t = 2.0$ ms and ends at $t = 2.4$ ms when the droplet is at 0°C), and ii) isothermal (at 0°C) freeze front propagation, which starts at $t = 2.4$ ms and ends at $t = 4.0$ ms. The initiation and end of freezing was identified by the change in intensity from the average value of 27.6 ± 0.1 (peak to peak) before freezing and 29.6 ± 0.1 after freezing due to change of phase from liquid to solid. Typical videos taken of the freezing process (21,000 FPS) resulted in ≈150 images from start to finish, ensuring enough granularity to capture the whole process.

Although the relation between the image intensity and phases of water (solid, liquid or mixed) is qualitative, small changes in intensity provide a clear and quantifiable window into freezing. The developed intensity-tracking method works particularly well for microscale droplets due to the significantly smaller radius when compared to the depth of field of the imaging optics. To verify our measurements, we performed additional experiments via focal plane shift imaging (FPSI) for focal planes located at the droplet base instead of the mid-plane. The FPSI results were invariant with a focal plane located within the droplet due to the significantly larger depth of field compared to the droplet length scale. To further verify the developed method, the total freezing time was also characterized by manual image processing of 30 randomly selected high-speed videos from the entire data set, showing the accuracy of our results to be within an error bound of ±5% when compared to image processing with the human eye.

4.5 Results and Discussions

4.5.1 Experiment Results

Figure 4.3(a) shows the individual droplet freezing time, t_f as a function of droplet diameter, $D = 2R$, for surface temperature $T_s = $ -20ºC. The individual droplet freezing time, t_f on superhydrophobic (SHP) surfaces was an order of magnitude greater than hydrophobic (HP) surfaces due to the higher characteristic length scales of droplets (volume/heat transfer area), and presence of air gaps beneath water droplets which act as thermal insulation to heat transfer. The four SHP surfaces having differing length scale nano/microstructures (60 nm to 1 µm) led to different air gap thickness and thermal resistance beneath the supercooled water droplets. Interestingly, for all droplet sizes (10 µm < R < 100 µm) analyzed on the varying length scale SHP surfaces, t_f showed the identical trend and magnitude, indicating that for the length scales examined here, the presence of air gaps beneath supercooled water droplets contributed negligibly

to delayed individual droplet freezing, consistent with previous studies on macroscale water films.[118] Note, for smaller droplet sizes, ($R < 10$ µm), thermal resistance offered by the air gaps becomes dominant than the thermal resistance of the droplet during freezing, wherein t_f might depend on the length scale of nano/microstructures (Figure 4.9).

4.5.2 Thermal Resistance Analysis

To help explain the underlying physics governing individual droplet freezing time, we examine the governing analytical heat transfer equations. When ice nucleation initiates in a water droplet, the temperature of the water droplet rises to 0°C due to recalescence (stage i in our results, Fig. 4.2) [128]. During recalescence, only a fraction of the liquid volume freezes into an ice scaffold while the latent heat of freezing is almost entirely absorbed by the resulting ice-water mixture, resulting in an increase of its temperature from the subcooled state (-20°C) to 0°C. When the ice-water droplet reaches 0°C, freeze front propagation ensues isothermally (at 0°C) within the droplet, converting the ice-water droplet to a homogenous ice droplet and rejecting the latent heat released into the substrate. The recalescence time was observed to be less than 20% of the total freezing time for the water droplets analyzed here. For scaling analysis, we assume that the recalescence time is $\approx 0.2 t_f$ and that the process is quasi-steady. Note, the $\approx 0.2 t_f$ recalescence time is a conservative estimate appropriate at smaller length scales ($R < 100$ µm). Prior experiments have shown the recalescence duration to be $< 0.2 t_f$ for larger droplets ($R > 1$ mm) [116]. Recalescence is a rapid, kinetically controlled process, wherein the fast temperature rise is due to the local nuclei growth, rather than heat transfer across the droplet [131-133]. The time taken for recalescence (~ 1 ms) is similar for all droplet sizes (10 µm $< R <$ 1 mm). For large droplets (R ~ 1 mm) with t_f ~ 10 s, the recalescence time is negligible as compared to t_f. Whereas, for the microscale droplets studied here (t_f ~ 10 ms), the recalescence approaches $0.2 t_f$. The latent heat

released during the recalescence freezing stage will be completely absorbed by the freezing droplet, to sensibly heat from -20°C to 0°C. Therefore, the total energy released into the substrate during freeze front propagation inside the droplet is equal to the heat transfer release rate, $\dot{q}_{tot}$, multiplied by the time taken for freeze front propagation inside the ice-water droplet during freezing, $0.8t_f$:

$$\dot{q}_{tot}(0.8t_f) = \rho_w V_{drop}(h_{sf} - c_P \Delta T_{sub}) \,, \tag{4.1}$$

where ρ_w and c_P are the density and specific heat of supercooled liquid water, respectively, V_{drop} is the droplet volume, and ΔT_{sub} is the temperature difference between the supercooled water droplet and 0°C.

To better understand the fundamental physics governing the rate of freezing, we developed an analytical thermal resistance model to analyze the rate-limiting steps for varying droplet morphologies. The thermal resistance analysis yields $\Delta T_{tot} = \psi_{tot} \dot{q}_{tot}$, where ΔT_{tot} is the temperature difference between the just-recalesced droplet (0°C) and far-field substrate temperature, and ψ_{tot} is the total thermal resistance, defined as the summation of the substrate spreading, ψ_{subs}, air gap, ψ_{gap}, and droplet conduction, ψ_{drop} thermal resistances.

Figure 4.8 shows the thermal resistance network for a droplet freezing on a cold superhydrophobic nanostructured surface. For a droplet with radius R residing on a surface with temperature T_s, the conduction thermal resistance offered by the substrate (assuming thermal resistance by a semi-infinite body) is: [134]

$$\psi_{\text{cond}} = \frac{1}{4k_s R \sin\theta},$$ (4.2)

where k_s is the thermal conductivity of the substrate, θ is the contact angle of the droplet. The thermal resistance of air gap beneath the water droplet is given by: [59]

$$\psi_{\text{gap}} = \frac{1}{k_{\text{HC}}\pi R^2 \sin^2\theta}\left[\frac{k_P\phi}{\delta_{\text{HC}}k_P + hk_{\text{HC}}} + \frac{k_w(1-\phi)}{\delta_{\text{HC}}k_w + hk_{\text{HC}}}\right]^{-1},$$ (4.3)

where k_{air} is the thermal conductivity of air, k_P is pillar thermal conductivity, h is the height of pillars, δ_{HC} is the coating thickness, ϕ is the structured surface solid fraction, k_w is thermal conductivity of water, and k_{HC} is the coating thermal conductivity. Thermal resistance offered by the droplet while freezing can be calculated from the solution to Stefan's problem. Assuming that the liquid phase is at the melting temperature of ice, and that the heat capacity of ice is negligible compared to the latent heat of solidification, an energy balance on the propagation of a planar ice-water front during freezing results in: [104,105]

$$vh_{\text{fs}} = \rho_{\text{ice}}k_{\text{ice}}\frac{\partial T}{\partial z},$$ (4.4)

where v is the ice front propagation speed, h_{fs} is the latent heat of fusion (per unit volume), k_{ice} and ρ_{ice} are the thermal conductivity and density of ice, and $\partial T/\partial z$ is the temperature gradient in the direction of ice propagation. Integrating Eq. (4.4) from ice nucleation to complete icing, we see that the total freezing time is proportional to the square of characteristic length, L_c (equal to height of the liquid droplet in this case, $L_c = R(1 + \cos\theta)$) is given by:

$$t_f = \frac{h_{fs}L_c{}^2}{2k_{ice}\overline{\Delta T}}, \tag{4.5}$$

where , $\overline{\Delta T}$ is the average temperature difference between the melting temperature (0°C) and the temperature at the base of water column ($\overline{\Delta T} = T_{melting} - T_{base}$).

For scaling, assuming that the recalescence time is negligible as compared to the total freezing time, the energy released into the substrate will be equal to the rate of heat released into the substrate by the ice-water droplet during freezing, $\dot{q}_{tot}$, multiplied by the total freezing time, t_f. By energy conservation, the energy released into the substrate will be equal to the latent energy released by the ice-water droplet while freezing:

$$\dot{q}_{tot}t_f = \rho_w V_{drop}h_{sf}, \tag{4.6}$$

where V_{drop} is the droplet volume. Thermal resistance analysis yields $\Delta T = \psi q$, Equation 4.6 then can be rearranged as:

$$t_f = \frac{\rho_w V_{drop}h_{sf}}{\Delta T_{tot}}\psi. \tag{4.7}$$

Comparing Eq. (4.5) and (4.7), we get:

$$\psi_{droplet} = \frac{3}{8\pi k_{ice}R(1 - \cos\theta)}. \tag{4.8}$$

Individual thermal resistances (ψ_{cond}, ψ_{gap}, and ψ_{drop}) are plotted as a function of droplet radius in Figure 4.9. Figure 4.9 corresponds to an aluminum substrate (thermal conductivity, $k_{\text{s}} = 205$ W/mK) with AlO(OH) nanostructures (height, $h = 100$ nm) and a monolayer coating of thickness (coating thickness, $\delta_{\text{HC}} = 3$ nm and coating thermal conductivity, $k_{\text{HC}} = 0.2$ W/mK). The droplet thermal resistance is dominant for droplet radius $R > 15$ μm. The total thermal resistance is thus, $\psi_{\text{tot}} = \psi_{\text{cond}} + \psi_{\text{gap}} + \psi_{\text{drop}} + \psi_{\text{conv}}$.

For all superhydrophobic substrates tested here, ψ_{gap} dominated at smaller droplet length scales ($R < 15$ µm), while the spreading resistance (ψ_{subs}) was negligible at all length scales, indicating that the freezing kinetics were governed mainly by heat conduction through the water/ice droplet. Normalizing the experimentally measured freezing time by the length scale dependent parameters in our thermal resistance analysis (V_{drop} and ψ_{tot}), results in a surface wettability and droplet length scale independent freezing parameter (t_{fr}):

$$t_{\text{fr}} = \frac{0.8 t_{\text{f}}}{V_{\text{drop}} \psi_{\text{tot}}} = \frac{\rho_{\text{w}}(h_{\text{sf}} - C_{\text{P}} \Delta T_{\text{sub}})}{\Delta T_{\text{tot}}}. \tag{4.9}$$

Figure 4.3(b) shows t_{fr} as a function of D for all experimentally measured data points, showing that all data from Figure 4.3(a) collapse to the same order of magnitude. The collapse of the data indicates that for the substrates and droplet sizes (10 µm $< R < 100$ µm) studied here, the contact angle and droplet length scale dependent heat conduction within the droplet governs the individual droplet freezing time. It is important to note, the frost wave propagation timescale (~1s) observed on the superhydrophobic surfaces was much slower than the individual droplet freezing timescale (~ 10ms). Thus, frost wave propagation via ice bridge growth dominates surface

condensation frosting dynamics, and delay in individual microscale droplet freezing time has a negligible direct effect on frosting time on non-wetting surfaces. However, individual droplet freezing may have an indirect effect on droplet ice bridging via the conduction of latent heat through the substrate to neighboring evaporating droplets that help grow the liquid bridge.

4.5.3 Numerical Model to Calculate Latent Heat Transferred to Neighboring Droplet

To elucidate the effect of latent heat released into the substrate by freezing of supercooled droplets, we calculated the latent heat transferred to neighboring droplets by performing transient numerical simulations. A 3D numerical model based on finite element method (ANSYS) was used to solve the heat transfer from the freezing droplet to a neighboring water droplet via the chilled substrate. The substrate was modeled (Figure 4.4) with a constant temperature boundary condition at the left, bottom and right surface. Utilization of insulated boundary conditions negligibly affected the results ($< 4\%$) due to the large domain size δ (discussed later). An insulated boundary condition was used at the top surface excluding the areas where heat flux is input and output (base areas of freezing and neighboring water droplets respectively). Using a convective boundary condition at the top surface instead of insulated resulted in $< 1.5\%$ change in the heat transfer results, at the price of significant convergence time increases. Thus, the insulated boundary condition was used at the top surface where droplets were not present. The heat flux input, q''_{lat} into the substrate at the base of freezing droplet was calculated by:

$$q''_{\text{lat}} = \frac{\rho_{\text{w}} V_{\text{drop}} h_{\text{fs}}}{\pi R^2 \sin^2 \theta \ t_{\text{f}}}, \tag{4.10}$$

where ρ_{w} is the water density, V_{drop} is the droplet volume, and θ is droplet apparent contact angle.

73

During the isothermal freeze front propagation inside a water droplet on substrates with very low thermal conductivity (< 1 W/m·K), the latent heat released by the freezing droplet can lead to significant evaporation of the remaining liquid in the freezing droplet, resulting in a smaller heat flux being released into the substrate. Here, we calculate the percentage of latent heat lost via evaporation of the mother droplet and the remaining percentage of latent heat released into the substrate.

Based on the individual droplet freezing times (t_f), we calculate the thermal penetration depth, δ for a given substrate ($\delta = \sqrt{\alpha_s t_f}$, where α_s is the thermal diffusivity of the substrate). As a conservative estimate, we define the volume of the substrate exchanging heat with the freezing droplet, [127]

$$V_{ex} = \pi(\delta + R_b)^2 \delta, \qquad \qquad \text{(if } \delta > 2R_b\text{)} \qquad (4.11)$$

$$V_{ex} = \pi(\delta + R_b)^2 R_b, \qquad \qquad \text{(if } \delta < 2R_b\text{)} \qquad (4.12)$$

where R_b is the base radius of the freezing droplet. We have considered a cylindrical volume in the substrate which will exchange heat with the freezing droplet rather than a hemispherical volume due to the conservative (maximum volume) estimate provided by the cylindrical geometry. The maximum increase in the temperature of the substrate during droplet freezing will be, $\Delta T = T_{melting} - T_s = 20°\text{C}$, assuming that the latent heat released into the substrate will heat up the substrate to the equilibrium temperature of the droplet during freezing, $T_{melting} = 0°\text{C}$. The maximum amount of energy absorbed by the substrate, assuming that the energy absorbed will increase the temperature of the volume V_{ex} underneath the freezing droplet by ΔT is,

74

$$Q_s = \rho_s V_{ex} c_P \Delta T \, , \tag{4.13}$$

where ρ_s and c_P are substrate density and specific heat respectively. The latent heat released by the freezing water droplet is:

$$Q_{lat} = \rho_w V_{drop} h_{fs}, \tag{4.14}$$

where V_{drop} is the volume of freezing droplet. If the latent heat released by the freezing droplet, $Q_{lat} < Q_s$, it is assumed that all the latent heat is released into the substrate. If $Q_{lat} > Q_s$, it is assumed that the freezing droplet releases latent heat equivalent to Q_s into the substrate and the remaining latent heat, $Q_{lat} - Q_s$, leads to the evaporation of the remaining liquid in the mother droplet.

It was observed that for substrates with very low thermal conductivity (< 1 W/m·K, formation of Frost Halos on PMMA), more than 50% of the latent heat released during freezing leads to evaporation of the mother droplet and the remaining latent heat is released into the substrate ($Q_s < 0.5 Q_{lat}$). For substrates with higher thermal conductivity (> 10 W/m·K), it was observed that that no latent heat is lost via evaporation of the freezing droplet, and all latent heat is released into the substrate ($Q_{lat} < Q_s$). Based on this criteria, the input heat flux in Fig. 4.5, q''_{lat} is defined as:

$$q''_{lat} = \frac{Q_{lat}}{\pi R_b^2 t_f}, \qquad \text{(if } Q_{lat} < Q_s) \tag{4.15}$$

$$q''_\text{lat} = \frac{Q_\text{s}}{\pi R_\text{b}^2 t_\text{f}}, \qquad\qquad (\text{if } Q_\text{lat} > Q_\text{s}) \qquad (4.16)$$

It is important to note, the above analysis assumes from the start that local evaporation of droplets due to heat conduction into the substrate is negligible. This arises due to the assumption that all of the latent heat released from the freezing mother droplets is transferred into sensible heating of the substrate beneath. In actuality, a portion of the conducted latent heat may be utilized to evaporate nearby droplets and result in $Q_\text{lat} < Q_\text{s}$. However, this assumption can be inferred to be incorrect due to the already shown minimal contribution of latent heat for local droplet evaporation at higher substrate thermal conductivities. For substrates with very low thermal conductivity (< 1 W/m·K), the latent heat released by the freezing droplet can lead to significant evaporation of the remaining liquid in the freezing droplet, resulting in a smaller heat flux being released into the substrate.

A convective heat transfer boundary condition is used at the base of the neighboring water droplet with an overall heat transfer coefficient, h_b, representing the conduction thermal resistance through the droplet (~ 20,000 W/m²K, Fig. 4.4a). The neighboring water droplet was assumed to be supercooled at the substrate temperature, $T_\text{neigh,drop} = T_\text{s} = -20°$C. To verify the sensitivity of this assumption, additional simulations were conducted to show that a change in neighboring droplet temperature to $T_\text{neigh,drop} = -10°$C resulted in <10% change in the heat transfer results, thus the neighboring droplet temperature was fixed at -20°C for all the simulations. The output of the simulation was the heat flux received by the neighboring water droplet, q''_iw. The distance between the freezing droplet and a neighboring droplet, x was varied along with the substrate thermal conductivity, k_s.

ANSYS Fluent was used model the substrate, with hexahedral meshing as shown in Figure 4.4(b) with $\approx$ 2 million cells. Mesh refinement was used at the droplet-substrate interface with minimum element size = 100 nm. A grid refinement study via a further reduction in mesh size resulted in < 1% change in the heat transfer results. The size of the domain was taken to be 0.5 mm x 0.5 mm x 1 mm (δ = 0.5 mm, Fig. 4.4b). Further increment in δ resulted in < 1% change in the heat transfer results. The domain was chosen based on the calculation of the thermal penetration depth of the released latent heat, estimated as $\delta \sim \sqrt{\alpha_s t_f}$. For the individual droplet freezing times considered here ($\approx$10 ms) and thermal diffusivity of aluminum ($\alpha_{Al} \approx 9.7 \times 10^{-5}$ m^2/s), we calculated a thermal penetration distance of $\delta \approx 1$ mm. During the simulations of droplet freezing at larger length scales ($R \sim 1$ mm), a larger domain size was chosen accordingly. Among the substrates used, Copper had the highest thermal penetration depth, $\delta \approx 20$ mm ($\alpha_{Cu} \approx 1.1 \times 10^{-4}$ m^2/s, and t_f = 3.1 s), resulting in a 20 mm x 20 mm x 50 mm domain size for the simulations. Further increment in domain size resulted in < 1% change in the heat transfer results. To allow for the latent heat pulse to diffuse, we run the transient simulations for time scales 5X greater than t_f.

Figure 4.5 shows the heat flux (q''_{iw}) transferred from a freezing droplet to a neighboring droplet as a function of center-to-center distance, x (left axis). To determine the magnitude of the latent heat received at a distance x from the freezing droplet, we calculated R_{evap} as a function of x (right axis), where R_{evap} is the radius of the water droplet which would evaporate completely due to the added latent heat flux, q''_{iw} for the duration of freezing time $0.8t_f$. For the droplet size scales examined here ($R < 120$ µm), $R_{evap} < 0.1$ nm, which is smaller than the condensation nucleation radius of water at STP (~ 10 nm) [57]. Thus, for the droplet length scales and wettabilities tested here ($R < 120$ µm), the transfer of latent heat to neighboring droplets was

insignificant, and account for a negligible fraction of neighboring droplet evaporation during frost wave propagation.

Our simulations and analytical model both reveal that the transfer of latent heat to neighboring droplets varies with substrate thermal conductivity. However, due to the high degree of heat spreading through the substrate, the fraction of evaporation of neighboring water droplets due to heat conduction through the substrate remains negligible for all thermal conductivities simulated ($0.1 < k_s < 400$ W/m·K). Thus, our simulations results predict that the velocity of the ice bridge growth should be invariant with substrate thermal conductivity, in good agreement with a previous study which modeled the growth velocity of an ice bridge independent of latent heat considerations [126].

4.5.4 Experiments to Measure Ice Bridge Growth Velocity

To experimentally verify our model and simulations, we conducted additional frosting experiments on glass ($k_s = 1$ W/m·K) and copper ($k_s = 401$ W/m·K) substrates spray-coated with a thin layer (< 100 nm) [135] of a superhydrophobic commercial coating. The optical microscopy setup (Fig. 4.1a) was used to record top view videos at 100 FPS of inter droplet ice bridge formation during frost wave propagation. Figure 4.6 shows the ice bridge average growth velocity, v_{ib} as a function of ice bridge length l_{ib}, defined as the distance between the freezing droplet and neighboring droplet for superhydrophobic glass and copper substrates. The temperature of the substrate was maintained at, T_s = -20°C and the temperature of the ambient was maintained at, T_a = 22.3 ± 0.5°C with a relative humidity of, Φ = 49.2 ± 1%. The velocity of the ice bridge was determined to be on the same order of magnitude ($\approx$1-4 µm/s) for both low and high thermal conductivity substrates, in line with our model and simulations. In agreement with previous

78

studies, [126] we observed that v_{ib} for the microscale droplets studied here was proportional to the rate of evaporation of the neighboring water droplet which is governed solely by vapor pressure gradients.

4.5.5 Droplet Freezing at Millimetric Length Scale

Contrary to our microscale frost wave propagation results, at larger droplet length scales ($R \sim 1$ mm) the latent heat transfer into the substrate may play a significant role in the evaporation of neighboring microscale water droplets. Previous studies of millimetric droplet frost halo formation showed that during the recalescence stage, if the supersaturated pressure required for heterogeneous nucleation of condensate on the substrate, p_{n}, is less than that of the pressure at the interface of the freezing ice-water droplet, $p_{\text{i},0}$, water molecules will diffuse from the liquid-vapor interface of the large freezing droplet to the ambient surroundings [128]. These water vapor molecules re-condense as microdroplets in the form of an annular ring surrounding the frozen droplet that can rapidly freeze, forming a frost halo. The survival and extent of the frost halo formation has been shown to depend on the duration of the transient pressure condition ($p_{\text{i},0} > p_{\text{n}}$), which is governed by the time taken after recalescence, τ_{f} to complete freeze front propagation [128]. With an increase in the substrate thermal conductivity k_{s}, τ_{f} decreases [128].

To probe the effect of latent heat released into the substrate by freezing droplets at larger length scales, we calculated the latent heat transferred to neighboring droplets, q''_{iw} by performing additional 3D transient numerical simulations. As previously mentioned, for substrates having low thermal conductivity (< 1 W/m·K), the latent heat released by the freezing droplet can lead to significant evaporation of the remaining liquid in the freezing (mother) droplet, resulting in a smaller heat flux released into the substrate [128]. We used analytical calculations to estimate the

fraction of latent heat lost via evaporation of the mother droplet and the remaining latent heat released into the substrate (Eq. 4.15 and 4.16) [127]. For substrates having very low thermal conductivity (< 1 W/m·K), more than 50% of the latent heat released during freezing goes to evaporating the mother droplet while the remaining heat is released into the substrate. For substrates with higher thermal conductivity (> 10 W/m·K), a negligible amount of heat is lost via evaporation of the mother droplet, hence all latent heat is released into the substrate.[127] For the simulations conducted herein, the percentage of latent heat released into the substrate was a conservative (theoretically maximum) estimate. The experimental data of individual droplet freezing times for larger droplet length scales ($R = 1.1$ mm) on substrates with varying thermal conductivity was obtained from a previous study, [128] and utilized in the transient numerical simulations via the application of an appropriate conductivity-dependent heat flux during droplet freezing.

Figure 4.7 shows the heat flux, q''_{iw} (left axis), and computed evaporation radius, R_{evap} (right axis), as a function of substrate thermal conductivity, k_s, for freezing droplets having $R =$ 12.2 µm and $R = 1.1$ mm neglecting frost halo microdroplet condensation effects. The distance between the edge of the base circle of the freezing droplet and the center of neighboring evaporating droplet, $x_e = 8$ µm was fixed. For $R = 1.1$ mm, $R_{evap} \sim 1$ µm, indicating that millimeter sized freezing water droplets have the capability of evaporating micron sized neighboring water droplets. The neighboring water droplets can be pre-existing neighboring supercooled condensate, or the small droplets that consist of the halo itself. As k_s decreases (401 to 0.19 W/m·K) the transferred heat flux from the freezing droplet to a neighboring water droplet increases due to the larger semi-infinite body resistance, $\psi_{subs} = 1/(4k_s R_b)$, where R_b is the droplet base radius, resulting in greater spatially confined heat flow to adjacent droplets. However, as previously

discussed, for sufficiently thermally insulating surfaces more than 50% of the droplet latent heat content can be lost via evaporation as opposed to substrate conduction. On thermally insulating surfaces assuming no frost halo microdroplet condensation effects, two competing effects are established: (1) the reduction of latent heat transferred to the substrate that acts to lower adjacent microdroplet evaporation, and (2) the localization of latent heat transferred from the freezing droplet to the neighboring droplets which act to increase adjacent microdroplet evaporation. For these simulations conducted here (Figure 4.7), the effect of heat localization dominated resulting in larger R_{evap} with lower k_s. To understand this counter intuitive result which opposes previous experiments, [128] we need to examine the main invalid assumption made during our simulations: neglecting frost halo mediated microdroplet condensation. The third and dominant factor affecting neighboring microscale droplet formation or evaporation is the pressure gradient ($p_{i,0} > p_n$), and how long it persists, resulting in diffusion of water vapor from the freezing ice-water droplet to the surrounding substrate. The discrepancy between our computational results and experiments clearly indicate that latent heat transfer to neighboring droplets via conduction through the substrate is not a dominating factor driving frost halo formation with large scale (~ 1mm) droplets. Instead, vapor pressure gradients constitute the main driving force for bridge formation and local droplet evaporation. Indeed, previous results have shown frost halo condensed microdroplets to be $R \approx 10~\mu\text{m} \gg R_{\text{evap}}$, [128] clearly pointing to vapor diffusion effects dominating droplet freezing dynamics across length scales.

The experimental and numerical results presented here clearly show that latent heat transfer through the substrate during frost formation has a negligible effect on condensation frosting dynamics on non-wetting substrates. While individual droplet freezing dynamics are governed by liquid/solid heat conduction within the droplet, bridge growth and frost halo formation across

length scales are governed by vapor diffusion dynamics. In the future, coupling 3D numerical simulations of vapor diffusion dynamics with heat conduction within the supercooled freezing droplet will be key to fully capturing the underlying physics of frost formation on arbitrary surfaces. Furthermore, the development of multi-droplet simulations in the frozen and supercooled state will be important to better represent the physical phenomena where droplet-droplet coupling has the potential to significantly alter the temperature fields inside the substrate and resulting frost wave propagation dynamics. In addition, future studies should examine the important effect of relative humidity on ice bridge formation. Although key for a variety of phase change processes, we do not expect the key message to change based on relative humidity due to the minute contribution of latent heat on adjacent droplet evaporation.

4.6 Conclusions

In conclusion, we have demonstrated that latent heat released into the substrate during freezing of individual droplets does not affect frost wave propagation or frost halo formation. Furthermore, we showed that the ice bridge velocities are independent of the substrate thermal conductivity. Ice bridge formation during frost wave propagation is governed solely by the vapor pressure gradient caused by the difference in saturation pressure of the water vapor surrounding the liquid droplet and the frozen droplet. We showed that at length scales tested here, the individual droplet freezing time depends on the substrate wettability, since it governs the droplet thermal resistance (which is the most dominant thermal resistance), increasing with higher intrinsic and apparent advancing contact angles. By characterizing the individual droplet freezing (~1ms) and frost wave propagation (~1s) timescales, we show that delay in individual droplet freezing (due to wettability effects) does not affect the overall frosting speed due to the disparate timescales of the two processes. This study not only elucidates the role of latent heat released into the substrate

82

during frost wave propagation but also explains the effect of substrate thermal conductivity and wettability during ice bridge formation and individual droplet freezing.
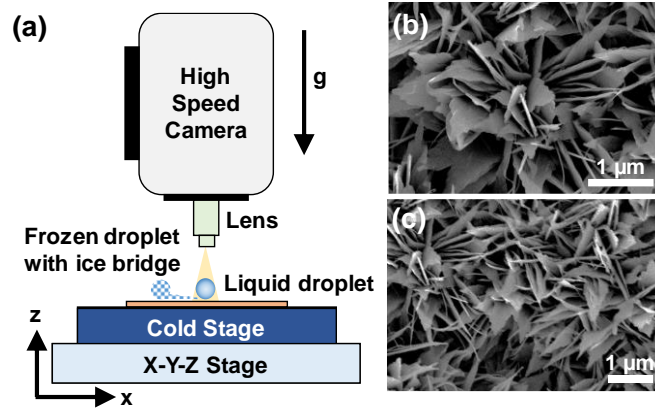
4.7 Figures

Figure 4.1. (a) Side view schematic of the freezing experiment (not to scale). Scanning electron micrograph of a (b) 10 min oxidized nanostructured CuO surface coated with a ≈ 3 nm thick layer of HTMS and (c) 10 min oxidized nanostructured Bronze surface coated with a ≈ 3 nm thick layer of HTMS. The length scale of structures on Cu and Bronze substrates are same with different substrate thermal conductivity ($k_{Cu} = 401$ W/m·K, $k_{Bronze} = 110$ W/m·K). The sharp, knife-like CuO structures have characteristic heights, $h \approx 1$ μm, and solid fraction, $\varphi \approx 0.04$. The cold stage was kept at a temperature $T_s = -20 \pm 0.5°C$. Movies were recorded at 7000 to 23000 frames per second. Experimental conditions: ambient air temperature $T_{air} = 22 \pm 0.5°C$, vapor temperature $T_v = T_{sat}(\varPhi P_{sat}(T_{air})) = 11.1 \pm 0.5°C$, relative humidity $\varPhi = 50 \pm 1\%$.
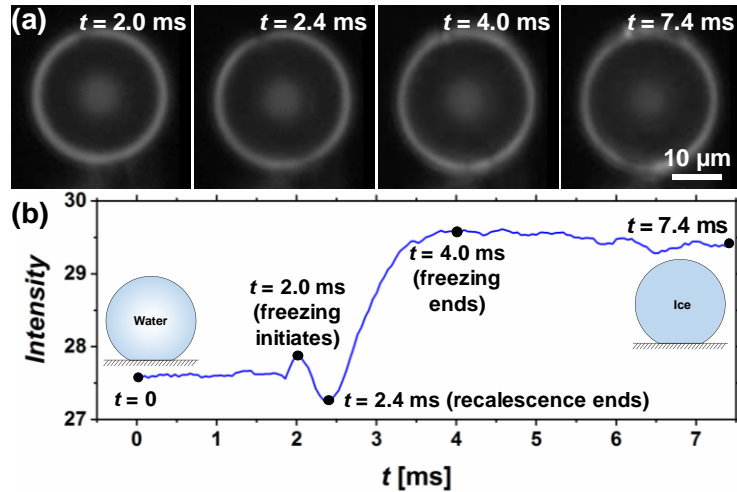
Figure 4.2. (a) Time-lapse optical microscopy images of individual droplet freezing on a nanostructured CuO – SHP surface ($\theta_a^{app} \approx 170.5 \pm 7.2°$). (b) Intensity (average RGB value) of the optical microscopy images as a function of time as the water droplet transitions from liquid to solid. At the beginning of the video at $t = 0$, the droplet is still in liquid state. Freezing initiates at $t = 2.0$ ms and it ends at $t = 4.0$ ms. The initiation and end of freezing was identified by the increase in intensity from the average value of 27.63 ± 0.04 (peak to peak) before freezing and 29.59 ± 0.05 after freezing.
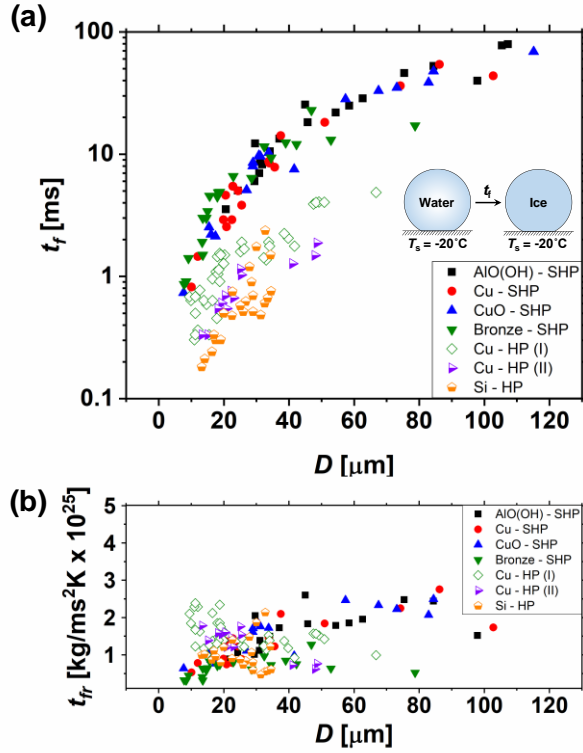
Figure 4.3. (a) Individual droplet freezing time, t_f and (b) reduced freezing parameter, t_{fr} as a function of droplet diameter, D for surface temperature T_s = -20ºC. For the hydrophobic samples (Cu – HP (I), Cu – HP (II), and Si – HP), frost wave propagated on the whole surface before the droplets could grow greater than 60 μm in diameter. Thus, there is no data for $D > 60$ μm for hydrophobic samples. The individual droplet freezing time, t_f for superhydrophobic (SHP) surfaces is an order of magnitude greater than hydrophobic (HP) surfaces due to the higher characteristic length scales (volume/heat transfer area) for $D > 30$ μm, and presence of air gaps beneath water droplets which act as thermal insulation to heat transfer for $D < 30$ μm. To normalize the results, the freezing time is divided by the droplet volume and the total thermal resistance, $t_{fr} = t_f/(V_{drop}\psi_{tot})$, resulting in a constant reduced freezing parameter ss a function of droplet diameter, D. Error bars are not included for clarity (maximum error in freezing time and diameter $\approx \pm 5\%$ of the measured value).
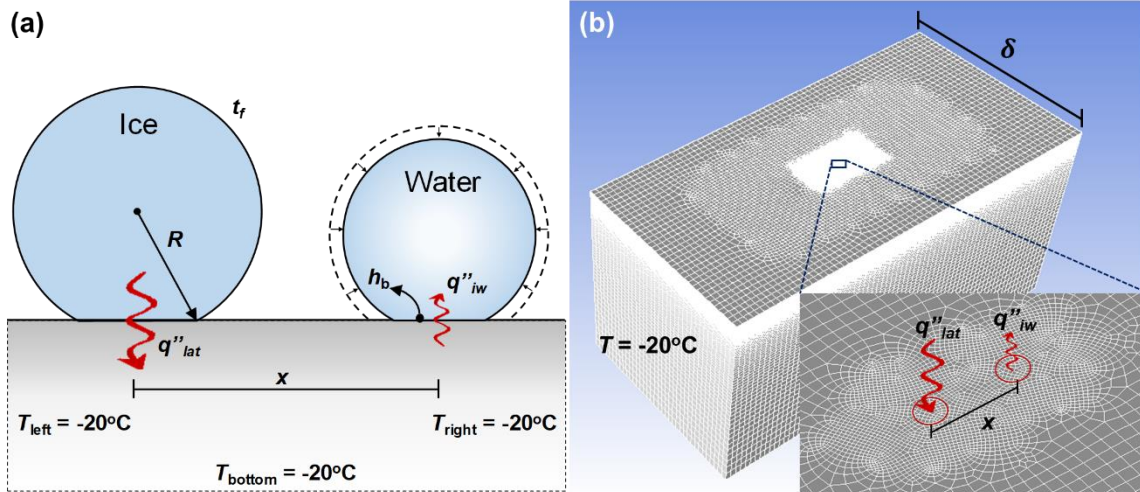
Figure 4.4. (a) Schematic of the simulation domain. (b) The hexahedral meshing of the domain (substrate) used in ANSYS Fluent. Inset: Zoomed-in view of the input and output boundary conditions. The domain was chosen based on the calculation of the thermal penetration depth of the released latent heat, estimated as $\delta \sim \sqrt{\alpha_s t_f}$. The total number of mesh elements exceeded 2 million with a minimum mesh refinement length scale of 100 nm at the locations immediately beneath the droplets.
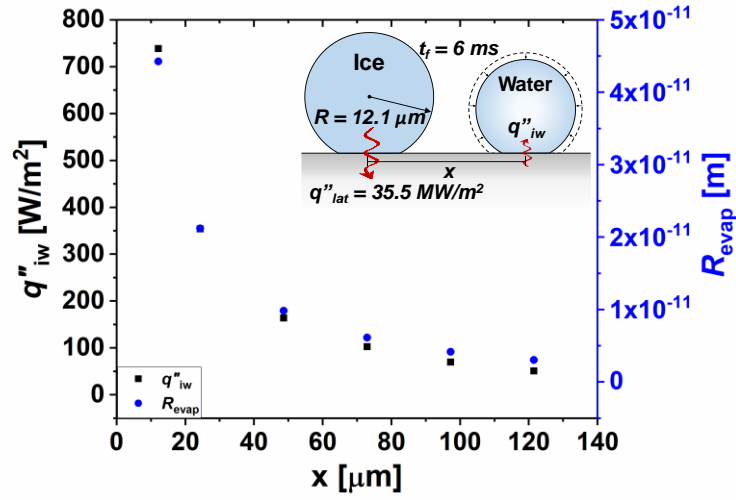
Figure 4.5. Heat flux (q''_{iw}) transferred from a freezing droplet to a neighboring droplet as a function of center-to-center distance, x, between the two droplets (left axis). Inset: Schematic of the simulation. The simulations are done for aluminum substrate ($k_{Al} = 205$ W/m·K). To determine the magnitude of the latent heat received at a distance x from the freezing droplet, we calculated R_{evap} as a function of x (right axis), where R_{evap} is the radius of water droplet which will evaporate completely due to the added latent heat flux, q''_{iw} available at the distance x for the duration of freezing time t_f. For the droplet size scales examined here ($R < 120$ µm), $R_{evap} < 0.1$ nm, smaller than the condensation nucleation radius of water at STP (~ 10 nm).
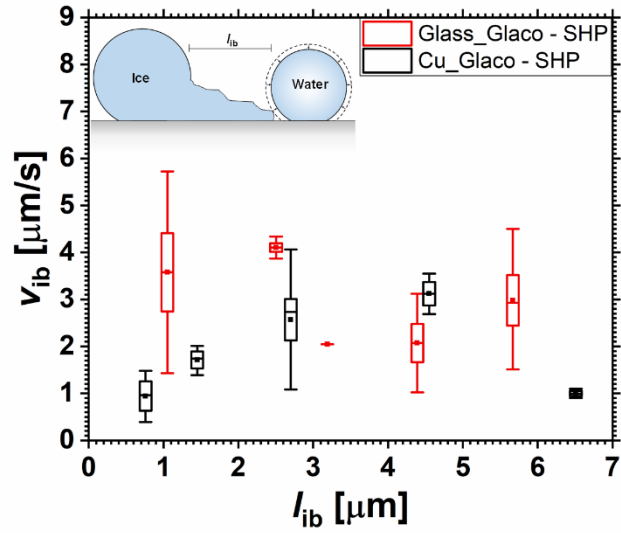
Figure 4.6. Ice bridge velocity, v_{ib} as a function of ice bridge length, l_{ib}, defined as the distance between the freezing and neighboring droplets (inset schematic), for glass and copper substrates spray-coated with Glaco commercial coatings. The ice bridge velocity, v_{ib} is the cumulative rate at which an ice bridge forms between two droplets spaced by the distance l_{ib}. The temperature of the substrate was, $T_s = -20°C$ and the temperature of the ambient was maintained at, $T_a = 22.3 \pm 0.5°C$ with a relative humidity of, $\phi = 49.2 \pm 1\%$. Boxes represent the standard deviation, square dots represents the mean, horizontal lines within the box represents the median, and the whiskers represent the minimum and maximum of the experimental data. The velocity of ice bridge was on the same order of magnitude for copper ($k_s = 401$ W/m·K) and glass ($k_s = 1$ W/m·K) substrates.
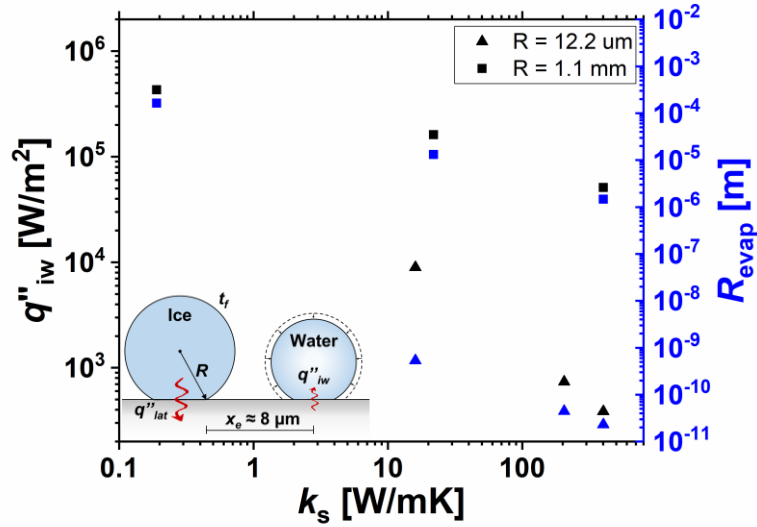
Figure 4.7. Heat flux, q''_{iw} (left axis) and evaporation radius, R_{evap} (right axis) as a function of substrate thermal conductivity, k_s for freezing droplet having $R = 12.2$ µm and $R = 1.1$ mm. The distance between the edge of the base circle of the freezing droplet and the center of neighboring evaporating droplet, $x_e = 8$ µm is fixed. Inset: Schematic of the simulation. As k_s decreases ($k_{Cu} = 401$ W/m·K, $k_{Al} = 205$ W/m·K, $k_{Ti} = 21.9$ W/m·K, $k_{Steel} = 16$ W/m·K, $k_{PMMA} = 0.19$ W/m·K) the transferred heat flux from the freezing droplet to a neighboring water droplet increases due to the larger semi-infinite body resistance $\psi_{t,s} = 1/4k_s R_b$. The experimental data of individual droplet freezing times at higher length scales ($R = 1.1$ mm) on substrates with varying thermal conductivity was obtained from literature [128]. Note, the results presented are incorrect and opposite trends compared to prior experimental results due to the omission of vapor diffusion effects in the simulation.
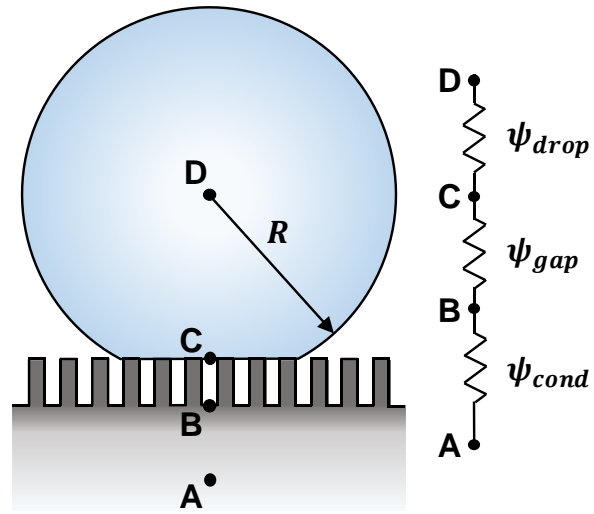
Figure 4.8. Thermal resistance network for a droplet freezing on a cold superhydrophobic nanostructured surface.
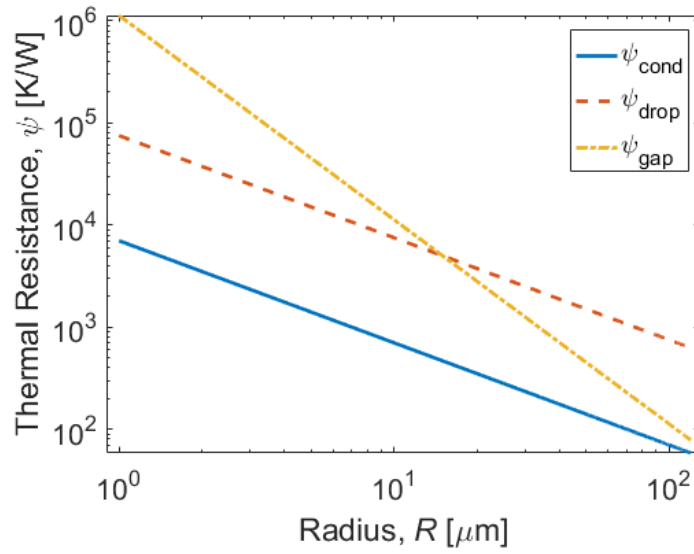
Figure 4.9. Individual thermal resistances (ψ_{cond}, ψ_{gap}, and ψ_{drop} are as a function of droplet radius. An aluminum substrate (thermal conductivity, k_s = 205 W/mK) with AlO(OH) nanostructures (height, h = 100 nm) and a monolayer coating of thickness (coating thickness, δ_{HC} = 3 nm and coating thermal conductivity, k_{HC} = 0.2 W/mK) is considered.

CHAPTER 5: DYNAMIC DEFROSTING ON SUPERHYDROPHOBIC AND BIPHILIC SURFACES

5.1 Overview

Ice formation and accretion present serious concerns for many building energy applications. In the heating, ventilation, air-conditioning, and refrigeration sectors, the most common approach to remove frost from a surface (defrost) is to reverse the system cycle direction and heat the working fluid. However, water retention on the heat exchanger surface during defrosting decreases the long term heat transfer performance. Here, we study the defrosting behavior of superhydrophobic and biphilic surfaces comprising of spatially distinct superhydrophobic ($\theta_a \rightarrow 180°$) and hydrophilic ($\theta_a = 78°$) domains. Using top and side view optical imaging, we show that superhydrophobic regions undergo dynamic defrosting, where the frozen ice/frost layer undergoes spontaneous motion via the formation of a highly mobile slush. We experimentally show that the high mobility of dynamic defrosting enables the use of surface forces to 'pull' and remove the slush from the surface prior to it completely melting, even in the absence of forces such as gravity or shear. To explore the effect of pattern heterogeneity, we studied various biphilic patterns inspired from nature such as the banana leaf. We optimized the design space with respect to minimizing water retention during defrosting. Our work not only provides the fundamental understanding required for the design of heterogeneous defrosting coatings, but also elucidates the role of wettability gradients on defrosting dynamics for a plethora of energy applications.

5.2 Introduction

Ice accretion and frost formation on solid surfaces is a crucial phenomenon to industrial applications, such as heating, ventilation, air-conditioning, and refrigeration (HVAC&R) systems [9,10,136-141], aircraft [142-149], energy conversion systems [150,151], and transportation platforms [152-155]. Ice accretion and frost formation is a multi-billion dollar problem in the United States [113]. Specifically, frost formation on heat exchanger surfaces in HVAC&R systems reduces heat transfer efficiency and results in significant economic losses [137,156-159], making defrosting a required engineering protocol. Broadly, two methods of defrosting exist: passive and active [160]. Passive methods use engineered surfaces to delay or reduce frost formation without additional power consumption. Active methods require additional power input for defrosting. With regards to passive defrosting methods, researchers have been developing hydrophobic [14] and superhydrophobic surfaces [15,16,81] in an attempt to delay frosting. The current approach to fabricate frost-reducing surfaces focuses on rough hydrophobic surfaces to increase the energy barrier for ice nucleation [14-16,18,19,81,90,114,119,161-164], and to further reduce both the contact angle hysteresis and the ice adhesion strength of the frost once it inevitably forms [106,165-169]. More recently, researchers have shown coalescence induced droplet jumping on ultra-low adhesion superhydrophobic surfaces to delay condensation frosting [115]. Droplet jumping enabled condensing droplets to escape at micrometric length scales (~1 μm) prior to supercooling and freezing on the surface [23,99].

In addition to jumping droplet condensate removal prior to freezing, studies have shown superhydrophobic surfaces to facilitate delayed freezing of individual droplets [116,117,170], as well as bulk water layers due to the delay in ice nucleation and higher thermal resistance at the liquid-solid interface [21,118], respectively. Although frosting delay has been shown with

superhydrophobic surfaces, complete elimination of frosting has not been achieved [24]. Given enough time, frosting will initiate and spread to cover the entire surface [23-25]. In lieu of this fact, anti-frosting surfaces that use sacrificial ice-stipes across the surface to keep the surrounding area dry for longer periods of time (> 3 hours) have been developed [171]. However, simple and passive defrosting strategies that guarantee no ice/frost formation on supercooled surfaces are lacking.

Due to the limitations in indefinitely preventing frost formation, industrial applications generally rely on active defrosting techniques. Three active defrosting methods exist: system defrosting, electro-hydrodynamics (EHD) [172], and oscillation/ultrasonic vibration [173,174]. Since EHD and vibration defrosting are not economically feasible, system defrosting is preferred. One system defrosting method utilizes reversal of the cycle direction to heat the working fluid and melt the frost [26,27]. However, (i) up to 27% of the total defrost heat input is used simply to heat up the evaporator [28], and (ii) up to 75% of the defrosting energy goes into heating the refrigeration system and not the ice [29]. Moreover, during frost, defrost, and refrost cycles, water retention is observed on the heat exchangers [30], which acts to decreases the overall heat transfer coefficient of a heat exchanger by 20% [10,31] and act as a seed layer for frost nucleation during the next frost cycle.

To eliminate water retention, we study dynamic defrosting on superhydrophobic (SHP) and biphilic surfaces. Our biphilic surfaces consist of spatially distinct ultra-low surface energy SHP ($\theta_a \rightarrow 180°$) and high surface energy hydrophilic ($\theta_a = 78°$) domains. Upon defrosting on a SHP region, the frost melts into a highly mobile slush. It was observed that the high mobility of slush enables the use of surface forces at hydrophilic regions to 'pull' the slush from SHP regions

95

prior to complete melting, even in the absence of external forces such as gravity or gas shear. We optimize the design of our biphilic surfaces for quicker cleaning of the surface during dynamic defrosting and for reduced water retention on SHP regions. Biphilic surface design optimization was performed for surfaces with horizontal (no gravity) and vertical (with gravity) configurations. Branched biphilic designs based on the banana leaf [175] were studied and optimized to achieve surface cleaning during dynamic defrosting. Furthermore, we studied the performance of biphilic surfaces during evaporation-mediated cleaning and drying of surfaces. Our work not only provides the fundamental design guidelines for the rational fabrication of biphilic surfaces for dynamic defrosting, it elucidates the role of wettability gradients on defrosting dynamics. Our results suggest avenues to further decrease defrost time by identifying critical bottlenecks in the process, and provide design methodologies to create effective defrost-enhancing surfaces for industrial applications.

5.3 Substrate Fabrication and Characterization

To fabricate the biphilic surface, first a microstructured superhydrophobic (SHP) CuO surface was fabricated, and later particular areas of the surface were laser ablated to make it hydrophilic. To fabricate the SHP CuO surface, commercially available polished multipurpose Cu tabs (30 mm x 30 mm x 0.8 mm) were used (99.90% purity). Each Cu tab was thoroughly rinsed with acetone, ethanol, isopropyl alcohol (IPA) and deionized (DI) water. The tabs were then dipped into a 5.0 M hydrochloric acid solution for 2 min to remove the native oxide film on the surface, then rinsed with DI water and dried with clean N_2 gas. Nanostructured CuO films were formed by immersing the cleaned tabs into a hot ($96 \pm 3°C$) alkaline solution composed of $NaClO_2$, $NaOH$, $Na_3PO_4 \cdot 12H_2O$, and DI water (3.75:5:10:100 wt. %) [129]. During the oxidation process, a thin (≈ 300 nm) Cu_2O layer was formed that then re-oxidized to form sharp, knife-like CuO oxide

structures with heights of $h \approx 1$ µm. Heptadecafluorodecyltrimethoxy-silane (HTMS, CAS # 83048-65-1) was deposited using vapor phase deposition to functionalize the surface [102]. Nanostructured CuO substrates were placed in a container with a vial of 1 mL HTMS toluene solution (5% v/v). A lid was placed on top to seal the container, followed by heating in an atmospheric pressure oven (Thermo Scientific BF51732C-1) at 90°C for 3 hours. This process allowed for the development of a highly conformal coating as the HTMS molecules evaporated from solution and covalently bonded with the free radicals on the surface. Contact angle measurements (MCA-3, Kyowa Interface Science Ltd.) of $\approx$300 nL droplets on an HTMS coated SHP CuO surface showed advancing/receding contact angles of $\theta_a{}^{app}/\theta_r{}^{app} \approx 170.5 \pm 7.2° / 162.7 \pm 3.4°$.

Particular areas on the SHP surface were laser ablated to make the surface biphilic [175]. A CO_2 laser source (Epilog Fusion M40) was used at 75 W power to ablate the HTMS coating and CuO microstructure from pre-defined areas. Scanning Electron Microscopy (SEM) images of the laser ablated region (Figure 1d) revealed that laser ablation melted the CuO nanostructures, making the surface flat and hydrophilic (HL) as compared to the structured superhydrophobic counterpart which was not irradiated (SHP, Figure 1d). Contact angle measurements on a homogeneous laser ablated SHP CuO surface showed advancing/receding contact angles of $\theta_a{}^{app}/\theta_r{}^{app} \approx 78 \pm 8.1° / 0°$. The laser ablation technique was used to fabricate various biphilic patterns as shown in Figure 1(c). Specifically, binary patterns with varying thickness of hydrophilic, L_{HL} and SHP, L_{SHP} regions as well as nature-inspired biphilic designs such as the banana leaf [175] were fabricated to study their dynamic defrosting performance.

To fabricate the sample base consisting of a nanostructured superhydrophilic (SHL) AlO(OH) sample, a commercially available Al tab (50 mm x 50 mm x 0.8 mm, 99.90% purity)

was first ultrasonically treated in acetone, followed by ethanol for 5 min each. After cleaning, the Al sample was dried in a clean N_2 stream. The Al sample was then immersed in hot deionized water (90°C) for one hour, followed by removal and rinsing with room temperature deionized water. This enabled boehmite ($Al_2O_3 \cdot xH_2O$) formation on the Al surface with sharp, knife-like structures having length scales approaching ≈300 nm [102]. Contact angle measurements on the AlO(OH) surface showed perfect wetting with apparent advancing contact angles of $\theta_a{}^{app} \rightarrow 0°$.

5.4 Experiment Methods

Dynamic defrosting was studied using a custom built set-up that enabled top-view and side-view optical access. The set-up is shown diagrammatically in Figure 1(a). A photograph of the set-up is shown in Figure 1(b). Samples were placed on the cold plate (Lytron Direct, CP10G14 Tubed Cold Plate) with a thin (≈ 100 µm) film of thermal paste (Apiezon N Grease) underneath in order to provide good thermal communication between the sample, base, and cold plate. The superhydrophilic AlO(OH) base was sandwiched between the sample and the cold plate. The superhydrophilic base acted as a sink for the defrost product (slush) which melted on the biphilic or SHP samples. The temperature of the superhydrophilic base, T_s was monitored using a surface K-type thermocouple (Omega SA1-K-120). The surface of the cold plate was oriented horizontally and vertically for different sets of experiments to study the effect of gravitational orientation. The cold plate was cooled using a chiller (Polyscience N0772046) circulating a mixture of water and ethylene glycol (50/50) at a flow rate of 11.8 ± 0.2 LPM. The sample temperature set point was $T_s = -15 \pm 0.9°C$ in the laboratory environment having air temperature, $T_{air} = 22 \pm 1.2°C$, and relative humidity (RH), $\Phi = 50 \pm 3\%$ (Roscid Technologies, RO120). The cooling cycle was

operated until a frost of thickness $h = 5$ mm was formed on the biphilic sample. The frost thickness was monitored actively using side view optical imaging with an accuracy of ± 0.5 mm, and typically took 77.9 ± 5.2 minutes to grow to $h = 5$ mm.

To vary the surface heating rate, two types of defrost methods were used for experiments: (i) heating the cold plate by setting the chiller at a higher temperature, or (ii) heating the sample by Joule heating a strip heater (McMaster-Carr Ultra-Thin Flexible Heat Sheet, 10 W/in². Density, 2" Long x 2" Wide, 120V AC) sandwiched between the base and the cold plate. For the cases where the sample was heated by changing the chiller set point, when $h = 5$ mm, the chiller was set to $T_{\text{chiller}} = 20 \pm 0.1°C$. For the cases where the sample was heated using a strip heater, when $h = 5$ mm, a DC power source (N5752A, Keysight Technologies) was used to energize the strip heater with 120 V, providing approximately 42.7 ± 1.2 W of heating. During Joule heating, the chiller was turned off, resulting in zero coolant flow. During the defrost cycle, T_s increased gradually. When T_s crossed the melting point of water, $T_{\text{melt}} = 0°C$, frost began to melt forming a highly mobile slush (water/frost mixture). The hydrophilic regions on the biphilic sample dynamically pulled the mobile slush, thereby cleaning the surface. The cleaning time, t_{cleaning} was characterized as the time from when the surface reached $T_s = 0°C$, to the time when complete cleaning of the SHP regions was achieved (zero surface coverage of slush) by dynamic movement of the slush on biphilic patterns. Defrosting movies were recorded from the top view and side view at 24 fps with a DSLR camera (Canon Rebel T3i, Canon EFS 18-55mm lens). To ensure repeatability, all experiments were conducted three separate times for every surface design and geometric orientation.

5.5 Results and Discussion

5.5.1 Horizontal Orientation

Figure 5.2 shows time-lapse images of dynamic defrosting on SHP and biphilic surfaces. The time $t = 0$ represents the instant when melting of frost was first observed visually. Figure 5.2(a) shows top-view time-lapse images of defrosting on a horizontal SHP surface. After defrosting, water retention was observed in the form of melt water that formed a puddle. To passively clean the surface during defrosting, dynamic defrosting was tested with biphilic surfaces that enable gradients in surface forces to remove the mobile slush. The hydrophilic regions on the biphilic surface pull the slush from the SHP regions, thereby cleaning the surface. Figure 5.2(b) shows top-view time-lapse images of defrosting on a horizontally oriented biphilic surface with $L_{SHP} = 1$ mm and $L_{HL} = 1$ mm. The hydrophilic regions dynamically pulled the slush during defrosting, eventually cleaning the surface. Figure 5.2(c) shows top-view time-lapse images of defrosting on a horizontally oriented biphilic surface with $L_{SHP} = 6$ mm and $L_{HL} = 1$ mm. Although the hydrophilic regions dynamically pulled the slush, complete cleaning of the surface was not achieved. Formation of satellite water droplets on the SHP areas was observed during the dynamic movement of slush. To clean the SHP areas of retained satellite water droplets, surface heating driven droplet evaporation had to be employed. To avoid the increased energy consumption due to heating, biphilic designs with no water retention were investigated.

To further optimize the cleaning performance with dynamic defrosting, branched biphilic surfaces inspired by the banana leaf were investigated [175]. Figure 5.2(d) shows top-view time-lapse images of defrosting on a horizontally oriented branched biphilic surface. On the branched surface, hydrophilic triangular branches originated from a hydrophilic trunk. During dynamic defrosting, the slush on the SHP regions initially moved in the direction of the hydrophilic branches

and later traveled transversely in the direction of the HL trunk. Therefore, during defrosting on branched surfaces, the slush traveled sequentially in two directions before it reaches the sink. It is important to note, the shape of the branches is an important feature which governs the passive capillary pumping of the slush. The branched regions are triangular in nature, diverging from the inner regions in close proximity to the SHP areas towards the trunk. The divergent channel creates a Laplace pressure gradient in the liquid that generates a capillary pumping force, which enables the passive flow of water and slush towards the trunk upon contact with the melt.

Figure 5.2(e) and 5.2(f) show top view and side view time-lapse images of defrosting on a vertically-oriented binary biphilic (aligned hydrophilic strips, L_{SHP} = 6 mm and L_{HL} = 2 mm) surface, respectively. During dynamic defrosting on the vertically oriented biphilic surface (Figure 5.2f), "*de-blooming*" was observed, characterized by slush lift-off from the SHP area coupled with coalescence with water droplets residing in the hydrophilic area. During defrosting on the vertical SHP surface, frost melted at the frost-surface interface with the remaining sheet of slush falling downwards from the surface due to gravitational force. Figure 5.2(f) shows that when frost melts at the frost-solid interface on a biphilic surface, although the frosts detaches from the SHP region due to gravity, it maintains attachment to the hydrophilic areas. At later times, the remaining sheet of frost-water mixture coalesced with water in the hydrophilic regions in a manner that is opposite of *blooming*, termed here as *de-blooming*. De-blooming was observed for vertically aligned biphilic surfaces, irrespective of the heating rate of the sample or orientation of the hydrophilic stripes.

To examine the physics of slush removal due to wettability gradients, we characterized the total cleaning time to remove the slush from the SHP surface. The total cleaning time, t_{cleaning},

was characterized as the time from when the surface thermocouple reached a value of $T_s = T_{melt}$ = 0°C, to the time that complete cleaning of the SHP regions by dynamic movement of the slush was attained. Figure 5.3(a) shows the cleaning time, $t_{cleaning}$, as a function of L_{SHP} on horizontally oriented (no gravity) biphilic surfaces (Figure 5.1c). Defrosting was achieved by changing the set point temperature on the chiller to 20 ± 1°C. To represent the biphilic designs that failed to achieve surface cleaning with remnants of satellite water droplets on the SHP areas, a value of $t_{cleaning}$ = 350 s was assigned. The hydrophilic surface with $L_{SHP} = 0$ (bare copper, $\theta_a{}^{app}/\theta_r{}^{app} \approx 40.4 \pm 3.8° / 0°$) exhibited water retention upon defrosting. The SHP surface ($L_{SHP} = 30$ mm) displayed water retention in the form of a melt water puddle (Figure 5.2a). Interestingly, biphilic surfaces with $L_{SHP} \leq 4$ mm exhibited complete cleaning during dynamic defrosting with no water residue remaining on the SHP areas. However, biphilic surfaces with $L_{SHP} > 4$ mm showed satellite water droplet retention on SHP areas after defrosting (Figure 5.2c).

Formation of satellite water droplets upon dynamic defrosting on superhydrophobic surfaces has been observed in the literature [176]. When a frost wave propagates on a superhydrophobic surface that exhibits coalescence induced droplet jumping, 1/3 of the condensate droplets freeze whereas 2/3 of the droplets evaporate [176]. The surface coverage of frozen droplets is thus minimum, and the frost dendrites that grow perpendicular to the surface on the frozen droplets are porous [176]. When a frost sheet of thickness < 2 mm defrosts, since the frost is porous and not well interconnected, it forms multiple droplets upon dewetting [176]. It was observed that during defrosting on biphilic surfaces, frost melts at the frost-solid interface. The melt water formed beneath the frost is continuously drained by the hydrophilic regions decreasing the thickness of the frost sheet. For biphilic surfaces with larger superhydrophobic regions (L_{SHP} > 4 mm) when a thin porous frost sheet melts, the neighboring hydrophilic regions pull the melt

water from the superhydrophobic region, however, the frost chunk that is not interconnected breaks up and form isolated satellite water droplets on the superhydrophobic regions. Moreover, increasing the superhydrophobic area on a biphilic surface allows for more water to build up in between hydrophilic region, increasing the possibility of formation of satellite droplets. For biphilic surfaces with thinner superhydrophobic regions ($L_{SHP} \leq 4$ mm), draining of the melt water keep occurring until all the frost is melted with little chance of water building up on the superhydrophobic region. Plateau-Rayleigh instability might lead to melt water break up to form satellite water droplets for biphilic surfaces with larger superhydrophobic area [57]. However, with very low liquid flow velocities (< 1 mm/s) where inertial and viscous forces are comparable, and surfaces forces are dominant, Plateau-Rayleigh instability seems unlikely to occur.

To further optimize the design of the biphilic surfaces, we studied branched bipihilic designs. The branched sample 1 (Branched 1) design was used from the banana leaf biphilic surface design [175]. Upon conducting dynamic defrosting on Branched 1, we observed that water droplets lodged between adjacent hydrophilic branches (inset of Figure 5.3a).

The divergent channels generate a capillary force, F_{cx} that is directly proportional to the angle subtended by the triangular branches, α ($F_{cx} \propto \alpha$) [177,178]. To assist melt-water removal on the branched samples, the angle subtended by the triangular hydrophilic branches, α was increased (from $\alpha = 1.8°$ for Branched 1 to $3.6°$ for Branched 2) to enhance the differential surface force. Furthermore, the distance between two adjacent hydrophilic branches was increased to avoid lodging of water droplets between them. As a result, Branched 2 showed complete cleaning of the surface during dynamic defrosting (inset of Figure 5.3a). However, it was observed that the cleaning time, $t_{cleaning}$ of Branched 2 was higher than binary biphilic samples with $L_{SHP} \leq 4$ mm. The longer cleaning time could be explained by the analysis of slush motion. During dynamic

defrosting on branched biphilic surfaces, the frost-water slush has to first move in the direction of the hydrophilic branches and subsequently travel in the transverse direction to the main hydrophilic trunk. As the slush has to travel sequentially in two orthogonal directions prior to reaching the sink, t_{cleaning} on the branched biphilic surfaces is higher compared to the binary biphilic surfaces where the melt water travels in one principal direction during defrosting.

To understand the versatility of biphilic surfaces during different defrosting methods, we studied the effect of the surface heating rate. Two types of defrost methods were used to vary the surface heating rate: (i) heating the cold plate by setting the chiller at a higher temperature, and (ii) heating of the base by Joule heating. Figure 3(b) shows the temperature of the base (T_{s}) as a function of time for the two heating methods. The Joule heating method had a 3-4X higher surface heating rate than the chiller re-heat method. Figure 5.3(c) shows the cleaning time, t_{cleaning} as a function of L_{SHP} on horizontally oriented binary biphilic surfaces using the different heating rates. As expected, irrespective of the heating rate, water retention was observed for $L_{\text{SHP}} > 4$ mm during defrosting whereas biphilic surfaces with $L_{\text{SHP}} \leq 4$ mm showed surface cleaning. The SHP and hydrophilic surfaces showed water retention. Thus, it can be concluded that for horizontally oriented surfaces, to achieve complete cleaning while dynamic defrosting, biphilic designs with 1 mm $\leq L_{\text{SHP}} \leq 4$ mm, and 1 mm $\leq L_{\text{HL}} \leq 2$ mm should be used.

During defrosting on the biphilic surfaces, water is retained at the hydrophilic regions. In certain settings, a dry surface is desired upon defrosting in order to eliminate the chance of re-frosting on existing nucleation sites. To avoid the chance of melt water retention, defrosting is done by surface heating until all moisture is evaporated completely. To understand the effect of various biphilic surface designs on evaporation-mediated surface cleaning, we studied the evaporation dynamics of retained water on biphilic surfaces post-defrosting. During the defrosting

104

cycle, the surface was heated to $T_s = 49.4 \pm 4.2°C$ using strip heaters. Figure 5.3(d) shows the time taken for complete evaporation of water during defrosting, $t_{evaporation}$ on horizontally oriented biphilic surfaces as a function of L_{SHP}. The evaporation time, $t_{evaporation}$ was characterized as the time from $T_s = T_{melt} = 0°C$ to the complete cleaning of the surface of water. We observed that for $L_{SHP} \leq 4$ mm, $t_{evaporation}$ for $L_{HL} = 1$ mm is 50% lower than $t_{evaporation}$ for $L_{HL} = 2$ mm. For $L_{SHP} \leq 4$ mm, satellite water droplets were not formed, and the melt water was present only at the hydrophilic sites of the biphilic surface. Assuming an equivalent receding contact angle, the amount of meltwater present in the hydrophilic areas with $L_{HL} = 2$ mm was greater than for samples having $L_{HL} = 1$ mm. Therefore, the thermal resistance to evaporation of the melt water for samples having $L_{HL} = 2$ mm was greater than samples having $L_{HL} = 1$ mm. The higher thermal resistance led to slower evaporation and longer evaporation times ($t_{evaporation}$). However, for samples having $L_{SHP} > 4$ mm, satellite water droplets remained on the SHP areas that needed to be evaporated. The size of the retained satellite water droplets was random, irrespective of L_{SHP} or L_{HL}. Thus, for $L_{SHP} > 4$ mm, no relationship existed between $t_{evaporation}$ and L_{HL} as the dominant limitation to full cleaning was the evaporation of superhydrophobic-state satellite droplets. Indeed, this result agrees with prior studies which show increasing sessile droplet evaporation time with increasing apparent contact angle in ambient (moist air) conditions [179-181].

5.5.2 Vertical Orientation

In order to study the defrosting behavior in the presence of gravity, the cold plate was oriented vertically and experiments repeated. Figure 5.4(a) shows the cleaning time, $t_{cleaning}$ for vertically oriented biphilic surfaces as a function of L_{SHP}. The hydrophilic stripes were parallel to the gravitational vector as shown in the inset of Figure 5.4(a). To represent the biphilic designs that failed to achieve surface cleaning and exhibited satellite water droplets or water retention,

$t_{\text{cleaning}} = 140$ s was arbitrarily assigned to them. Experiments revealed that the hydrophilic surface ($L_{\text{SHP}} = 0$) showed water retention. The SHP surface had the lowest t_{cleaning} and best defrosting performance. During defrosting on the vertically oriented SHP surface, frost melted at the frost-surface interface, and the remaining slush fell instantaneously due to gravity, thereby reducing t_{cleaning}. Although, t_{cleaning} for the SHP surface was the lowest, t_{cleaning} for biphilic surfaces was within 30% of that observed on the SHP surface. *De-blooming* (Fig. 2e, f) acted to accelerate defrosting for biphilic surfaces.

To study the effect of the orientation of the hydrophilic stripes with respect to gravity, we re-oriented samples on the vertical setup by rotating them by 90°. Figure 5.4(b) shows the cleaning time, t_{cleaning} for vertically oriented biphilic surfaces as a function of L_{SHP}. Here, the hydrophilic stripes were perpendicular to the gravitational vector (Figure 5.4b, inset). We observed that the order of magnitude of t_{cleaning} was similar (~ 50 s for defrosting using chiller, and ~ 20 s for defrosting using electric strip heaters) irrespective of the orientation of hydrophilic stripes with respect to gravity. Re-orientation of the hydrophilic stripes did not affect the dynamic defrosting performance of the biphilic surfaces. Although the SHP surface showed the best dynamic defrosting performance in the vertical configuration, biphilic surfaces showed similar results which were much better than unaltered surfaces.

Analogous to experiments conducted in the horizontal configuration, dynamic defrosting on the vertically oriented biphilic surfaces resulted in water retention on the hydrophilic regions. To understand the effect of biphilic surface design on evaporation led surface cleaning, we studied evaporation-mediated defrosting of the complete surface (complete water removal). During the defrosting cycle, the surface was heated to $T_s = 49.4 \pm 4.2°C$ using strip heaters. Figure 5.5 shows the time taken for complete evaporation of water, $t_{\text{evaporation}}$ from the vertically oriented biphilic

surface as a function of L_{SHP}. The evaporation time, $t_{\text{evaporation}}$ was characterized as the time from $T_s = T_{\text{melt}} = 0°C$ to the complete drying of the surface. In accordance with the horizontal orientation results, $t_{\text{evaporation}}$ for $L_{\text{HL}} = 1$ mm was 25% lower than $L_{\text{HL}} = 2$ mm due to the added thermal resistance of the retained water in the hydrophilic regions. Unlike the horizontal configuration, no satellite water droplet retention was observed when the samples were oriented vertically. The ultra-low adhesion on the SHP surface resulted in rapid gravitational shedding of the slush. Hence, $t_{\text{evaporation}}$ for $L_{\text{HL}} = 1$ mm is lower than $L_{\text{HL}} = 2$ mm for all L_{SHP} as opposed to the horizontally oriented biphilic surfaces where the trend deviates for $L_{\text{SHP}} > 4$ mm as shown in Figure 3(d).

The dynamic defrosting experiments performed in this study for horizontally and vertically oriented SHP and biphilic surfaces with varying surface heating rates demonstrate that biphilic surfaces have the capability to clean the surface effectively during defrosting. Hydrophilic regions pull the melting slush from the SHP region during defrosting. Biphilic surfaces designed to avoid satellite droplet formation were more effective in surface cleaning. Our experiments suggest that the satellite droplet formation can be avoided by designing biphilic surfaces with $L_{\text{SHP}} < 4$ mm. For applications wherein a completely dry surface is desired, biphilic surfaces with thinner hydrophilic areas are preferred ($L_{\text{HL}} = 1$ mm).

In the future, the study of a complete cycle or multiple cycles: frosting, defrosting and refrosting, on biphilic surfaces will be critical to fully understand the overall cycle performance. Indeed, the experiments conducted here were done with a superhydrophilic base which acted as an ideal sink for slush and water. Real life implementation of biphilic surfaces for dynamic defrosting must consider this fact and implement water sinking features. Furthermore, the study of the defrosting performance for varying thicknesses is required to understand the limits of biphilic

surface designs. Dynamic defrosting on biphilic surfaces at oblique inclinations should be studied to mimic the defrosting in real life applications, where the orientation of the defrosting surface may not be ideally horizontal or vertical.

Future work on frost-defrost cycling on real life heat exchangers coated with biphilic surfaces is needed in order to fully understand the feasibility of our approach at larger length scales. Furthermore, although quantified here for condensation frosting conditions, where the frost formed is porous and has a low density, future work is needed to better understand biphilic defrosting on surfaces which undergo ablimation frosting, common in refrigeration and heat pumping applications. In addition, the results reported here are for ideal single coupon samples with infinite room for frost growth and slush/melt-water dynamics. In real systems, the spacing between frosting surfaces rarely exceeds 2 mm, resulting in significant potential for interaction between surfaces. Indeed, although the defrosting performance on homogeneous superhydrophobic surfaces was shown to be best when compared to its unaltered and biphilic counterparts, the same cannot be concluded for cases where significant surface-surface interactions may act to block the motion of slush down the surface (e.g. louvered heat exchanger fins) which act to increase defrosting time when compared to unaltered heat exchangers [182]. It would be interesting to investigate the defrosting techniques outlined here in more realistic conditions with finite spatial constraints for dynamic defrosting as well as in gas shear conditions, both of which are prevalent in the HVAC&R industry. Furthermore, a detailed study on the economic impact in terms of the payback period for the input costs associated with biphilic surface fabrication should be done. Lastly, the durability of the biphilic surfaces under repeated frosting-defrosting cycles must be tested to meet the requirements of the HVAC industry.

5.6 Conclusions

We rigorously studied the defrosting behavior on hydrophilic, superhydrophobic, and biphilic (hydrophilic/superhydrophobic) surfaces. Using tip and side view optical imaging, we showed that superhydrophobic regions undergo dynamic defrosting, where the frost layer initiates spontaneous motion via the formation of highly mobile slush. Due to the difference in the surface forces on biphilic surfaces, the hydrophilic regions acted to 'pull' the mobile slush prior to complete frost melting, even in the absence of forces such as gravity or vapor shear. Horizontally oriented biphilic surfaces having SHP regions of thickness $L_{SHP} \leq 4$ mm showed enhanced defrosting behavior when compared to unaltered or fully SHP surfaces. For biphilic surfaces with $L_{SHP} > 4$ mm, satellite water droplets remained on the SHP areas. The formation of satellite droplets was observed irrespective of the surface heating rate. To understand the effect of pattern heterogeneity, we studied banana-leaf-inspired branched biphilic patterns optimized to minimize cleaning time. We observed that binary biphilic designs were simpler to manufacture when compared to branched designs, and offered better surface cleaning performance during defrosting. Defrosting utilizing full evaporation showed that designs with hydrophilic regions of thickness, $L_{HL} = 1$ mm performed better than $L_{HL} = 2$ mm for $L_{SHP} \leq 4$ mm, due to lower thermal resistance of retained water. During dynamic defrosting on vertically oriented surfaces (with gravity), SHP samples exhibited the best cleaning performance, with biphilic surfaces within 30% of the minimum cleaning time. Our work not only provides the fundamental understanding required for the design of heterogeneous defrosting coatings, but also elucidates the role of wettability gradients on defrosting dynamics.
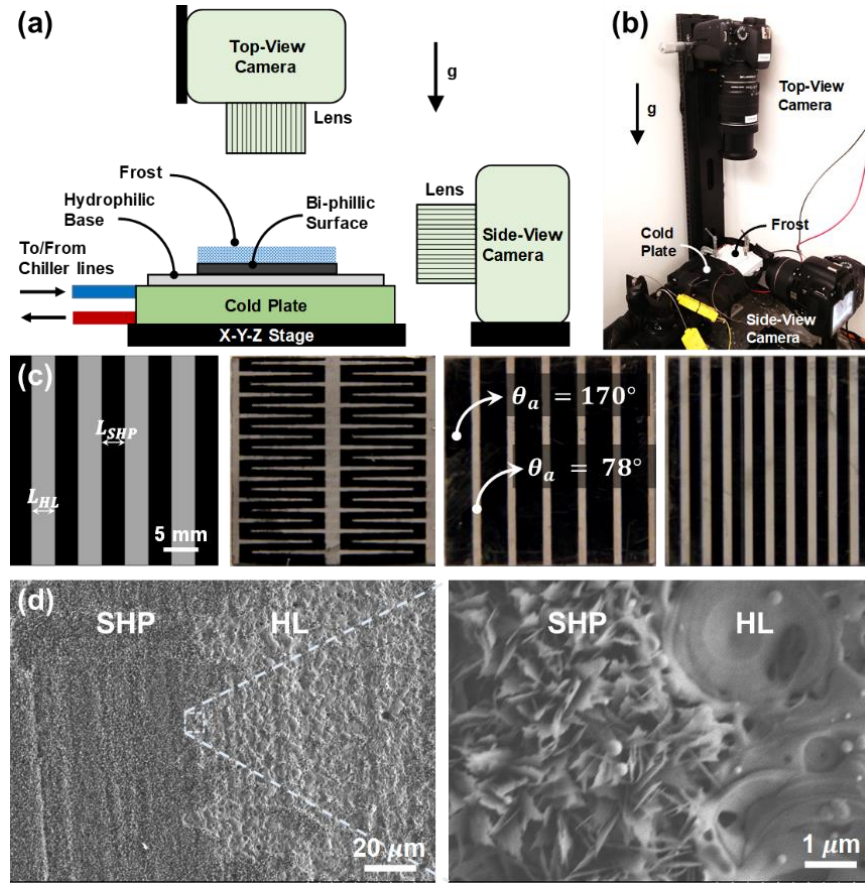
5.7 Figures

Figure 5.1. (a) Schematic of the experimental setup. The temperature of the biphilic surface was maintained at T_s = -15 $\pm$ 0.9°C with ambient temperature and relative humidity of T_{air} = 20 $\pm$ 0.9°C and ϕ = 50 $\pm$ 3%, respectively. (b) Picture of the actual experimental setup. (c) Schematic and top view optical photograph of copper-based biphilic surfaces. The black regions represent CuO superhydrophobic (SHP) areas (θ_a^{app} = 170.5 $\pm$ 7.2°) and gray region represents laser ablated hydrophilic (HL) areas (θ_a = 78 $\pm$ 8.1°). To explore the effect of pattern heterogeneity, various binary and branched biphilic patterns were fabricated. (d) Scanning electron micrograph of the biphilic surface shown in (c) at the SHP-hydrophilic interface (black-gray interface). The region on the left is the SHP area while the region on the right is the HL area. The laser ablates the CuO structures and HTMS coating leading to the formation of a hydrophilic domain.
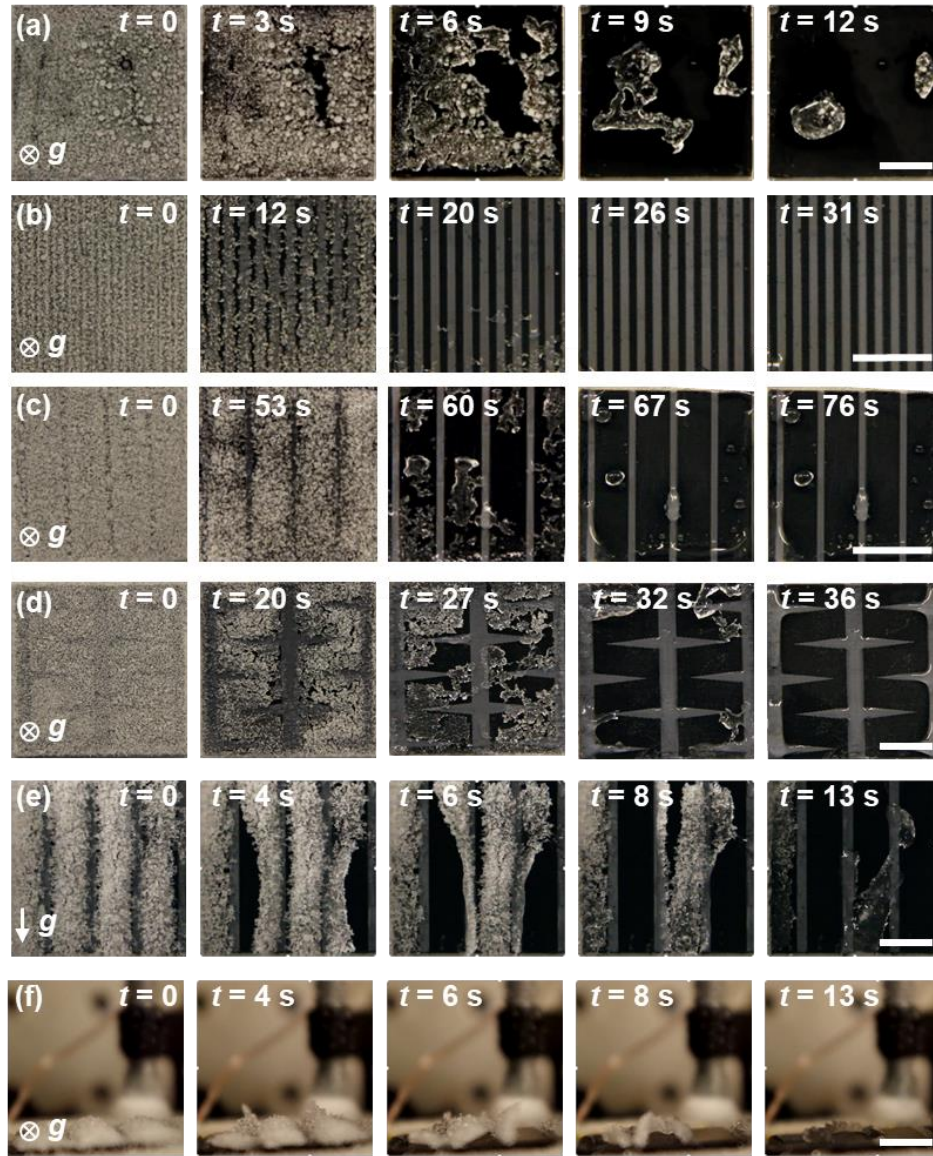
Figure 5.2. Time-lapse images of dynamic defrosting on a horizontally-oriented (a) SHP surface wherein water retention after defrosting was observed, (b) binary biphilic surface (L_{SHP} = 1 mm and L_{HL} = 1 mm) wherein complete surface cleaning was observed, (c) binary biphilic surface (L_{SHP} = 6 mm and L_{HL} = 1 mm) wherein water retention in the form of satellite water droplets was observed, and (d) branched biphilic surface wherein complete surface cleaning was observed. (e) Top view and (f) side view time-lapse images of defrosting on a vertically-oriented binary biphilic (L_{SHP} = 6 mm and L_{HL} = 2 mm) surface. The results of (f) show the *de-blooming effect*, wherein frost lifts off the SHP area and is pulled by the coalescing water droplets in the hydrophilic area. The scale bar for all images is 9 mm.
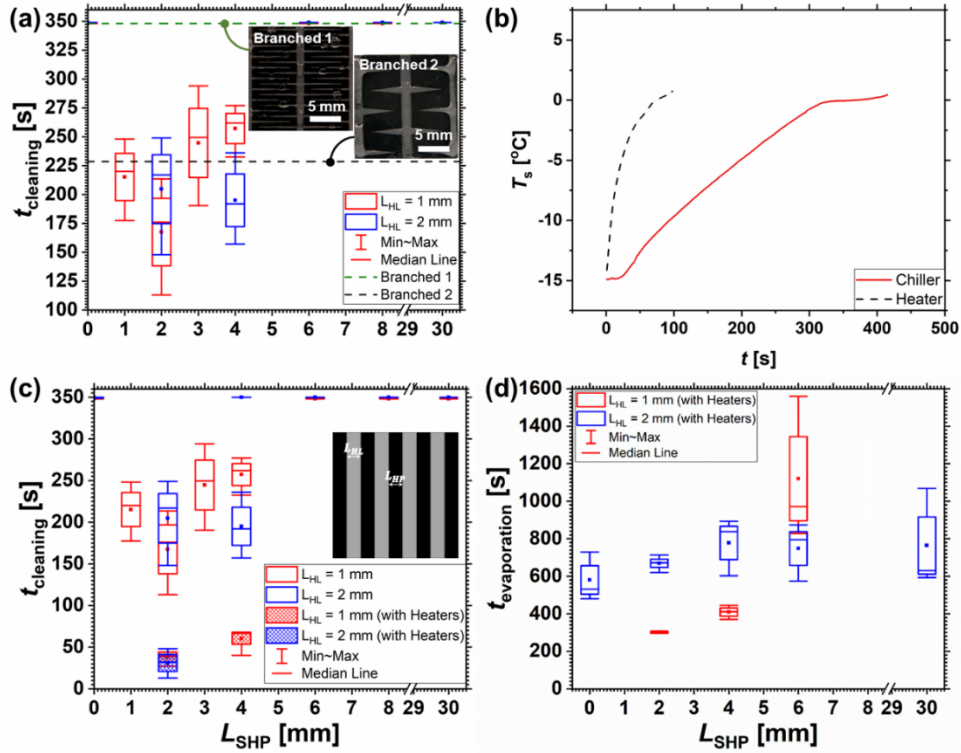
111

Figure 5.3. (a) Cleaning time, $t_{cleaning}$ as a function of L_{SHP} on a horizontally oriented binary biphilic surface. Defrosting was achieved by changing the set point temperature on the chiller to 20°C. The data points corresponding to $t_{cleaning} = 350$ s denote cases where water retention was observed and the surface was not completely cleaned. For $L_{SHP} > 4$ mm, satellite water droplets were left in the SHP areas after defrosting, leading to water retention on the surface. Inset: Optical top-view images of the branched biphilic samples 1 and 2 after dynamic defrosting (b) Temperature of the biphilic surface as a function of time for the two different heating methods. In order to achieve quicker heating, electric strip heaters underneath the biphilic surface were used. (c) Cleaning time, $t_{cleaning}$ as a function of L_{SHP} on a horizontally oriented binary biphilic surface for different heating rates. Irrespective of the heating rate, water retention was observed for $L_{SHP} > 4$ mm during defrosting. Inset: Schematic of a binary biphilic sample. (d) Time taken for complete evaporation of water from the horizontally oriented biphilic surface during defrosting, $t_{evaporation}$ as a function of L_{SHP}. The biphilic surface was heated using electric strip heaters. Boxes represent the standard deviation in the experiment data, whereas the whiskers represent the minimum and maximum of the measured values.

112
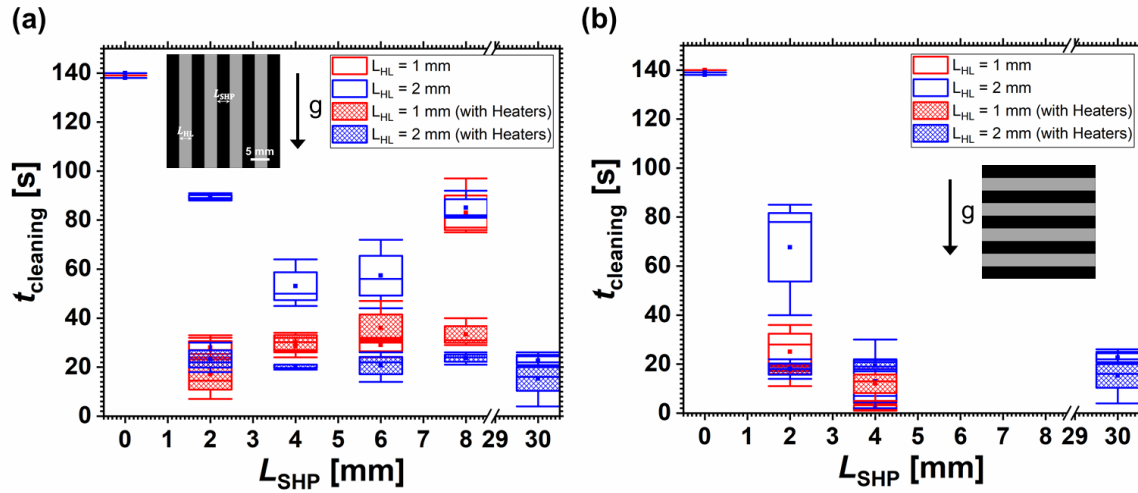
Figure 5.4. Cleaning time, $t_{cleaning}$ as a function of L_{SHP} on a vertically oriented binary biphilic surface for different heating rates with hydrophilic stripes (a) parallel and (b) perpendicular to the gravitational vector. Inset: schematics of the orientation of the biphilic surface with respect to the gravitational vector. The SHP surface (L_{SHP} = 30 mm) showed the fastest cleaning for vertically oriented surfaces. The order of magnitude of $t_{cleaning}$ was similar irrespective of the orientation of hydrophilic stripes with respect to gravity. The boxes represent the standard deviation in the experiment data, whereas whiskers represent the minimum and maximum of the measured values.

Figure 5.5. Time taken for complete evaporation of water from the vertically oriented biphilic surface during defrosting, $t_{\text{evaporation}}$ as a function of L_{SHP}. The biphilic surface was heated using electric strip heaters. The boxes represent the standard deviation in the experiment data, whereas whiskers represent the minimum and maximum of the measured values.
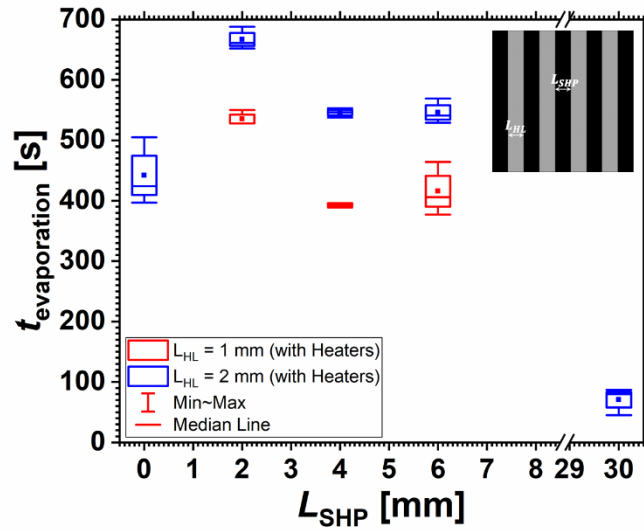
CHAPTER 6: PULSE INTERFACIAL DEFROSTING

6.1 Overview

Frost formation and ice accretion is a major problem for a plethora of industries. Common defrosting and deicing techniques utilize energy-intensive mechanical actuation to dislodge or heating methods to melt ice/frost from the surface. Here, we study an ultra-efficient method to defrost a surface covered with ice/frost by focusing energy at the substrate-ice interface. To remove ice/frost efficiently, it is beneficial only to melt the interfacial layer adhering the ice/frost to the solid surface by using a localized 'pulse' of heat, allowing gravity or gas shear in conjunction with the ultra-thin lubricating melt water layer to remove the ice/frost. To probe the physics of the pulse defrosting process, we developed a transient numerical heat transfer model of interfacial pulse-defrosting. Experimental validation of the model was achieved via pulse ($\approx$100 ms) Joule heating of indium tin oxide (ITO) coated on glass samples. Utilizing transient heat fluxes ranging from 10 to 100 W/cm^2, spontaneous melting of the interfacial ice/frost layer was achieved leading to rapid ice removal. We employed the model to outline design guidelines for interfacial pulse-defrosting applications, showing that pulse defrosting uses 0.56% energy and 0.0032% defrosting time, when compared to conventional defrosting methods. This study not only provides a fundamental knowledge base for the design of ultra-efficient defrosting and deicing surfaces but also elucidates the role of transient energy and hydrodynamic effects during interfacial defrosting.

6.2 Introduction

Understanding the mechanisms of frost formation is essential to a variety of industrial applications including refrigeration [9,10,82], aviation [11], wind energy generation [12], and power transmission [13]. Ice accretion and frost formation are multi-billion dollar problems in the

United States alone [113]. To delay frost formation, researchers have proposed the use of suitably designed superhydrophobic surfaces [15-17,81,118] to delay the heterogeneous nucleation of ice [18,19,90] as well as condensation frosting [20,170]. Although relying on surface wettability to delay frosting is passive, given enough time, frost formation during condensation frosting ensues due to the propagation of an inter-droplet frost wave from neighboring edge defects [23,183]. In building energy applications, methods to remove frost from the surfaces of thermal components use electric heaters or hot-gas from the compressor to melt frost, which results in a further increase in energy consumption, and downtime. The most common approach reverses the cycle direction and inefficiently heats the working fluid to melt the frost. Of the energy input for defrost [28], and up to 75% goes into heating the refrigeration system instead of the frost/ice [29].

A need exists for defrosting approaches that are more energy efficient and quicker. Past studies have investigated electro-thermal Joule heating for de-icing applications [32-35], demonstrating a high energy requirement to achieve thermal de-icing. In order to mitigate high energy consumption, pulse electro-thermal defrosting has been proposed in the past [36,37], wherein melting of the interfacial layer adhering the ice to the solid surface allows gravity in conjunction with the ultra-thin lubricating meltwater layer to remove the ice/frost. However, accurate transient phase change heat transfer models of the pulse-defrosting process are currently not available. Furthermore, the coupling of transient lubricating film physics with the transient thermally driven phase change processes has not been explored.

In this Chapter, we developed a one-dimensional transient numerical heat transfer model to study interfacial pulse-defrosting physics. We employed the enthalpy method to solve the phase-change problem. For a given defrosting problem and available power input the duration of the

pulse required for spontaneous interfacial defrosting of ice at an arbitrary temperature is predicted using appropriate time-dependent boundary conditions. To validate the model experimentally, we performed pulse-defrosting experiments by Joule heating of indium tin oxide (ITO) coated on glass samples in the vertical orientation with gravity parallel to the sample face. To study the effects of initial substrate conditions conducive to building energy applications as well as aerospace icing, pulse defrosting was studied using substrate temperatures of T_s = -15.1 $\pm$ 1.2°C and -71 $\pm$ 4.6°C, respectively. With heat fluxes ranging from 10 to 100 W/cm^2, spontaneous melting of the interfacial ice layer was achieved leading to rapid ice removal from the surface due to interfacial lubrication and gravitational shedding. The defrost time using thin film ITO heaters in conjunction with energy pulses was significantly lower (0.0032%) than for conventional steady heating methods. The experimental results showed excellent agreement with our developed model. Due to the high durability of ITO, the heater thickness was limited to less than 10 µm, limiting added parasitic thermal resistance for heat exchanger applications. We employ our model to outline design guidelines for interfacial pulse-defrosting applications. This study not only provides a fundamental knowledge base for the design of efficient defrosting surfaces, but also elucidates the key and coupled roles of energy and hydrodynamic effects at the interface during pulse defrosting.

6.3 Numerical Model

In the solution of the phase change problem, the enthalpy form of the energy equation (Eq. 6.1) [184], is equivalent to the usual temperature form in which the heat equation is written separately for the liquid and solid regions and coupled by an energy balance at the solid-frost/ice interface. Hence, the governing equations for solid and liquid phases need not be separated, and can be represented as:

$$\rho \frac{\partial h}{\partial t} = k \frac{\partial^2 T}{\partial x^2} + \dot{q} , \tag{6.1}$$

where ρ, h, and k are the are the density, enthalpy, and thermal conductivity, respectively, t is time, T is local temperature, and x is the distance in the domain as defined in Figure 6.1(a). To solve Eq. (6.1), we use the finite difference approximation in space and time using the implicit scheme [185]:

$$\rho \frac{h_i^{n+1} - h_i^n}{\Delta t} = k \frac{T_{i-1}^{n+1} - 2T_i^{n+1} + T_{i+1}^{n+1}}{\Delta x^2} + \dot{q} , \tag{6.2}$$

where the subscript i denotes spatial discretization and the superscript n denotes time discretization. At every time step, we assumed a guess temperature, $T^*(x, t_{n+1})$, equal to the temperature solution obtained from the previous time step, $T^*(x, t_{n+1}) = T(x, t_n)$. We used the Taylor series approximation of enthalpy as a function of temperature at the current time step (t_{n+1}):

$$h(T_i^{n+1}) = h^* + \left(\frac{\partial h}{\partial T} \right)^* (T_i^{n+1} - T_i^*), \tag{6.3}$$

where '$*$' indicates a parameter evaluated based on the best guess for temperature. Substituting Eq. (6.3) into Eq. (6.2) results in a discrete equation for the interior cells:

$$\left[\left(\frac{\partial h}{\partial T} \right)^* + \frac{2k\Delta t}{\rho \Delta x^2} \right] T_i^{n+1} = \frac{k\Delta t}{\rho \Delta x^2} (T_{i-1}^{n+1} + T_{i+1}^{n+1}) + h_i^n + \left(\frac{\partial h}{\partial T} \right)^* T_i^* - h^* + \frac{\Delta t \dot{q}}{\rho}. \tag{6.4}$$

Equation (6.4) was solved iteratively to obtain the temperature at the current time step, T_i^{n+1}. At every time step, the guess temperature was updated until the maximum relative error reached a value less than 10^{-4}. Figure 6.1(a) represents the model domain for which Eq. (6.4) was solved having an ice/frost thickness l_i on a substrate with thickness l_s. The pulse heating element of thickness l_{he} is sandwiched between the substrate and ice/frost. Note, for every spatial cell i, the physical properties (ρ, k, h) are determined based on the material in that cell: substrate for $0 < x \leq l_s$, pulse heater for $l_s < x \leq l_s + l_{he}$, and water/ice/frost for $l_s + l_{he} < x \leq l_s + l_{he} + l_i$. For the water/ice/frost domain, the cell was assumed to be ice/frost if the guess temperature of the cell was $T_i^* < T_m$, and liquid water if $T_i^* > T_m$, where $T_m = 0°C$. Initially, at time $t = 0$, the substrate and ice block are maintained at temperature, T_s. When the heating element is supplied by a pulse of Joule heating, a volumetric heat generation, $\dot{q}$ is released into the heating element ($l_s < x \leq l_s + l_{he}$) for a finite time defined by the pulse width τ. The heat released into the heating element is allowed to diffuse into the substrate and ice/frost domain and results in the melting of a transient and finite water layer at the interface having thickness l_w. The creation of a thin lubricating water layer at the ice/substrate interface initiates sliding of the ice/frost. The transient velocity of the sliding ice/frost layer is governed by a force balance between the gravitational body force F_g on the ice/frost bulk, and the transient and velocity-mediated shear force F_{shear} in the lubrication layer retarding the motion. For simplicity, we assumed that the lubricating layer develop into a stable Couette flow. In order to determine the critical thickness of the melt water layer, $l_{w,c}$ needed for complete removal of the ice/frost block, we equated $F_g = F_{shear}$, and obtained:

$$l_{w,c} = \frac{\mu_w v}{l_i \rho_i g}, \tag{6.5}$$

where μ_w is the temperature-dependent melt-water dynamic viscosity, v is the sliding velocity, and g is the gravitational constant. The initial condition applied to the ice slab was, $T(x, t = 0) = T_s$. The boundary conditions applied to the domain were:

$$-k\frac{\partial T}{\partial x}\Big|_{x=0} = 0\,, \tag{6.6}$$

$$-k\frac{\partial T}{\partial x}\Big|_{x=l_s+l_{he}+l_i} = h_i[T(l_i, t) - T_a]\,. \tag{6.7}$$

Equation (6.6) represents the symmetric boundary condition applied at $x = 0$. For time $0 < t \leq t_{pulse}$, the heating element is Joule heated with volumetric heat generation of $\dot{q}$. For time, $t > t_{pulse}$, Joule heating is arrested resulting in zero energy input ($\dot{q} = 0$) in the heating element ($l_s < x \leq l_s + l_{he}$). During $t > t_{pulse}$, the water melt layer refreezes due to cooling by the adjacent ice block at $x > l_w$. To solve Eq. (6.4), the derivative of the enthalpy with respect to temperature was required (Fig. 6.1b), which is ill-defined at the melting temperature $T_m = 0$°C. In order to resolve the numerical discrepancy, the approximate enthalpy of water was calculated for a mushy zone with solidus temperature, $T_{sol} = -0.5$°C and liquidus, $T_{liq} = 0.5$°C:

$$h = \begin{cases} C_{p,i}T & T \leq T_{sol} \\ \left(\dfrac{T_{liq} - T}{T_{liq} - T_{sol}}\right)C_{p,i}T + \left(\dfrac{T - T_{sol}}{T_{liq} - T_{sol}}\right)C_{p,w}T + \left(\dfrac{T - T_{sol}}{T_{liq} - T_{sol}}\right)L & T_{sol} < T < T_{liq}. \\ L + C_{p,w}T & T \geq T_{liq} \end{cases} \tag{6.8}$$

At the interface of two dissimilar materials ($x = l_s$, $x = l_s + l_{he}$, and at the ice/frost-water interface), the thermal conductivity was calculated by taking the harmonic mean of the two

dissimilar materials, $k_{\text{interface}} = 2k_1 k_2/(k_1 + k_2)$. Equation (6.4) was solved to obtain the transient temperature profile $T(x, t)$ subject to boundary conditions given by Eq. (6.6) and (6.7), and enthalpy defined by Eq. (6.8). A glass substrate, $l_s = 1$ mm with an ITO coating, $l_{\text{he}} = 50$ μm which acts as the pulse-heating element was used in the simulation domain. Glass was chosen as the substrate material in order to obtain results that can be verified with experiments, and ITO was chosen as the heating element due to its prevalent use in steady heating applications for current airframe systems. The input parameters used to compute model results covering different regimes of frosting and defrosting were: T_s = -15°C (building energy applications), and -70°C (aerospace applications); t_{pulse} = 0.1, 0.2, 0.3, 0.4, and 0.5 s; heat flux at the ITO coating, $q''_{\text{in}} = \dot{q} l_{\text{he}} = 93$, 62, 31, and 15.5 W/cm^2. The thickness of the ice block, l_i is taken to be 5 mm, which results in $l_{\text{w,c}}$ = 28.3 μm.

6.4 Model Results and Discussions

Figure 6.2(a) shows the temperature profile inside the melting ice block as a function of location for ascending time intervals for T_s = -70°C, Δt_{pulse} = 0.5 s, q''_{in} = 62 W/cm^2. For $t \leq 0.5$ s, the temperature of the glass substrate and ice/frost layer rises due to the rapid heat generation at the ITO coating at x = 1 mm. After $t > \Delta t_{\text{pulse}}$, the heat generation at the ITO coating ceases, while the temperature of the melted ice layer decreases, which results in refreezing with concurrent heating of the adjacent ice block on the right side due to heat diffusion. For effective pulse-defrosting, the critical thickness of the melt water layer, $l_{\text{w,c}}$ must remain liquid long enough to enable the adjacent ice block to slide off completely from the surface due to gravity. In order to determine the duration of pulse-heating required for spontaneous de-frosting, we plotted the temperature at the melt layer, T_{ml} at $x = l_{\text{w,c}}$ (Fig. 6.1a) as a function of time for various pulse

durations and $T_s = -70°C$, and $q''_{in} = 62$ W/cm^2 (Fig. 6.2b). For spontaneous defrosting, T_{ml} should be greater than the liquidus temperature, $T_{ml} > T_{liq}$. Figure 6.2(b) reveals that for a pulse duration of $\Delta t_{pulse} \geq 0.3$ s, successful pulse defrosting is achieved for samples that are 50 cm tall. For shorter pulse durations, the chance of re-freezing and sticking to the substrate prior to ice/frost removal becomes a greater concern.

In order to understand the effect of pulse width or energy input on defrosting dynamics, we varied the input heat flux in our simulations for a substrate temperature, $T_s = -70°C$. Figure 6.2(c) shows T_{ml} as a function of time for various input heat fluxes for input conditions $T_s = -70°C$, and $\Delta t_{pulse} = 0.2$ s. The results show that for input heat fluxes, $q''_{in} < 62$ W/cm^2, the ice at $x = l_{w,c}$ does not melt ($T_{ml} < T_{sol}$) for the pulse duration of 0.2 s. With further increase in the input heat flux to $q''_{in} = 93$ W/cm^2, melting of the ice at $x = l_{w,c}$ commenced. For low substrate temperatures ($T_s < -50°C$) and pulse durations (< 0.2 s), high input heat fluxes $q''_{in} > 90$ W/cm^2 are required to achieve spontaneous pulse-defrosting. To better understand the role of substrate temperature during pulse defrosting, we studied the variation of T_{ml} during pulse-heating for different substrate temperatures. Figure 6.2(d) shows T_{ml} as a function of time for various initial temperatures, which is equal to the substrate temperature ($T_{in} = T_s$). The input conditions were $q''_{in} = 31$ W/cm^2, and $\Delta t_{pulse} = 0.5$ s. As expected, the results show that for $T_s = -15°C$, lower input heat fluxes (15 W/cm$^2 < q''_{in} < 30$ W/cm^2) enable spontaneous defrosting as compared to higher input fluxes required ($q''_{in} > 50$ W/cm^2) for $T_s = -70°C$.

6.5 Experimental Validation

6.5.1 Experiment Methods

To validate the model experimentally for the low temperature (T_s < -50°C) and high temperature regimes (-20°C < T_s < -10°C), we constructed two independent experimental setups. Figure 6.3(a) shows a schematic of the experimental setup used for the low temperature regime wherein liquid Nitrogen (LN2) was used as the cooling fluid. A solid L-shaped copper block was submerged into an LN2 bath. A glass substrate (Sigma Aldrich, 25 mm × 25 mm × 1.1 mm, 7.5 Ω electrical resistance) coated with a thin layer (≈ 550 nm) of ITO was used as the test substrate. In order to establish a firm electrical contact, two busbars were attached to the substrate using silver epoxy resin (Epo-Tek H20E) as shown on the right and left hand sides of the inset image of Fig. 6.3(c). The substrate was attached to the copper block using a thin layer (≈50 μm) of thermal paste (Apiezon N Grease). At steady state, the temperature of the substrate, measured using a thermocouple (Omega, K type, ± 0.5°C accuracy), was T_s = -71 ± 4.6°C.

Figure 6.3(b) shows a schematic of the high temperature (T_s = -15°C) experimental setup. A vertical cold plate (CP10, Lytron) connected to a chiller (PolyScience, Model: N0772046) set at -15°C was used to cool the substrate attached with a thin layer (≈ 50 μm) of thermal paste (Apiezon N Grease). At steady state, the temperature of the substrate was T_s = -15.1 ± 1.2°C. The ITO sample was connected in series with a transistor. Pulses of varying lengths were supplied to the transistor gate driver with a waveform generator (Agilent 33522A) in order to control the amount of time that current would conduct through the ITO sample. The amplitude of the current pulse was controlled by setting the current limit of the dc power supply (Kenwood PD56-10D). Since the circuit has inductance from the long connection cables, the pulse waveform contained ringing and was non-ideal. A gate resistance of 20 mΩ was employed so that the ringing would be

minimized and the energy from the pulse could be estimated using the ideal waveform approximation. During the de-icing/frosting process, optical videos were recorded in the normal direction of the substrate as shown in Fig. 6.3(a) and (b) using a DSLR camera (Canon Rebel T3i). Ice blocks having 5 mm thicknesses were frozen to the substrate by surface melting/refreezing [37]. For a detailed schematic of the pulse-defrosting circuit, as well as experimental setup photos, please see Section SX of the Supporting Information.

6.5.2 Experiment Results and Discussions

Figure 6.3(c) shows the pulse duration required for complete de-icing of the substrate for two different substrate temperatures, T_s = -70ºC and -15ºC as a function of input heat flux at the ITO coating. The numerical model and experiments are in good agreement, denoting that the heat-pulse required for spontaneous deicing (t_{pulse} < 0.5 s) of the substrate is q''_{in} > 15 W/cm^2 for T_s = -15ºC, and q''_{in} > 50 W/cm^2 for T_s = -70ºC. The area above the curves denote the regimes where spontaneous deicing can be achieved for a given pulse duration, t_{pulse} and input heat flux, q''_{in}. The discrepancy between the experiment and the numerical model at low input heat fluxes, q''_{in} < 20 W/cm^2 for T_s = -15ºC can be attributed to the 1D nature of the numerical model. For low input heat fluxes, the time required for thermal penetration of Joule heating from the busbars on the edges of the ITO sample (inset Figure 6.3(c)) towards its interior might be significant, which is not taken into account in the current study. To minimize the energy consumption, E_{in} during spontaneous pulse deicing, the function $E_{in} = q''_{in} \cdot t_{pulse}$ is optimized. It was observed that t_{pulse} is the significant parameter and decreasing t_{pulse} leads to a decrease in E_{in}. Although, it is evident in Figure 6.3(c) that decreasing t_{pulse} leads to an increase in q''_{in}, the overall energy consumption decreases. Thus, it is inferred that for minimizing the energy consumption during instantaneous

pulse defrosting, the least pulse duration is preferred. In the future, a 3 Dimensional model needs to be developed to account for the non-symmetries related to Joule heating by supplying electric current via busbars to the ITO coating. Furthermore, modeling of time varying melt layer thickness and time varying shear stress at the ice-solid interface needs to be developed. Modeling of the dynamics of the ice block as it slides down the surface with a varying shear will be needed to accurately design high fidelity pulse defrosting systems. The decoupled nature of the hydrodynamic forces and ice kinematics from the energy equation facilitate the integration of this shear stress dynamic with our numerical model and propose a good avenue for future work. Moreover, in the future, modeling of frost on the substrate should be done to accurately simulate the amount of energy required to defrost instantaneously, as compared to ice modeled in this study. Indeed, although the work considered here presents a starting point for engineers to develop pulse defrosting systems for arbitrarily long vertical surfaces, more work is needed in the future on optimization and economics of pulse defrosting in order to minimize energy input.

6.6 Conclusions

In this chapter, we discussed the most efficient way of supplying the defrosting energy to a surface covered with ice, at the solid-ice interface. To remove the ice efficiently, it is beneficial only to melt the interfacial layer adhering the ice to the solid surface, and allow gravity in conjunction with the ultra-thin lubricating meltwater layer to remove the ice. To better understand the physics, we developed a heat transfer model for transient interfacial pulse-defrosting. During pulse heating for spontaneous defrosting, the temperature at the critical thickness of melt layer, T_{ml} should be greater than the liquidus temperature, $T_{\mathrm{ml}} > T_{\mathrm{liq}}$ so that the adjacent ice block slides off the substrate due to gravity. We observed that for very low substrate temperatures ($T_s < -50°C$), in order to achieve spontaneous pulse-defrosting, high input heat fluxes at the ice-solid interface

($q"_{in} > 50$ W/cm^2) are required. Whereas, for substrates with higher temperatures ($T_s > $ -15°C), lower input heat fluxes (10 W/cm$^2 < q"_{in} < 30$ W/cm^2) enable spontaneous defrosting. We did experimental validation of the model by Joule heating of indium tin oxide (ITO) coated on glass samples to melt the interfacial ice layer. With heat fluxes ranging from 10 to 100 W/cm^2, spontaneous melting of the interfacial ice layer was achieved leading to rapid ice removal. The defrost time (≤ 0.5 s) for thin film ITO heaters was significantly lower than for the conventional heating methods. The experimental results showed excellent agreement with the numerical model. It was observed that for minimum energy consumption, lower pulse time is preferred. Design guidelines for interfacial pulse-defrosting applications were outlined based on the model developed in this work. This study not only provides a fundamental knowledge base for the design of efficient defrosting surfaces, but also highlights the benefits of interfacial heating on defrosting dynamics.
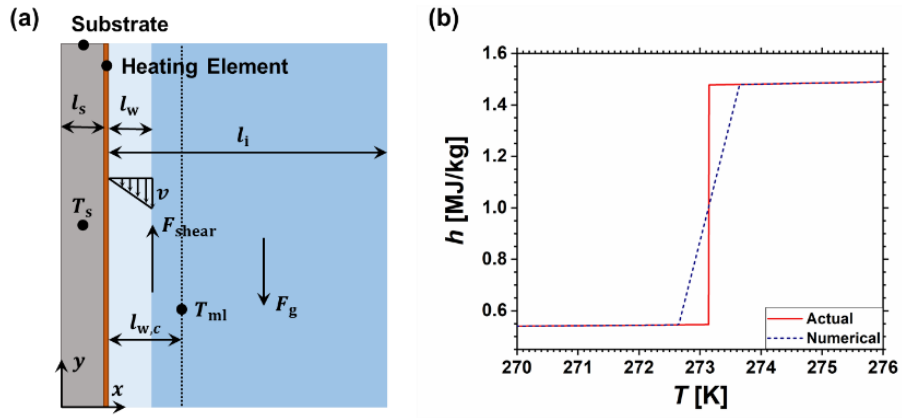
6.7 Figures

Figure 6.1. (a) Schematic drawing of the model. (b) Water enthalpy, h as a function of temperature used in the numerical model as compared to the actual enthalpy.
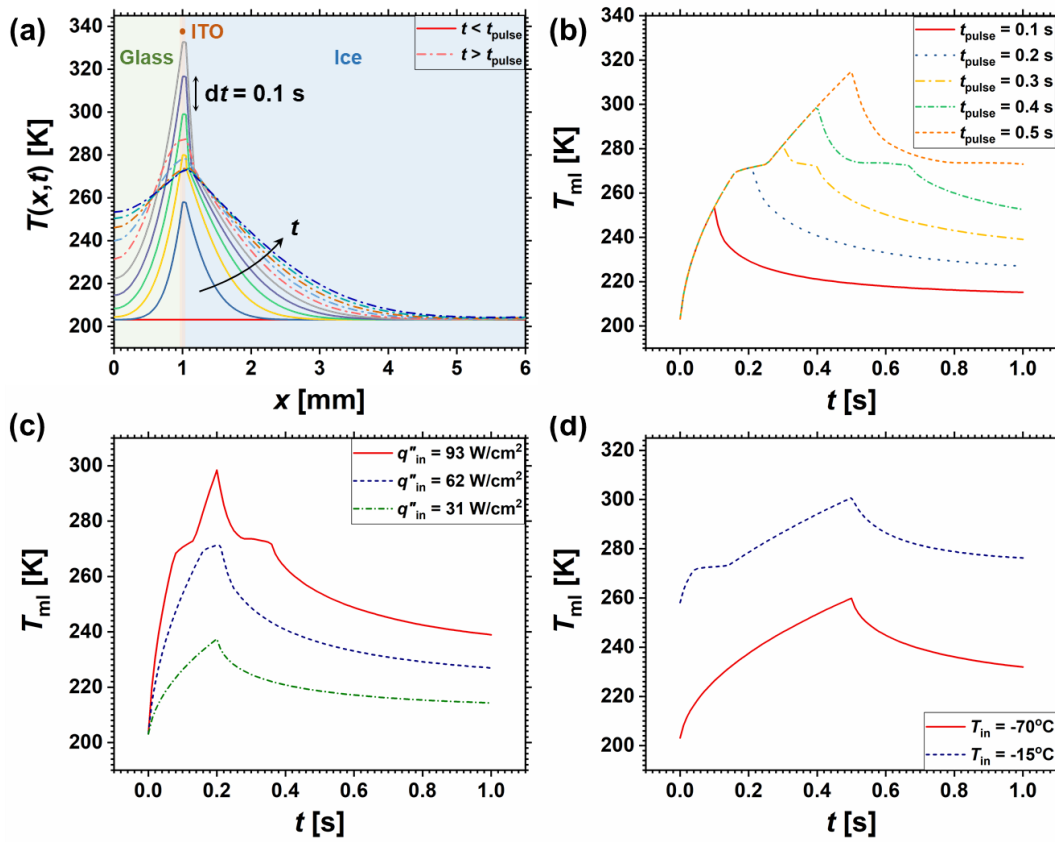
Figure 6.2. (a) Temperature profile with ascending time intervals for T_s = -70°C, t_{pulse} = 0.5 s, q''_{in} = 62 W/cm^2. The time interval between two adjacent profiles is 0.1 s. (b) T_{ml} as a function of time for various pulse-heating durations with T_s = -70°C, q''_{in} = 62 W/cm^2. (c) T_{ml} as a function of time for various input heat fluxes with T_s = -70°C, t_{pulse} = 0.2 s. (d) T_{ml} as a function of time for various initial conditions with q''_{in} = 31 W/cm^2, t_{pulse} = 0.5 s. For all the cases, l_i = 5 mm.

Figure 6.3. Schematic of the experimental setup for (a) $T_s = -70°C$, and (b) $T_s = -15°C$. (c) Duration of pulse required for complete de-icing as a function of input heat flux for $T_s = -70°C$ and $-15°C$ (Inset: Vertically oriented ITO coated glass substrate with ice block frozen on it).
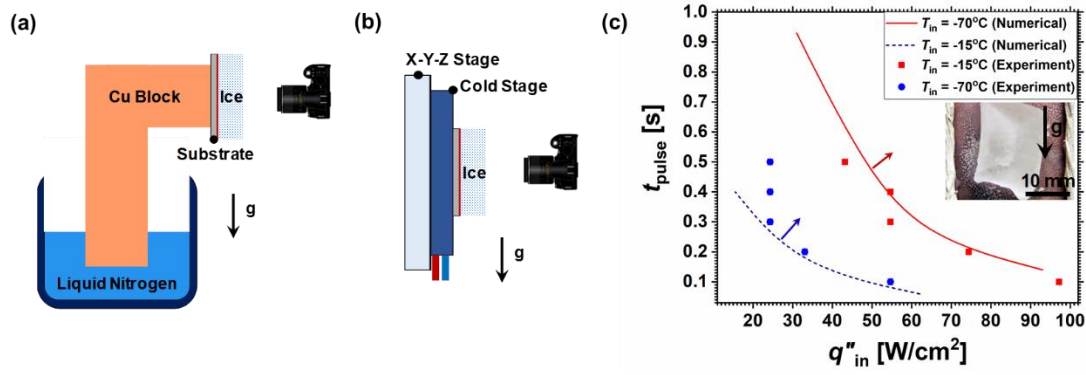
CHAPTER 7: CONCLUSIONS

7.1 Condensation on Biphilic Surfaces

We coupled the individual droplet growth and condensation heat transfer with droplet jumping dynamics to optimize the design of a biphilic surface for maximum heat flux. We show that a biphilic surface has higher droplet growth rate during condensation than a superhydrophobic surface. In contrast to the previously used strategy of highly wetting droplet growth spots to achieve ordered droplet growth, we explored an alternative strategy of promoting a large droplet growth rate contrast. By promoting significantly faster droplet growth rates on the defined growth spots, a locally hydrophobic (large receding angle) surface wetting state can be used. This leads to a significant reduction in droplet adhesion to extend the range of pattern geometries and droplet Oh where droplet jumping is possible. Furthermore, the biphilic surface exhibits 10X higher heat transfer coefficient in comparison to a SHP surface. Biphilic surfaces with lower maximum droplet sizes (higher Oh) and lower contact angles during coalescence are preferred for higher heat flux. To determine the droplet jumping dynamics in this regime, we performed VOF numerical simulations of coalescence induced droplet jumping. The numerical simulations show that for hydrophilic spots, higher pitch ratios (high contact angle) and lower Oh are required to observe coalescence induced droplet jumping, whereas hydrophobic spots exhibit jumping at higher Oh and lower contact angle, enhancing the heat flux. The characteristic velocity of jumping droplets on a biphilic surface with hydrophobic spots was higher than a surface with no adhesion. The results of the numerical model are superimposed on the condensation heat transfer model to optimize the design of a biphilic surface for maximum condensation heat flux. This study not only provides a more accurate framework for predicting the jumping-droplet condensation heat transfer

on biphilic surfaces, it offers insights into biphilic surface design methodologies to achieve maximum condensation heat flux.

7.2 Bulk Water Freezing Dynamics

We have demonstrated that the use of nanoscale superhydrophobic surfaces does not result in the anomalous heat-transfer mediated delay of water freezing. Instead, classical heat transfer effects govern the freezing process irrespective of wettability, indicating that the required liquid length scales must approach the length scale of the coating in order to observe an appreciable effect. Transient freezing FEM simulations revealed that the overall heat transfer coefficient at the column base for freezing on nanoscale superhydrophobic surfaces approaches 2 kW/m^{2}K, irrespective of wettability or column length scale, and reduces monotonically with increased coating thickness. The results shown here suggest that in order to delay the frost wave front propagation inside the liquid at larger length scales, one must use thicker superhydrophobic coatings on the surface, where the coating resistance is comparable to the liquid conduction resistance. For applications involving air side heat transfer, this translates to a 5% overall heat transfer decrease for a 45% delay in total freezing time.

7.3 Individual Droplet Freezing and Frost Wave Propagation

We have demonstrated that latent heat released into the substrate during freezing of individual droplets does not affect frost wave propagation or frost halo formation. Furthermore, we showed that the ice bridge velocities are independent of the substrate thermal conductivity. Ice bridge formation during frost wave propagation is governed solely by the vapor pressure gradient caused by the difference in saturation pressure of the water vapor surrounding the liquid droplet and the frozen droplet. We showed that at length scales tested here, the individual droplet freezing

131

time depends on the substrate wettability, since it governs the droplet thermal resistance (which is the most dominant thermal resistance), increasing with higher intrinsic and apparent advancing contact angles. By characterizing the individual droplet freezing (~1ms) and frost wave propagation (~1s) timescales, we show that delay in individual droplet freezing (due to wettability effects) does not affect the overall frosting speed due to the disparate timescales of the two processes. This study not only elucidates the role of latent heat released into the substrate during frost wave propagation but also explains the effect of substrate thermal conductivity and wettability during ice bridge formation and individual droplet freezing.

7.4 Dynamic Defrosting on Superhydrophobic and Biphilic Surfaces

We rigorously studied the defrosting behavior on hydrophilic, superhydrophobic, and biphilic (hydrophilic/superhydrophobic) surfaces. Using tip and side view optical imaging, we showed that superhydrophobic regions undergo dynamic defrosting, where the frost layer initiates spontaneous motion via the formation of highly mobile slush. Due to the difference in the surface forces on biphilic surfaces, the hydrophilic regions acted to 'pull' the mobile slush prior to complete frost melting, even in the absence of forces such as gravity or vapor shear. Horizontally oriented biphilic surfaces having SHP regions of thickness $L_{SHP} \leq 4$ mm showed enhanced defrosting behavior when compared to unaltered or fully SHP surfaces. For biphilic surfaces with $L_{SHP} > 4$ mm, satellite water droplets remained on the SHP areas due to the Plateau-Rayleigh instability. The limit of the Plateau-Rayleigh instability at $L_{SHP} = 4$ mm was observed irrespective of the surface heating rate. To understand the effect of pattern heterogeneity, we studied banana-leaf-inspired branched biphilic patterns optimized to minimize cleaning time. We observed that binary biphilic designs were simpler to manufacture when compared to branched designs, and offered better surface cleaning performance during defrosting. Defrosting utilizing full evaporation

132

showed that designs with hydrophilic regions of thickness, L_{HL} = 1 mm performed better than L_{HL} = 2 mm for $L_{\text{SHP}} \leq$ 4 mm, due to lower thermal resistance of retained water. During dynamic defrosting on vertically oriented surfaces (with gravity), SHP samples exhibited the best cleaning performance, with biphilic surfaces within 30% of the minimum cleaning time. Our work not only provides the fundamental understanding required for the design of heterogeneous defrosting coatings, but also elucidates the role of wettability gradients on defrosting dynamics.

7.5 Pulse Interfacial Defrosting

We discussed the most efficient way of supplying the defrosting energy to a surface covered with ice, at the solid-ice interface. To remove the ice efficiently, it is beneficial only to melt the interfacial layer adhering the ice to the solid surface, and allow gravity in conjunction with the ultra-thin lubricating meltwater layer to remove the ice. To better understand the physics, we developed a heat transfer model for transient interfacial pulse-defrosting. During pulse heating for spontaneous defrosting, the temperature at the critical thickness of melt layer, T_{ml} should be greater than the liquidus temperature, $T_{\text{ml}} > T_{\text{liq}}$ so that the adjacent ice block slides off the substrate due to gravity. We observed that for very low substrate temperatures (T_s < -50°C), in order to achieve spontaneous pulse-defrosting, high input heat fluxes at the ice-solid interface (q''_{in} > 50 W/cm^2) are required. Whereas, for substrates with higher temperatures (T_s > -15°C), lower input heat fluxes (10 W/cm^2 < q''_{in} < 30 W/cm^2) enable spontaneous defrosting. We did experimental validation of the model by Joule heating of indium tin oxide (ITO) coated on glass samples to melt the interfacial ice layer. With heat fluxes ranging from 10 to 100 W/cm^2, spontaneous melting of the interfacial ice layer was achieved leading to rapid ice removal. The defrost time ($\leq$ 0.5 s) for thin film ITO heaters was significantly lower than for the conventional heating methods. The experimental results showed excellent agreement with the numerical model.

133

It was observed that for minimum energy consumption, lower pulse time is preferred. Design guidelines for interfacial pulse-defrosting applications were outlined based on the model developed in this work. This study not only provides a fundamental knowledge base for the design of efficient defrosting surfaces, but also highlights the benefits of interfacial heating on defrosting dynamics.

REFERENCES

[1]   R. N. Wenzel, Industrial & Engineering Chemistry **28**, 988 (1936).

[2]   A. Cassie and S. Baxter, Transactions of the Faraday Society **40**, 546 (1944).

[3]   J. B. Boreyko and C. H. Chen, Phys Rev Lett **103**, 184501 (2009).

[4]   R. Enright, N. Miljkovic, A. Al-Obeidi, C. V. Thompson, and E. N. Wang, Langmuir **40**, 14424 (2012).

[5]   N. Miljkovic, R. Enright, Y. Nam, K. Lopez, N. Dou, J. Sack, and E. N. Wang, Nano Letters **13**, 179 (2013).

[6]   N. Miljkovic, D. J. Preston, R. Enright, and E. N. Wang, Acs Nano **7**, 11043 (2013).

[7]   Y. M. Hou, M. Yu, X. M. Chen, Z. K. Wang, and S. H. Yao, Acs Nano **9**, 71 (2015).

[8]   E. Ölçeroğlu and M. McCarthy, ACS applied materials & interfaces **8**, 5729 (2016).

[9]   E. Moallem, L. Cremaschi, D. E. Fisher, and S. Padhmanabhan, Exp Therm Fluid Sci **39**, 176 (2012).

[10]   Y. Xia, Y. Zhong, P. S. Hrnjak, and A. M. Jacobi, Int J Refrig **29**, 1066 (2006).

[11]   Y. Bolouk, Adhesion of Freezing Precipitates to Aircraft Surfaces, 1996.

[12]   O. Parent and A. Ilinca, Cold Reg Sci Technol **65**, 88 (2011).

[13]   M. Farzaneh, *Atmospheric icing of power networks* (Springer Science & Business Media, 2008).

[14]   J. L. Hoke, J. G. Georgiadis, and A. M. Jacobi, J Thermophys Heat Tr **18**, 228 (2004).

[15]   B. Na and R. L. Webb, International Journal of Heat and Mass Transfer **46**, 3797 (2003).

[16]   Q. L. Zhang, M. He, X. P. Zeng, K. Y. Li, D. P. Cui, J. Chen, J. J. Wang, Y. L. Song, and L. Jiang, Soft Matter **8**, 8285 (2012).

[17]   S. Nath, S. F. Ahmadi, and J. B. Boreyko, Nanosc Microsc Therm (2016).

[18]   A. Alizadeh *et al.*, Langmuir **28**, 3180 (2012).

[19]   L. Mishchenko, B. Hatton, V. Bahadur, J. A. Taylor, T. Krupenkin, and J. Aizenberg, Acs Nano **4**, 7699 (2010).

[20]   S. Jung, M. Dorrestijn, D. Raps, A. Das, C. M. Megaridis, and D. Poulikakos, Langmuir **27**, 3059 (2011).

[21]   P. Tourkine, M. Le Merrer, and D. Quere, Langmuir **25**, 7214 (2009).

[22]   J. B. Dooley, *Determination and characterization of ice propagation mechanisms on surfaces undergoing dropwise condensation* (TEXAS A&M UNIVERSITY, 2010).

[23]   J. B. Boreyko and P. C. Collier, Acs Nano **7**, 1618 (2013).

[24]   S. Nath, S. F. Ahmadi, and J. B. Boreyko, Nanosc Microsc Therm **21**, 81 (2017).

[25]   J. B. Boreyko, R. R. Hansen, K. R. Murphy, S. Nath, S. T. Retterer, and C. P. Collier, Sci Rep-Uk **6**, 19131 (2016).

[26]   Y. Ding, G. Ma, Q. Chai, and Y. Jiang, International Journal of Refrigeration **27**, 671 (2004).

[27]   M. Qu, L. Xia, S. Deng, and Y. Jiang, Applied energy **97**, 327 (2012).

[28]   W. F. Stoecker, J. J. Lux, and R. J. Kooy, Ashrae J **25**, 66 (1983).

[29]   D. H. Niederer, ASHRAE Transactions **82**

467 (1976).

[30]   P. Zhang and P. Hrnjak, International Journal of Refrigeration **33**, 1118 (2010).

[31]   Y. P. Xia, P. S. Hrnjak, and A. M. Jacobi, Ashrae Tran **111**, 487 (2005).

[32]   M. Farzaneh, C. Volat, and A. Leblond, Atmospheric Icing of Power Networks. Springer, Netherlands, 229 (2008).

[33]   A.-R. O. Raji, S. Salters, E. L. Samuel, Y. Zhu, V. Volman, and J. M. Tour, ACS applied materials & interfaces **6**, 16661 (2014).

[34]   V. Volman, J. M. Tour, Y. Zhu, and A.-R. O. Raji, in *Microwaves, Radar, and Wireless Communication (MIKON), 2014 20th International Conference on* (IEEE, 2014), pp. 1.

[35]   M. Elsharkawy, D. Tortorella, S. Kapatral, and C. M. Megaridis, Langmuir **32**, 4278 (2016).

[36]   G. C. Botura, D. Sweet, and D. Flosdorf, *Development and demonstration of low power electrothermal de-icing system* (American Institute of Aeronautics and Astronautics, 2005).

[37]   V. F. Petrenko, C. R. Sullivan, V. Kozlyuk, F. V. Petrenko, and V. Veerasamy, Cold Reg Sci Technol **65**, 70 (2011).

[38]   M. H. Kim and C. W. Bullard, Int J Refrig **25**, 924 (2002).

[39]   B. Z. Li and R. M. Yao, Renew Energ **34**, 1994 (2009).

[40]   L. Perez-Lombard, J. Ortiz, and C. Pout, Energ Buildings **40**, 394 (2008).

[41]   J. M. Beer, Prog Energ Combust **33**, 107 (2007).

[42]   T. B. Peters *et al.*, Ieee T Comp Pack Man **2**, 1637 (2012).

[43]   E. J. Le Fevre and J. W. Rose, International Journal of Heat and Mass Transfer **7**, 272 (1964).

[44]   E. J. Le Fevre and J. W. Rose, in *Proceedings of the Third International Heat Transfer Conference* (ASME, Chicago, IL, 1966), pp. 362.

[45]   B. B. Mikic, International Journal of Heat and Mass Transfer **12**, 1311 (1969).

[46]   J. W. Rose, International Journal of Heat and Mass Transfer **10**, 755 (1967).

[47]   J. W. Rose, P I Mech Eng a-J Pow **216**, 115 (2002).

[48]   R. Enright, N. Miljkovic, J. Sprittles, K. Nolan, R. Mitchell, and E. N. Wang, Acs Nano **8**, 10352 (2014).

[49]   F. J. Liu, G. Ghigliotti, J. J. Feng, and C. H. Chen, J Fluid Mech **752**, 39 (2014).

[50]   F. J. Liu, G. Ghigliotti, J. J. Feng, and C. H. Chen, J Fluid Mech **752**, 22 (2014).

[51]   Y. Nam, H. Kim, and S. Shin, Appl Phys Lett **103** (2013).

[52]   Y. Nam, D. Seo, C. Lee, and S. Shin, Soft Matter **11**, 154 (2015).

[53]   Y. Shang, Y. Hou, M. Yu, and S. Yao, International Journal of Heat and Mass Transfer **122**, 117 (2018).

[54]   Y. Hou, M. Yu, X. Chen, Z. Wang, and S. Yao, Journal of Heat Transfer **137**, 080907 (2015).

[55]   S. Chavan *et al.*, Langmuir **32**, 7774 (2016).

[56]   R. W. Schrage, Thesis, Columbia University., 1953.

[57]   V. P. Carey, *Liquid-Vapor Phase-Change Phenomena* (CRC Press, 2008), 2nd edn.

[58]   S. Kim and K. J. Kim, Journal of Heat Transfer **133**, 081502 (2011).

[59]   N. Miljkovic, R. Enright, and E. N. Wang, Journal of Heat Transfer **135** (2013).

[60]   Y. Hou, M. Yu, X. Chen, Z. Wang, and S. Yao, Acs Nano **9**, 71 (2014).

[61]   M. Abu-Orabi, International journal of heat and mass transfer **41**, 81 (1998).

[62]   J. W. Rose, in *Proceedings of the Royal Society of London A: Mathematical, Physical and Engineering Sciences* (The Royal Society, 1987), pp. 305.

[63]   J. W. Rose, in *Heat Transfer Conference*1998), pp. 89.

[64]   D. Labuntsov, High Temperature **5**, 579 (1967).

[65]   T. Muratova and D. Labuntsov, High temperature **7**, 888 (1969).

[66]   Y. Sone and Y. Onishi, Journal of the Physical Society of Japan **44**, 1981 (1978).

[67]   D. Labuntsov and A. Kryukov, International Journal of Heat and Mass Transfer **22**, 989 (1979).

[68]   T. Ytrehus and J. Alvestad, Progress in Astronautics and Aeronautics **74**, 330 (1981).

[69]   J. Cipolla Jr, H. Lang, and S. Loyalka, The Journal of Chemical Physics **61**, 69 (1974).

[70]   H. Lang, The Journal of Chemical Physics **62**, 858 (1975).

[71]   J. Thomas Jr, Transport Theory and Statistical Physics **14**, 485 (1985).

[72]   C. Siewert and J. Thomas Jr, The Physics of Fluids **16**, 1557 (1973).

[73]   A. Umur and P. Griffith, ASME J. Heat Transfer **87**, 275 (1965).

[74]   S. S. Sadhal and W. W. Martin, International Journal of Heat and Mass Transfer **20**, 1401 (1977).

[75]   G. H. McKinley and M. Renardy, Phys Fluids **23**, 127101 (2011).

[76]   R. Attarzadeh and A. Dolatabadi, Phys Fluids **29**, 012104 (2017).

[77]   J. Wasserfall, P. Figueiredo, R. Kneer, W. Rohlfs, and P. Pischke, Physical Review Fluids **2**, 123601 (2017).

[78]   Y. Cheng, J. Xu, and Y. Sui, International Journal of Heat and Mass Transfer **95**, 506 (2016).

[79]   F. Liu, G. Ghigliotti, J. J. Feng, and C.-H. Chen, J Fluid Mech **752**, 39 (2014).

[80]   T. Mouterde, G. Lehoucq, S. Xavier, A. Checco, C. T. Black, A. Rahman, T. Midavaine, C. Clanet, and D. Quéré, Nat Mater **16**, 658 (2017).

[81]   K. K. Varanasi, T. Deng, J. D. Smith, M. Hsu, and N. Bhate, Appl Phys Lett **97** (2010).

[82]   Y. S. Chang, J Therm Sci Tech-Jpn **6**, 123 (2011).

[83]   J. L. Laforte, M. A. Allaire, and J. Laflamme, Atmospheric Research **46**, 143 (1998).

[84]   B. D. Storey and A. M. Jacobi, International Journal of Heat and Mass Transfer **42**, 3787 (1999).

[85]   V. Bahadur, L. Mishchenko, B. Hatton, J. A. Taylor, J. Aizenberg, and T. Krupenkin, Langmuir **27**, 14143 (2011).

[86]   L. Yin, Q. Xia, J. A. Xue, S. Q. Yang, Q. J. Wang, and Q. M. Chen, Appl Surf Sci **256**, 6764 (2010).

[87]   P. Guo, Y. M. Zheng, M. X. Wen, C. Song, Y. C. Lin, and L. Jiang, Adv Mater **24**, 2642 (2012).

[88]   T. Deng, K. K. Varanasi, M. Hsu, N. Bhate, C. Keimel, J. Stein, and M. Blohm, Appl Phys Lett **94** (2009).

[89]   S. A. Kulinich and M. Farzaneh, Appl Surf Sci **255**, 8153 (2009).

[90]   L. B. Boinovich and A. M. Emelyanenko, Mendeleev Commun **23**, 3 (2013).

[91]   F. C. Wang, C. R. Li, Y. Z. Lv, F. C. Lv, and Y. F. Du, Cold Reg Sci Technol **62**, 29 (2010).

[92]   H. Wang, G. G. He, and Q. Q. Tian, Appl Surf Sci **258**, 7219 (2012).

[93]   Y. F. Huang, M. J. Hu, S. P. Yi, X. H. Liu, H. B. Li, C. Huang, Y. B. Luo, and Y. Li, Thin Solid Films **520**, 5644 (2012).

[94]   T. V. J. Charpentier, A. Neville, P. Millner, R. W. Hewson, and A. Morina, J Colloid Interf Sci **394**, 539 (2013).

[95]   H. Wang, L. Tang, X. Wu, W. Dai, and Y. Qiu, Appl Surf Sci **253**, 8818 (2007).

[96]   M. He, J. Wang, H. Li, X. Jin, J. Wang, B. Liu, and Y. Song, Soft Matter **6**, 2396 (2010).

[97]   M. He, J. Wang, H. Li, and Y. Song, Soft Matter **7**, 3993 (2011).

[98]   Q. Zhang, M. He, X. Zeng, K. Li, D. Cui, J. Chen, J. Wang, Y. Song, and L. Jiang, Soft Matter **8**, 8285 (2012).

[99]   Y. Zhang, X. Yu, H. Wu, and J. Wu, Appl Surf Sci **258**, 8253 (2012).

[100] X. Gao, X. Yan, X. Yao, L. Xu, K. Zhang, J. Zhang, B. Yang, and L. Jiang, Adv Mater **19**, 2213 (2007).

[101] P. Tourkine, M. Le Merrer, and D. Quéré, Langmuir **25**, 7214 (2009).

[102] Y. Zhou, W. Yi-Zhi, Y. Yi-Fan, G. Mao-Gang, and X. Xiao-Liang, Chinese Physical Society **21** (2012).

[103] I. A. Larmour, S. E. Bell, and G. C. Saunders, Angewandte Chemie **119**, 1740 (2007).

[104] J. Stefan, Annalen der Physik **278**, 269 (1891).

[105] M. Nauenberg, European Journal of Physics **37**, 045102 (2016).

[106] A. J. Meuler, J. D. Smith, K. K. Varanasi, J. M. Mabry, G. H. McKinley, and R. E. Cohen, ACS Applied Materials & Interfaces **2**, 3100 (2010).

[107] N. Miljkovic, R. Enright, Y. Nam, K. Lopez, N. Dou, J. Sack, and E. N. Wang, Nano Lett **13**, 179 (2013).

[108] N. Miljkovic, R. Enright, and E. N. Wang, ACS Nano **6**, 1776 (2012).

[109] R. Enright, N. Miljkovic, J. L. Alvarado, K. Kim, and J. W. Rose, Nanosc Microsc Therm **18**, 223 (2014).

[110] R. Enright, N. Miljkovic, N. Dou, Y. Nam, and E. N. Wang, Journal of Heat Transfer **135**, 091304 (2013).

[111] N. Miljkovic and E. N. Wang, Mrs Bull **38**, 397 (2013).

[112] N. Miljkovic, R. Enright, and E. N. Wang, Journal of Heat Transfer, doi: 10.1115/1.4024597 (2013).

[113] K. Sobolev *et al.*, Anti-icing and de-icing superhydrophobic concrete to improve the safety on critical elements on roadway pavements, 2013.

[114] X. Sun and K. Rykaczewski, Acs Nano **11**, 906 (2016).

[115] M. C. Rajagopal and S. K. Das, Journal of Non-Newtonian Fluid Mechanics **228**, 17 (2016).

[116] G. Chaudhary and R. Li, Exp Therm Fluid Sci **57**, 86 (2014).

[117] H. Zhang, Y. Zhao, R. Lv, and C. Yang, International Journal of Thermal Sciences **101**, 59 (2016).

[118] S. Chavan, J. Carpenter, M. Nallapaneni, J. Chen, and N. Miljkovic, Appl Phys Lett **110**, 041604 (2017).

[119] J. Guadarrama-Cetina, A. Mongruel, W. Gonzalez-Vinas, and D. Beysens, Epl-Europhys Lett **101** (2013).

[120] Y. Zhang, M. R. Klittich, M. Gao, and A. Dhinojwala, ACS applied materials & interfaces **9**, 6512 (2017).

[121] K. D. Esmeryan, C. E. Castano, R. Mohammadi, Y. Lazarov, and E. I. Radeva, Journal of Physics D: Applied Physics **51**, 055302 (2018).

[122]   M.-H. Kim, H. Kim, K.-S. Lee, and D. R. Kim, Energy Conversion and Management **138**, 1 (2017).

[123]   P. B. Weisensee, Y. Wang, Q. Hongliang, D. Schultz, W. P. King, and N. Miljkovic, International Journal of Heat and Mass Transfer **109**, 187 (2017).

[124]   J. Rose and L. Glicksman, International journal of heat and mass transfer **16**, 411 (1973).

[125]   A. Kim, C. Lee, H. Kim, and J. Kim, ACS applied materials & interfaces **7**, 7206 (2015).

[126]   S. Nath and J. B. Boreyko, Langmuir **32**, 8350 (2016).

[127]   G. Graeber, T. M. Schutzius, H. Eghlidi, and D. Poulikakos, Proceedings of the National Academy of Sciences **114**, 11040 (2017).

[128]   S. Jung, M. K. Tiwari, and D. Poulikakos, Proceedings of the National Academy of Sciences **109**, 16073 (2012).

[129]   Y. Nam and Y. S. Ju, J Adhes Sci Technol **27**, 2163 (2013).

[130]   K. Rykaczewski, J. H. J. Scott, and A. G. Fedorov, Appl Phys Lett **98** (2011).

[131]   F. Aliotta, P. V. Giaquinta, R. C. Ponterio, S. Prestipino, F. Saija, G. Salvato, and C. Vasi, Sci Rep-Uk **4**, 7230 (2014).

[132]   F. Feuillebois, A. Lasek, P. Creismeas, F. Pigeonneau, and A. Szaniawski, J Colloid Interf Sci **169**, 90 (1995).

[133]   C. Angell, Annual Review of Physical Chemistry **34**, 593 (1983).

[134]   A. F. Mills, (Prentice Hall Upper Saddle River, NJ, 1999).

[135]   P. B. Weisensee, J. Tian, N. Miljkovic, and W. P. King, Sci Rep-Uk **6**, 30328 (2016).

[136]   R. Radermacher and K. Kim, International Journal of Refrigeration **19**, 61 (1996).

[137]   J. D. J. D. o. E. Kelso, (2012).

[138]   L. Huang, Z. Liu, Y. Liu, Y. Gou, and J. Wang, Experimental Thermal and Fluid Science **33**, 1049 (2009).

[139]   J. Lv, Y. Song, L. Jiang, and J. Wang, Acs Nano **8**, 3152 (2014).

[140]   P. Zhang and F. Y. Lv, Energy **82**, 1068 (2015).

[141]   C. H. M. Machielsen and H. G. Kerschbaumer, International Journal of Refrigeration **12**, 283 (1989).

[142]   J. La Due, M. Muller, and M. Swangler, Journal of aircraft **33**, 131 (1996).

[143]   A. P. Broeren, S. Lee, and C. Clark, Journal of Aircraft **53**, 451 (2015).

[144]   J. Brown, S. Raghunathan, J. Watterson, A. Linton, and D. Riordon, Journal of aircraft **39**, 65 (2002).

[145]   O. Harireche, P. Verdin, C. P. Thompson, and D. W. Hammond, Journal of Aircraft **45**, 1924 (2008).

[146]   S. Özgen, M. Carbonaro, and G. Sarma, Physics of Fluids **14**, 3391 (2002).

[147]   W. Dong, J. Zhu, M. Zheng, and Y. Chen, Journal of Propulsion and Power **31**, 896 (2015).

[148]   T. G. Keith Jr, K. J. DEWITT, J. K. Nathman, D. A. Dietrich, and K. M. Al-Khalil, Journal of Propulsion and Power **6**, 628 (1990).

[149]   C. Zilio and L. Patricelli, Applied Thermal Engineering **63**, 40 (2014).

[150]   G. Giebel, R. Brownsword, G. Kariniotakis, M. Denhard, and C. Draxl, ANEMOS. plus (2011).

[151]   D. H. Thomas, *Energy Efficiency through Combined Heat and Power or Cogeneration* (Nova Science Publishers, 2010).

[152]   A. K. Andersson and L. Chapman, Accident Analysis & Prevention **43**, 284 (2011).

[153]   D. Aydın, R. Kizilel, R. O. Caniaz, and S. Kizilel, Industrial & Engineering Chemistry Research **54**, 12587 (2015).

[154]   E. Heymsfield, A. Osweiler, P. Selvam, and M. Kuss, Journal of Cold Regions Engineering **28**, 04014001 (2014).

[155]   A. Klein-Paste and J. Wåhlin, Cold Regions Science and Technology **96**, 1 (2013).

[156]   B. Li and R. Yao, Renewable Energy **34**, 1994 (2009).

[157]   Y. Xia, Y. Zhong, P. Hrnjak, and A. Jacobi, International Journal of Refrigeration **29**, 1066 (2006).

[158]   Y.-S. Chang, Journal of Thermal Science and Technology **6**, 123 (2011).

[159]   M. R. Nasr, M. Fauchoux, R. W. Besant, and C. J. Simonson, Renewable and Sustainable Energy Reviews **30**, 538 (2014).

[160]   M. Amer and C.-C. Wang, Renewable and Sustainable Energy Reviews **73**, 53 (2017).

[161]   L. L. Cao, A. K. Jones, V. K. Sikka, J. Z. Wu, and D. Gao, Langmuir **25**, 12444 (2009).

[162]   S. Jung, M. K. Tiwari, N. V. Doan, and D. Poulikakos, Nat Commun **3** (2012).

[163]   H. Wang, L. M. Tang, X. M. Wu, W. T. Dai, and Y. P. Qiu, Appl Surf Sci **253**, 8818 (2007).

[164]   C. J. L. Hermes, R. O. Piucco, J. R. Barbosa, and C. Melo, Exp Therm Fluid Sci **33**, 371 (2009).

[165]   A. J. Meuler, G. H. McKinley, and R. E. Cohen, Acs Nano **4**, 7048 (2010).

[166]   S. A. Kulinich and M. Farzaneh, Langmuir **25**, 8854 (2009).

[167]   S. A. Kulinich and M. Farzaneh, Cold Reg Sci Technol **65**, 60 (2011).

[168]   S. Farhadi, M. Farzaneh, and S. A. Kulinich, Appl Surf Sci **257**, 6264 (2011).

[169]   M. Nosonovsky and V. Hejazi, Acs Nano **6**, 8488 (2012).

[170]   S. Chavan, D. Park, N. Singla, P. Sokalski, K. Boyina, and N. Miljkovic, Langmuir **34**, 6636 (2018).

[171]   S. F. Ahmadi, S. Nath, G. J. Iliff, B. R. Srijanto, C. P. Collier, P. Yue, and J. B. Boreyko, ACS applied materials & interfaces **10**, 32874 (2018).

[172]   V. J. Schaefer and I. Langmuir, *Project cirrus* 1953).

[173]   K. Adachi, K. Saiki, and H. Sato, in *Ultrasonics Symposium, 1998. Proceedings., 1998 IEEE* (IEEE, 1998), pp. 759.

[174]   K. Adachi, K. Saiki, H. Sato, and T. Ito, Japanese journal of applied physics **42**, 682 (2003).

[175]   A. Ghosh, S. Beaini, B. J. Zhang, R. Ganguly, and C. M. Megaridis, Langmuir **30**, 13103 (2014).

[176]   J. B. Boreyko, B. R. Srijanto, T. D. Nguyen, C. Vega, M. Fuentes-Cabrera, and C. P. Collier, Langmuir **29**, 9516 (2013).

[177]   A. Ghosh, R. Ganguly, T. M. Schutzius, and C. M. Megaridis, Lab on a Chip **14**, 1538 (2014).

[178]   É. Lorenceau and D. Quéré, J Fluid Mech **510**, 29 (2004).

[179]   A. A. Günay, S. Sett, J. Oh, and N. Miljkovic, Langmuir **33**, 12007 (2017).

[180]   S. Dash and S. V. Garimella, Phys Rev E **89**, 042402 (2014).

[181]   J. M. Stauber, S. K. Wilson, B. R. Duffy, and K. Sefiane, J Fluid Mech **744** (2014).

[182]   K. S. Boyina, N. V. Upot, J. Mayer, S. Chavan, K. F. Rabbi, T. Foulkes, X. Wang, and N. Miljkovic.

[183]   X. Chen, R. Ma, H. Zhou, X. Zhou, L. Che, S. Yao, and Z. Wang, Sci Rep-Uk **3** (2013).

[184]   N. Shamsundar and E. Sparrow, Journal of Heat Transfer, 333 (1975).

[185]   D. W. Hahn and M. N. Ã–zisik, *Heat conduction* (John Wiley & Sons, 2012).